Michael Seniuch

Analysis of the Phase Structure in Extended Higgs Models

July 2006

Analysis of the Phase Structure in Extended Higgs Models

Dissertation

zur Erlangung des Doktorgrades

der Fakultät für Physik

der Universität Bielefeld

vorgelegt von

Dipl.-Phys. Michael Seniuch

aus Herford

7. Juli 2006

Gutachter: Prof. Dr. D. Bödeker

Prof. Dr. M. Laine

Abstract

We study the generation of the baryon asymmetry in the context of electroweak baryogenesis in two different extensions of the Standard Model. First, we consider an effective theory, in which the Standard Model is augmented by an additional dimension-six Higgs operator. The effects of new physics beyond a cut-off scale are parameterized by this operator. The second model is the two-Higgs-doublet model, whose particle spectrum is extended by two further neutral and two charged heavy Higgs bosons. In both cases we focus on the properties of the electroweak phase transition, especially on its strength and the profile of the nucleating bubbles. After reviewing some general aspects of the electroweak phase transition and baryogenesis we derive the respective thermal effective potentials to one-loop order. We systematically study the parameter spaces, using numerical methods, and compute the strength of the phase transition and the wall thickness as a function of the Higgs masses. We find a strong first order transition for a light Higgs state with a mass up to about 200 GeV. In case of the dimension-six model the cut-off scale has to stay between 500 and 850 GeV, in the two-Higgs-doublet model one needs at least one heavy Higgs mass of 300 GeV. The wall thickness varies for both theories in the range roughly from two to fifteen, in units of the inverse critical temperature. We also estimate the size of the electron and neutron electric dipole moments, since new sources of CP-violation give rise to them. In wide ranges of the parameter space we are not in conflict with the experimental bounds. Finally the baryon asymmetry, which is predicted by these models, is related to the Higgs mass and the other appropriate input parameters. In both models the measured baryon asymmetry can be achieved for natural values of the model parameters.

Contents

Chapter 1

Introduction

The matter in our universe, concentrated in galaxies and stars, mainly consists of quarks and electrons. From particle physics it is known, theoretically as well as experimentally, that for each of these particle species there exists a corresponding antiparticle species. However, the actual amount of antimatter on Earth is infinitesimally small. Some antiparticles are produced in high energy collider experiments and some antiprotons with a ratio of $n_{\bar{p}}/n_p \approx 10^{-4}$ appear in the cosmic radiation, produced in secondary processes like $p+p \rightarrow 3p+\bar{p}$. Also in the near solar neighborhood interplanetary probes have found no evidence for antimatter. If astronomically large regions of antimatter existed, e.g. whole galaxies or clusters, one would need a so far unknown mechanism to separate them from matter regions or one would expect annihilation processes of particles and antiparticles at the boundaries between them. Since we do not observe any gamma-ray radiation which is characteristic for such an annihilation, at least our observable universe seems to be dominated by matter. Thus, nearly all the mass in the universe is concentrated in baryons.

A quantitative measure for this asymmetry is the ratio of the baryon density n_B to the entropy density s in the universe, which remains constant as long as equilibrium is preserved. Recent measurements by the Wilkinson Microwave Anisotropy Probe (WMAP) combined with large scale structure data lead to [1]

$$\eta_B \equiv \frac{n_B}{s} = (8.7 \pm 0.3) \cdot 10^{-11}. \tag{1.1}$$

The baryon asymmetry of the universe (BAU) can also be related to the photon density n_γ since s and n_γ are at the present time connected via $s = 7.04 n_\gamma$. Thus, with a ratio $n_B/n_\gamma \approx 6.1 \cdot 10^{-10}$ one observes in the universe for each baryon about $1.6 \cdot 10^9$ photons. The explanation of this striking ratio is still an open question in cosmology and particle physics.

Assuming the validity of the standard big bang model with matter-antimatter-symmetric initial conditions one needs a mechanism in the early evolution of the universe which generates the baryon asymmetry observed today, starting from a

symmetric initial state. Independent of a concrete baryogenesis model some requirements have to be satisfied to produce an asymmetry. In 1967 Sakharov stated three necessary conditions which have to be fulfilled for any baryogenesis scenario [2]. The so-called Sakharov conditions read:

- B (baryon number) violation,

- C (charge conjugation) and CP (product of charge and parity conjugation) violation,

- departure from thermal equilibrium.

The first condition is obvious. If the baryon number is conserved in all particle interactions, today's asymmetry can only be explained by asymmetric initial condition. The second requirement is necessary in order to ensure different rates for particle and antiparticle interactions. If C is not violated, the rate of a process involving particles is equal to the rate of the process for the corresponding antiparticles, which cannot result in an asymmetry. Due to the CPT-theorem, which assumes the combined symmetry of C, P and T as a fundamental symmetry respected by nature, the violation of CP is the equivalent of T-non-conservation, i.e. the violation of the time-reversal invariance. A T-conservation would cause equal rates of a process and the reverse process. The third condition arises from the fact that in a CPT-invariant theory the expectation value of the baryon number operator is time-independent in thermal equilibrium. Thus, a zero initial baryon number remains zero.

Early proposals for a baryogenesis scenario suggest out-of-equilibrium decays of a super-heavy particle [3–6]. They are usually formulated in the framework of grand unified theories (GUTs). In such models super-heavy X-bosons exist, whose decay rates fall below the Hubble rate during the expansion of the universe. Then these particles decouple from the thermal bath. The decays of the X-bosons and $\bar{X}$-bosons are CP- and B-violating, so that an asymmetry can be produced. The GUT-baryogenesis takes place at energy scales of the order of 10^{16} GeV. A different approach is the generation of the BAU via leptogenesis, in which in a first step a lepton asymmetry is created, which is then converted by so-called sphaleron-processes into an asymmetry in the baryonic sector. This scenario was first suggested in ref. [7], reviews can be found e.g. in refs. [8, 9]. In such models heavy Majorana neutrinos fall out of equilibrium at a temperature below the GUT scale, typically of the order $10^{10} - 10^{12}$ GeV. The L-violating neutrino decays lead to a lepton asymmetry, resulting finally via $(B + L)$-violating interactions in a baryon asymmetry. Heavy Majorana neutrinos may also explain the light Standard Model neutrino masses with the help of the so-called seesaw mechanism [10, 11]. In general, models which generate the BAU at temperatures above the electroweak scale, which is of the order 100 GeV, need beside the $(B + L)$-violating but $(B - L)$-conserving sphaleron processes also $(B - L)$-violation. Since the sphaleron rates are efficient for temperatures $T \gtrsim 100$ GeV, a baryon asymmetry generated at higher scales would be washed out if $(B - L)$ were conserved.

A further candidate for baryogenesis is the electroweak phase transition (EWPT), at which the $SU(2)_L \times U(1)_Y$ electroweak symmetry was broken to $U(1)_{em}$. It was first realized in ref. [12] that the EWPT in the Standard Model (SM) provides a natural baryogenesis mechanism if the phase transition (PT) is of first order. The SM already contains in the electroweak sector C- and CP-violation as well as the B-violating sphalerons, as required by the Sakharov conditions. The departure from thermal equilibrium would be realized in a first order PT. In addition the PT has to be strong in order to prevent the abovementioned washout. Assuming such a PT, bubbles of the broken phase begin to nucleate, they expand, finally percolate and fill all of space. CP-violating interactions of the particles in the plasma with the bubble walls in combination with $(B + L)$-violating sphalerons in front of the bubbles result in a baryon asymmetry, which is frozen inside the bubbles.

The strength of the phase transition depends on the Higgs mass, as has been investigated in the literature [13–18]. It turned out that the transition is strong only for Higgs masses $m_h \lesssim 40$ GeV. Since the experimental lower bound, given by the LEP2 experiments, restricts the Higgs mass to $m_h > 114$ GeV [19], electroweak baryogenesis is not possible in the Standard Model. Moreover the amount of CP-violation in the SM is too small to explain the BAU. However, extensions to the SM may provide all necessary ingredients. There have been many proposals during the last years concerning extended models (see, e.g. ref. [20] for a review). For instance, in supersymmetric theories a strong first order PT can occur if the partner of the top quark is lighter than about 150 GeV. Future collider experiments like those at the Large Hadron Collider (LHC), which will be brought on line in 2008, or measurements at a possible International Linear Collider (ILC) offer the possibility to detect the Higgs boson or potentially non-standard-model particles, e.g. sypersymmetric partners or additional Higgs bosons. These prospects provide an interesting and in the near future testable opportunity for an electroweak baryogenesis scenario in extensions of the Standard Model.

In this work we discuss two different extended Higgs models and analyze their phase structure. We do not aim at a high precision calculation, but focus on the phase transition characteristic in order to map the parameter range where a strong first order PT exists. We also discuss some crucial bubble properties like the profile and thickness of the bubble wall. In addition we investigate the influence of the CP-violating parameters of the models on the electric dipole moments (EDMs) of the electron and neutron. They are experimentally constrained by upper limits, which have to be respected by the models under consideration.

The first model which we consider is the Standard Model augmented by a dimension-six Higgs operator. It is an effective theory which parameterizes effects of new physics through a cut-off scale. It has been shown that the stabilization of the Higgs potential with a dimension-six interaction provides a first order phase transition also for Higgs masses above 100 GeV [21–23]. Moreover such non-renormalizable interactions allow for new sources of CP-violation.

A second, popular extension of the SM is the two-Higgs-doublet model (2HDM), in which the Higgs sector is supplemented by an additional $SU(2)$ Higgs doublet. Beside the SM Higgs the 2HDM contains two further neutral and two charged Higgs bosons. This model has been extensively discussed in the literature in many aspects, also in the view of electroweak baryogenesis [24–32]. In addition it offers the possibility for a strong first order phase transition. We choose a complex coupling in the potential, which introduces an explicit CP-violation and mixes the CP odd and even states. In principle there are nine independent couplings in this model. Due to physical constraints like the Higgs vacuum expectation value (VEV) and since we restrict to the case of degenerate heavy Higgs masses we are left with a four-dimensional parameter space, which we have to search for a first order PT.

Let us outline the structure of this work. In chapter 2 we review some general aspects of the electroweak phase transition. An important tool for analyzing the phase structure of a given model is the so-called effective potential. We introduce the effective potential to one-loop order considering a scalar field theory as an example, first at zero-temperature, then also at finite temperature. The strength of a phase transition is defined and the theoretical basics of bubble formation at the PT are presented.

In chapter 3 we discuss the mechanism of electroweak baryogenesis. We dwell on CP- and B-violation in the Standard Model, which are necessary conditions. Usually baryogenesis is described by a set of transport equations. Starting from dispersion relations for particles and antiparticles these equations are derived in the semiclassical approximation, which corresponds to an expansion in gradients.

The Standard Model with a dimension-six Higgs operator is introduced in chapter 4. We set up the one-loop effective thermal potential, which is analyzed with regard to the strength of the phase transition. We further compute the bubble wall thickness with different methods and compare them to each other. The shape of the bubble wall is modeled with a tanh-curve. We check that the experimental limits on the electron and neutron EDMs are not violated. We close this chapter with a discussion of the baryon asymmetry which can be generated in this model. The measured BAU can serve to obtain a correlation between the Higgs mass and the cut-off scale of the effective theory.

Subsequently we perform the same analysis for the two-Higgs-doublet model in chapter 5. We derive the corresponding effective potential including a renormalization procedure for the one-loop parameters. We compute the shape of the effective potential and the strength of the PT in dependence on the model parameters. We also pay attention to the bubble properties, like the change of the Higgs expectation value in the bubble wall. When passing the wall also the mass of a particle changes. We focus on the change of the top quark mass and its CP-violating phase. Moreover the electron and neutron EDMs in the 2HDM are computed. Finally we discuss the baryon asymmetry in the 2HDM, which can be used to predict the size of the EDMs. We close this work with a summary in chapter 6.

Chapter 2

The Electroweak Phase Transition

2.1 Electroweak symmetry breaking

In the early universe at temperatures above about 100 GeV the $SU(2)_L \times U(1)_Y$ electroweak symmetry was unbroken and all particles were massless. The temperature decreases while the universe expands and at $T \approx 100$ GeV, which corresponds to an age of 10^{-10} seconds, the electroweak symmetry was spontaneously broken down to $U(1)_{\text{em}}$ in a phase transition (PT) [33]. The weak gauge bosons and the leptons then receive their mass by the Higgs mechanism [34, 35]. In the Standard Model the Higgs Lagrangian reads

$$\mathscr{L}_{\text{Higgs}} = (D_\mu \Phi)^\dagger (D^\mu \Phi) - V_0 \tag{2.1}$$

with the potential

$$V_0 = -\mu^2 \Phi^\dagger \Phi + \lambda (\Phi^\dagger \Phi)^2 \tag{2.2}$$

and the $SU(2)$ Higgs doublet

$$\Phi = \begin{pmatrix} \phi^+ \\ \phi^0 \end{pmatrix} = \frac{1}{\sqrt{2}} \begin{pmatrix} \chi_1 + i\chi_2 \\ \phi + h + i\chi_3 \end{pmatrix} \tag{2.3}$$

where ϕ is the real constant background field, h the Higgs field and χ_i are the Goldstone bosons. The expansion of the potential around the background field yields

$$V_0(\phi) = -\frac{\mu^2}{2}\phi^2 + \frac{\lambda}{4}\phi^4. \tag{2.4}$$

The minimum of the potential, i.e. the vacuum expectation value (VEV), is then given by $\langle 0|\phi|0\rangle = v = \sqrt{\mu^2/\lambda}$. The field dependent squared masses of the Higgs boson and the Goldstone bosons are

$$\begin{aligned} m_h^2(\phi) &= 3\lambda\phi^2 - \mu^2, \\ m_\chi^2(\phi) &= \lambda\phi^2 - \mu^2 \end{aligned} \tag{2.5}$$

so that one obtains for the physical masses $m_h^2(v) = 2\lambda v^2$ and $m_\chi^2(v) = 0$. The Lagrangian is symmetric under the local gauge transformation

$$\Phi(x) \to \Phi'(x) = \exp[i\boldsymbol{\alpha}(x)\cdot\boldsymbol{\sigma}(x)/2]\Phi(x), \qquad (2.6)$$

where σ_i are the Pauli matrices. But the ground state, $\Phi = \frac{1}{\sqrt{2}}\binom{0}{v}$, spontaneously breaks this symmetry. The weak gauge bosons acquire their masses due to the coupling to the Higgs field via the covariant derivatives and the fermions become massive due to Yukawa coupling terms. The electroweak symmetry breaking is associated with a so-called phase transition.

In general, many systems in nature show a phase transition behavior, at which small changes in an external parameter, e.g. the temperature, result in a change of the macroscopic properties of the system. Let us mention for instance the transition between the fluid and gaseous state of water or the spontaneous magnetization of a ferromagnetic system. Usually a phase transition can be characterized by an order parameter, a macroscopic quantity, which vanishes in one phase and has a finite value in the other phase. The transition between the two phases can proceed in different ways. In the case of a first order PT the order parameter has a discontinuity and jumps from zero to a finite value. The two phases coexist for some time since bubbles of one phase nucleate and expand, surrounded by a background of the other phase. If the order parameter changes rapidly but continuously, and its first derivative is discontinuous, the PT is of second order. A third possibility is a smooth cross-over, which is strictly speaking no real phase transition. Here the change of the macroscopic properties as a function of temperature (or time) is less pronounced without any discontinuity. In the case of the electroweak phase transition (EWPT) the expectation value of the Higgs field may serve as an order parameter, since it is zero (or small) at temperatures above the PT temperature, so that the particle masses vanish, and non-zero in the broken phase. But it turned out that in the Standard Model the electroweak symmetry breaking proceeds as a cross-over instead of a phase transition [13–15]. Nevertheless the situation may change in extensions of the SM, so that the behavior of the Higgs field expectation value indicates a first order phase transition.

A first order PT offers the possibility for a departure from thermal equilibrium as is required by the Sakharov conditions for any baryogenesis scenario. The time scales of particle reactions then become larger than the time scales of the rapidly nucleating and expanding bubbles, which causes a non-equilibrium situation. The nature of a phase transition in an quantum field theory can be analyzed with the help of the so-called effective potential, which we will introduce in the following section.

2.2 The effective potential

Before discussing a quantum mechanical system let us first briefly review the pro-
ceeding in classical mechanics. A standard mechanism to determine whether the
phase transition of a classical system, e.g. a ferromagnet in an external magnetic field
H, is of first or second order, is to compute the Helmholtz free energy $F = -T \ln Z$,
where T is the temperature and Z the partition function. From F one can derive
thermodynamic functions, for instance the magnetization $M = -\frac{\partial F}{\partial H}\big|_T$, which is
the order parameter of the ferromagnetic system. Its behavior can be studied with
the Gibbs free energy G, the Legendre transformation of F. As a function of the
magnetization, G has a minimum for vanishing field H, which characterizes the most
stable state of the system.

An analogous mechanism has been developed for quantum field theories, leading us
to the effective potential. Detailed descriptions can be found in several text books,
e.g. [36–40], a review is also given in ref. [41]. In order to derive an expression for the
effective potential we consider the example of a scalar field ϕ with the Lagrangian

$$\mathscr{L} = \frac{1}{2}(\partial_\mu \phi)(\partial^\mu \phi) - V_0(\phi) \tag{2.7}$$

in the presence of an external field J. The energy functional $W[J]$, which is the gen-
erating functional of the connected correlation functions, is defined by the relation

$$Z[J] = e^{-iW[J]} = \int \mathcal{D}\phi\, e^{i\int \mathrm{d}^4 x(\mathscr{L}[\phi] + J\phi)}. \tag{2.8}$$

The functional derivative of $W[J]$ leads to the vacuum expectation value of the field
ϕ in the presence of the external source J, which is defined as the classical field ϕ_cl,

$$-\frac{\delta W[J]}{\delta J(x)} = \frac{\int \mathcal{D}\phi\, \phi(x) e^{i\int(\mathscr{L}[\phi] + J\phi)}}{\int \mathcal{D}\phi\, e^{i\int(\mathscr{L}[\phi] + J\phi)}} = \frac{\langle 0|\phi(x)|0\rangle_J}{\langle 0|0\rangle_J} = \phi_\mathrm{cl}(x). \tag{2.9}$$

The Legendre transformation of $W[J]$, which is the analogous quantity to the Gibbs
free energy, is called the effective action

$$\Gamma[\phi_\mathrm{cl}] = -W[J] - \int \mathrm{d}^4 y\, J(y)\phi_\mathrm{cl}(y). \tag{2.10}$$

Since the derivative of $\Gamma[\phi_\mathrm{cl}]$ with respect to $\phi_\mathrm{cl}(x)$ yields, apart from a minus sign,
the source term $J(x)$, the effective action satisfies the equation

$$\frac{\delta \Gamma[\phi_\mathrm{cl}]}{\delta \phi_\mathrm{cl}(x)} = 0 \tag{2.11}$$

if the external source is set to zero. Thus, the state ϕ_cl which is the solution of
eq. (2.11) represents the (meta) stable quantum state of the theory. If we consider

the Higgs potential it leads to the vacuum expectation value of the Higgs field, which serves as the order parameter of the EWPT.

The effective action has the meaning of a generating functional for the one-particle irreducible (1PI) Green functions $\Gamma^{(n)}$. It can be expanded in the series

$$\Gamma[\phi_{\mathrm{cl}}] = \sum_n \frac{1}{n!} \int \mathrm{d}^4 x_1 \ldots \mathrm{d}^4 x_n \, \phi_{\mathrm{cl}}(x_1) \ldots \phi_{\mathrm{cl}}(x_n) \, \Gamma^{(n)}(x_1, \ldots, x_n). \qquad (2.12)$$

$\Gamma^{(n)}$ is the sum of all 1PI diagrams with n external lines. Conventionally 1PI graphs are evaluated with no propagators on the external lines. Usually one considers a theory which is translationally invariant. Then the solution for ϕ_{cl} is constant and does not depend on x. With a Fourier transformation of the functions $\Gamma^{(n)}(x)$ into $\Gamma^{(n)}(p)$ one obtains for eq. (2.12) the expression

$$\Gamma[\phi_{\mathrm{cl}}] = \sum_n \frac{1}{n!} \int \mathrm{d}^4 x \, \phi_{\mathrm{cl}}^n \, \Gamma^{(n)}(p_i = 0). \qquad (2.13)$$

Now, starting from the effective action the effective potential V_{eff} is defined by the relation

$$\Gamma[\phi_{\mathrm{cl}}] = - \int \mathrm{d}^4 x \, V_{\mathrm{eff}}(\phi_{\mathrm{cl}}). \qquad (2.14)$$

The condition (2.11) that $\Gamma[\phi_{\mathrm{cl}}]$ has an extremum for the vacuum state of the system translates into the equation

$$\frac{\partial}{\partial \phi_{\mathrm{cl}}} V_{\mathrm{eff}}(\phi_{\mathrm{cl}}) = 0. \qquad (2.15)$$

The choice $J = 0$ also implies, using eq. (2.10), that $-\Gamma$ is the energy of the state ϕ_{cl} which solves eq. (2.11), or the equivalent eq. (2.15), and $V_{\mathrm{eff}} = -\frac{\Gamma}{\mathcal{V}\mathcal{T}}$ is the energy per volume $\mathcal{V}$ and time $\mathcal{T}$, i.e. the energy density.

Finally by comparing eqs. (2.13) and (2.14) one obtains an expression for the effective potential in terms of a series of 1PI functions,

$$V_{\mathrm{eff}}(\phi_{\mathrm{cl}}) = - \sum_n \frac{1}{n!} \phi_{\mathrm{cl}}^n \, \Gamma^{(n)}(p_i = 0). \qquad (2.16)$$

A useful approximative method for the computation of V_{eff} is the loop expansion. At tree level V_{eff} is just the classical potential V_0. In our work we will use the one-loop effective potential [42], whose derivation will be briefly sketched in the following.

One-loop effective potential at zero temperature

Let us illustrate the computation of the one-loop effective potential considering the example of a real scalar field with the tree-level potential

$$V_0 = \frac{1}{2} m^2 \phi^2 + \frac{\lambda}{4!} \phi^4. \qquad (2.17)$$

As stated above the zeroth order contribution to V_{eff} is V_0. At one-loop order one has to sum up the diagrams shown in fig. 2.1, where each of the n propagators gives a factor of $i/(p^2 - m^2 + i\varepsilon)$ and each vertex counts as $-i\lambda/2$. There is an integration over loop momenta and an additional symmetry factor of $1/2n$ because of the symmetry under reflections and rotations. Using the result (2.16) derived above yields for the one-loop contribution

$$
\begin{aligned}
V_1(\phi_{\text{cl}}) &= i \sum_n \int \frac{\mathrm{d}^4 p}{(2\pi)^4} \frac{1}{2n} \left(\frac{\lambda/2\phi_{\text{cl}}^2}{p^2 - m^2 + i\varepsilon} \right)^n \\
&= -\frac{i}{2} \int \frac{\mathrm{d}^4 p}{(2\pi)^4} \ln\left(1 - \frac{\lambda/2\phi_{\text{cl}}^2}{p^2 - m^2 + i\varepsilon} \right) \\
&= \frac{1}{2} \int \frac{\mathrm{d}^4 p_E}{(2\pi)^4} \ln\left(1 + \frac{\lambda/2\phi_{\text{cl}}^2}{p_E^2 + m^2} \right)
\end{aligned}
\tag{2.18}
$$

where we performed a Wick rotation to Euclidean momenta in the last step. If one finally introduces the shifted mass $m^2(\phi_{\text{cl}}) = \frac{\partial^2}{\partial \phi_{\text{cl}}^2} V_0$ and ignores an irrelevant field-independent term the one-loop contribution reads

$$
V_1(\phi_{\text{cl}}) = \frac{1}{2} \int \frac{\mathrm{d}^4 p_E}{(2\pi)^4} \ln\left(p_E^2 + m^2(\phi_{\text{cl}}) \right) .
\tag{2.19}
$$

Unfortunately this integral is ultraviolet divergent and has to be renormalized. Therefore the theory must be regularized and the infinities have to be absorbed in counter terms. Common regularization methods are e.g. the cut-off or the dimensional regularization. Both result in an expression of the form

$$
V_1(\phi_{\text{cl}}) = \frac{1}{64\pi^2} m^4(\phi_{\text{cl}}) \left(\ln \frac{m^2(\phi_{\text{cl}})}{Q^2} - C \right)
\tag{2.20}
$$

where Q is a renormalization scale and C depends on the regularization scheme. For instance in the $\overline{\text{MS}}$ scheme one has $C = 3/2$. In this work we will use $C = 0$, which
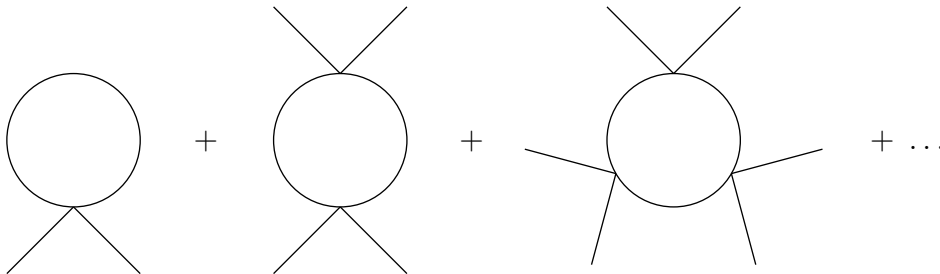

Figure 2.1: 1PI diagrams contributing to the one-loop effective potential for the example (2.17).

corresponds to absorbing a different constant into the ultraviolet divergent term. We also do not need to specify explicitly the counter terms, since we are only interested in the effective potential, which is finite. In the theories under consideration we take into account in each case the heaviest particles, since they contribute mainly to the one-loop effective potential. These are the top quark in the model with a dimension-six Higgs operator and in addition the four heavy Higgs bosons in the two-Higgs doublet model. In general we therefore use the Coleman-Weinberg type expression [42]

$$V_1(\phi_{\rm cl}) = \pm \sum_{B,F} n_{B(F)} \frac{1}{64\pi^2} m_{B(F)}^4(\phi_{\rm cl}) \ln \frac{m_{B(F)}^2(\phi_{\rm cl})}{Q^2} \qquad (2.21)$$

including the degrees of freedom $n_{B(F)}$, where "$+(-)$" applies to bosons (fermions). Up to now we only dealt with the effective potential at zero temperature. Of course for the analysis of the EWPT we need the corresponding method also for finite temperature.

One-loop effective potential at finite temperature

A simple way to derive the desired result for finite temperature is to start from eq. (2.19) and translate the $T = 0$ expressions into $T \neq 0$ terms. One has to perform the substitutions

$$p_E^2 = p_{E0}^2 + \mathbf{p}^2 \qquad \rightarrow \qquad \omega_n^2 + \mathbf{p}^2, \qquad (2.22)$$

$$\int \frac{{\rm d}^4 p}{(2\pi)^4} \qquad \rightarrow \qquad T \sum_n \int \frac{{\rm d}^3 p}{(2\pi)^3} \qquad (2.23)$$

where $\omega_n = 2n\pi T$ are the bosonic Matsubara frequencies, which we consider in this example. The corresponding fermionic frequencies read $\omega_n = (2n+1)\pi T$. With the substitutions (2.22) and (2.23) eq. (2.19) translates into

$$V_{1,{\rm T}}(\phi_{\rm cl}) = \frac{T}{2} \sum_n \int \frac{{\rm d}^3 p}{(2\pi)^3} \ln \left(\omega_n^2 + \omega^2 \right) \qquad (2.24)$$

with $\omega^2 = \mathbf{p}^2 + m^2(\phi_{\rm cl})$. After performing the Matsubara sum and dropping a $\phi_{\rm cl}$-independent term one obtains [43]

$$V_{1,{\rm T}}(\phi_{\rm cl}) = \int \frac{{\rm d}^3 p}{(2\pi)^3} \left(\frac{\omega}{2} + T \ln \left(1 - e^{-\omega/T} \right) \right). \qquad (2.25)$$

The first part of the integral, which is temperature independent, represents the $T = 0$ one-loop contribution (2.19). Let us restrict to the part $\Delta V_{\rm eff,T}$ containing

the temperature dependence. The integration over the solid angle can be easily performed and one is left with the expression

$$\Delta V_{\text{eff,T}} = \frac{T^4}{2\pi^2} \int_0^\infty \mathrm{d}x\, x^2 \ln\left(1 - e^{-\sqrt{x^2 + (m/T)^2}}\right). \tag{2.26}$$

This integral is defined as the thermal bosonic function

$$f_{\text{B}}(m_B/T) = \frac{1}{2\pi^2} \int_0^\infty \mathrm{d}x\, x^2 \ln\left(1 - e^{-\sqrt{x^2 + (m/T)^2}}\right). \tag{2.27}$$

In an analogous manner one derives for fermion fields the thermal fermionic function

$$f_{\text{F}}(m_F/T) = -\frac{1}{2\pi^2} \int_0^\infty \mathrm{d}x\, x^2 \ln\left(1 + e^{-\sqrt{x^2 + (m/T)^2}}\right). \tag{2.28}$$

Including again possible degrees of freedom $n_{B(F)}$ for bosons (fermions) the thermal contribution to the one-loop effective potential is then given by [43]

$$\Delta V_{\text{eff,T}} = T^4 \sum_B n_B\, f_{\text{B}}(m_B/T) + T^4 \sum_F n_F\, f_{\text{F}}(m_F/T). \tag{2.29}$$

There exist useful approximations of f_{B} and f_{F} for the high $(m/T \ll 1)$ and low temperature limit $(m/T \gg 1)$. The expansions in powers of $x = m/T$ read for high temperatures [44]

$$
\begin{aligned}
f_{\text{B}}^{\text{HT}}(x) &= \frac{-\pi^2}{90} + \frac{x^2}{24} - \frac{x^3}{12\pi} - \frac{x^4}{64\pi^2} \ln\frac{x^2}{c_{\text{B}}} \\
&\quad + \frac{x^2}{2} \sum_{n=2}^\infty \left(-\frac{x^2}{4\pi^2}\right)^n \frac{(2n-3)!!\,\zeta(2n-1)}{(2n)!!\,(n+1)}, \\
f_{\text{F}}^{\text{HT}}(x) &= \frac{-7\pi^2}{720} + \frac{x^2}{48} + \frac{x^4}{64\pi^2} \ln\frac{x^2}{c_{\text{F}}} \\
&\quad - \frac{x^2}{2} \sum_{n=2}^\infty \left(-\frac{x^2}{4\pi^2}\right)^n \frac{(2n-3)!!\,\zeta(2n-1)}{(2n)!!\,(n+1)}(2^{2n-1} - 1)
\end{aligned}
\tag{2.30}
$$
$$\tag{2.31}$$

with $c_{\text{F}} = \pi^2 \exp(3/2 - 2\gamma_e) \approx 13.94$ and $c_{\text{B}} = 16 c_{\text{F}}$ and for low temperatures [45]

$$
\begin{aligned}
f^{\text{LT}}(x) &= f_{\text{B}}^{\text{LT}}(x) = f_{\text{F}}^{\text{LT}}(x) \\
&= -\left(\frac{x}{2\pi}\right)^{3/2} e^{-x} \sum_{n=2}^\infty \frac{1}{2^n n!} \frac{\Gamma(5/2 + n)}{\Gamma(5/2 - n)} x^{-n}.
\end{aligned}
\tag{2.32}
$$

Now, we have derived a tool for the analysis of the EWPT. The dynamics of the phase transition is governed by the finite temperature effective potential, which consists of the tree-level potential and to one-loop order of the contributions (2.21) and (2.29). In the following we neglect the subscript "cl" of the classical field, since it should be obvious that we mean ϕ_{cl} when dealing with V_{eff}.

2.3 The strength of the phase transition

As already mentioned phase transitions can be categorized as first or higher order transitions. The typical evolution of an effective potential is shown in fig. 2.2 for these two cases, where we need not specify a concrete model. At high temperature (cf. dotted red curves) the effective potential has only one minimum, located at the origin. In a first order PT a second, broken local minimum develops with decreasing temperature, which becomes degenerated with the first one at the so-called critical temperature T_c (solid black curve). The two minima are separated by an energy barrier. At $T < T_c$ the second minimum becomes the global one and finally the energy barrier disappears (dashed blue curve). In the case of a continuous order transition there is always only one minimum, which evolves smoothly from the origin to $\phi > 0$. The critical temperature is then defined by the condition that the curvature at $\phi = 0$ vanishes, i.e. $V''_{\text{eff}}(0) = 0$. Above T_c, $V_{\text{eff}}(0)$ is a minimum of the potential, and below T_c it becomes a maximum.

An important quantity to characterize a phase transition is the strength ξ, which is defined as

$$\xi = \frac{\phi_c}{T_c} \tag{2.33}$$

where ϕ_c is the location of the broken minimum at $T = T_c$. Of course, according to this definition, a non-vanishing strength makes only sense for a first order phase transition. Anyway, we are interested in a first order transition to fulfill the requirement of departure from thermal equilibrium. Moreover, an additional constraint arises for successful baryogenesis. The so-called "washout criterion" has to be satisfied [46, 47], i.e.

$$\xi \gtrsim 1, \tag{2.34}$$

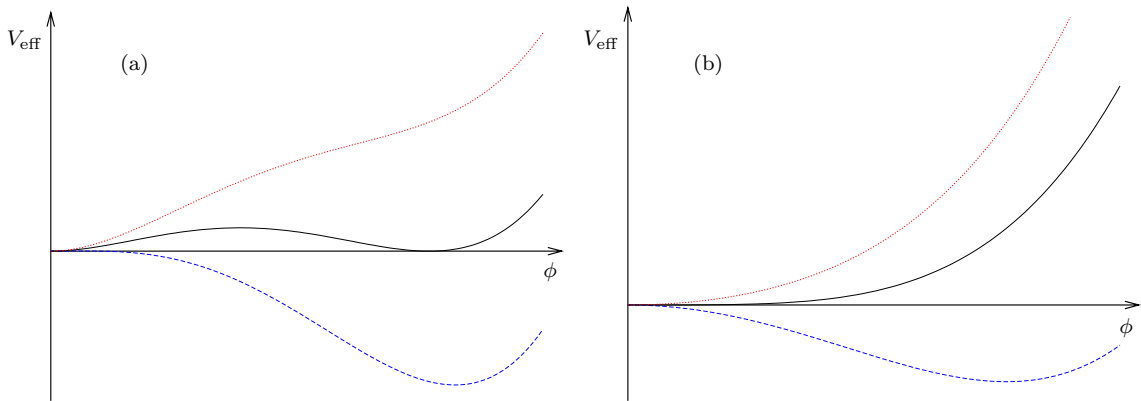Figure 2.2: Evolution of the effective potential with temperature. Dotted red: $T > T_c$, solid black: $T = T_c$, dashed blue: $T < T_c$. Part (a) shows a first and (b) a second order PT.

in order to prevent a washout of the generated baryon asymmetry by sphaleron processes after the PT. We will discuss sphalerons in more detail in section 3.2. In the case of $\xi \gtrsim 1$ the phase transition is called "strong".

In the Standard Model the strength of the phase transition has been investigated in dependence on the Higgs mass [13–18]. A strong first order transition is only realized for Higgs masses $m_h \lesssim 40$ GeV. It is of first order, but weak up to $m_h \approx 72$ GeV, where the transition changes into a crossover [48–50]. Since the LEP2 experiments established a much larger lower bound for the mass of the SM Higgs boson, $m_h > 114$ GeV [19], the transition between the symmetric and broken phase is just a smooth cross-over. Thus, the SM does not fulfill the Sakharov condition of a departure from thermal equilibrium. However, let us continue with the discussion of a first order phase transition and focus on the Higgs bubbles which begin to nucleate at this transition.

2.4 Bubble formation

During a first order phase transition, when the broken minimum becomes the global one, a thermal tunneling process from the metastable vacuum into the true vacuum starts.[1] Bubbles of the new phase begin to nucleate, they expand and finally percolate.

In quantum mechanics, i.e. at zero temperature, the dynamics of tunneling can be described in the semiclassical theory as developed by Coleman [51]. Let us illustrate the procedure considering as example a scalar field ϕ with a potential $V(\phi)$ normalized to $V(\phi_{\mathrm{sym}} = 0) = 0$. In order to compute the probability for tunneling the Euclidean equation of motion has to be solved first,

$$\Box\phi - \frac{\mathrm{d}V}{\mathrm{d}\phi} = \frac{\mathrm{d}^2\phi}{\mathrm{d}\tau^2} + \nabla^2\phi - \frac{\mathrm{d}V}{\mathrm{d}\phi} = 0 \tag{2.35}$$

with the boundary conditions $\phi \to 0$ for $\tau \to \pm\infty$ and $\mathrm{d}\phi/\mathrm{d}\tau = 0$ for $\tau = 0$. The tunneling probability per unit time and unit volume is then given by

$$\Gamma = A\,e^{-S_4} \tag{2.36}$$

where S_4 is the Euclidean action for the solution of eq. (2.35),

$$S_4[\phi] = \int \mathrm{d}\tau\,\mathrm{d}^3x \left[\frac{1}{2}\left(\frac{\mathrm{d}\phi}{\mathrm{d}\tau}\right)^2 + \frac{1}{2}\left(\nabla\phi\right)^2 + V(\phi) \right]. \tag{2.37}$$

---

[1]At finite temperature the transition is not a tunneling process in the quantum mechanical sense, but is driven by thermal fluctuations. Since the occurrence of such processes is described in terms of probabilities, it is often called a "tunneling" mechanism in analogy to the quantum mechanical probability description.

The tunneling rate at finite temperature is derived in an analogous way, taking into account that finite temperature field theory is equivalent to Euclidean field theory with periodicity T^{-1} in the imaginary "time" direction τ. The potential V has to be replaced by the thermal effective potential $V_{\text{eff,T}}$ [52]. For large temperatures one expects a O(3) symmetric solution $\phi = \phi(r = |\mathbf{x}|)$. Then eq. (2.37) is reduced by integration over τ to $S_4 = S_3/T$ with the three-dimensional Euclidean action [52–54]

$$
\begin{aligned}
S_3[\phi] &= \int \mathrm{d}^3 x \left[\frac{1}{2} (\nabla \phi)^2 + V_{\text{eff,T}}(\phi) \right] \\
&= 4\pi \int_0^\infty \mathrm{d}r \, r^2 \left[\frac{1}{2} \left(\frac{\mathrm{d}\phi}{\mathrm{d}r} \right)^2 + V_{\text{eff,T}}(\phi) \right]
\end{aligned}
\tag{2.38}
$$

and the equation of motion simplifies to

$$
\frac{\mathrm{d}^2 \phi}{\mathrm{d}r^2} + \frac{2}{r} \frac{\mathrm{d}\phi}{\mathrm{d}r} - \frac{\mathrm{d}V_{\text{eff,T}}}{\mathrm{d}\phi} = 0
\tag{2.39}
$$

with the boundary conditions $\phi \to 0$ for $\tau \to \infty$ and $\mathrm{d}\phi/\mathrm{d}r = 0$ for $r = 0$. At finite temperature the probability for tunneling per unit time and unit volume is given by [52]

$$
\Gamma = A(T) \, e^{-S_3/T} \sim T^4 \, e^{-S_3/T}.
\tag{2.40}
$$

The computation of the temperature dependent prefactor A is rather complicated, but in general it is sufficient to have a rough estimate, and one finds on dimensional grounds $A \sim \mathcal{O}(T^4)$. Moreover, the dominant contribution comes from the exponential, not from the factor A, so that its precise value is not needed [45].

The bubble nucleation starts at the nucleation temperature T_n somewhat below the critical temperature T_c when the tunneling probability inside a causal volume is of the order one. This corresponds to the condition [45]

$$
\frac{S_3(T_n)}{T_n} \sim 130 - 140.
\tag{2.41}
$$

When the energy difference $\Delta V = V_{\text{eff,T}}(\phi_{\text{sym}}) - V_{\text{eff,T}}(\phi_{\text{bkr}})$ between the two minima of the potential is small compared to the height of the potential barrier V_b then the radius of the bubble becomes much larger than the thickness of the bubble wall [52]. This allows further approximations in the so-called "thin wall limit". Under such an assumption the friction term in eq. (2.39) can be neglected, which reduces it to the equation describing tunneling in one-dimensional space.

$$
\frac{\mathrm{d}^2 \phi}{\mathrm{d}z^2} - \frac{\mathrm{d}V_{\text{eff,T}}}{\mathrm{d}\phi} = 0.
\tag{2.42}
$$

Note that in this case we renamed the variable r into z which indicates that $\phi(z)$ describes no longer a spherical solution, but a domain wall. The boundary conditions

translate into $\phi \to \phi_{\mathrm{brk}}$ for $z \to -\infty$ and $\phi \to \phi_{\mathrm{sym}}$ for $z \to \infty$. In the limit $\Delta V \to 0$ the solution of the equation of motion is [52]

$$\frac{\mathrm{d}\phi}{\mathrm{d}z} = -\sqrt{2V_{\mathrm{eff,T}}} \qquad \Rightarrow \qquad z = \int_\phi^{\phi_{\mathrm{brk}}} \frac{\mathrm{d}\phi'}{\sqrt{2V_{\mathrm{eff,T}}}}. \tag{2.43}$$

In the thin wall limit the three-dimensional action can be expressed in terms of the bubble radius R, the energy difference ΔV and the surface tension, which is equal to the action S_1 corresponding to the one-dimensional theory,

$$S_3 = -\frac{4}{3}\pi R^3 \Delta V + 4\pi R^2 S_1 \tag{2.44}$$

with the surface tension

$$S_1 = \int_0^\infty \mathrm{d}r \left[\frac{1}{2}\left(\frac{\mathrm{d}\phi}{\mathrm{d}r}\right)^2 + V_{\mathrm{eff,T}}(\phi) \right] = \int_{\phi_{\mathrm{sym}}}^{\phi_{\mathrm{brk}}} \mathrm{d}\phi \sqrt{2V_{\mathrm{eff,T}}}. \tag{2.45}$$

The bubble radius R is obtained by maximization of eq. (2.44), which gives

$$R = \frac{2S_1}{\Delta V}. \tag{2.46}$$

Thus, the final result for S_3 in the thin wall approximation reads

$$S_3 = \frac{16\pi S_1^3}{\Delta V^2}. \tag{2.47}$$

Let us now consider a concrete example. A quite simple potential which has two degenerate minima at $\phi_{\mathrm{sym}} = 0$ and $\phi_{\mathrm{brk}} = v$ and which fulfills the above requirements is

$$V(\phi) = \frac{\lambda}{4}\phi^2(\phi - v)^2. \tag{2.48}$$

The potential barrier is located at $\phi = v/2$ with the height $V_b = \lambda/64\, v^4$ and the solution of the equation of motion (2.42) is the function

$$\phi(z) = \frac{v}{2}\left(1 - \tanh\frac{z}{L_{\mathrm{w}}}\right) \tag{2.49}$$

where the wall thickness L_{w} is given by

$$L_{\mathrm{w}} = \sqrt{\frac{8}{\lambda v^2}} = \frac{v}{\sqrt{8V_b}}. \tag{2.50}$$

This formula will give us also for more complex potentials a rough, but rather simple approximation for the wall thickness.

The wall profile (2.49) is shown in fig. 2.3 where also the thickness of the bubble
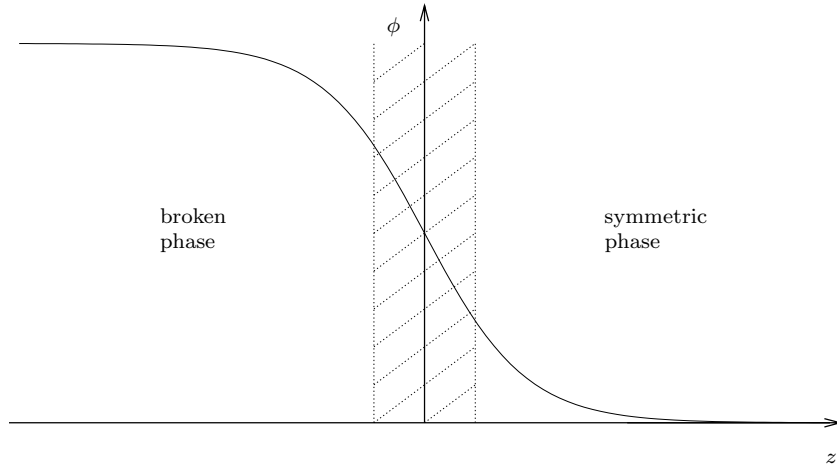
Figure 2.3: Illustration of the bubble wall profile according to eq. (2.49).

wall is indicated. In the wall frame the center of the wall is fixed at $z = 0$. In the plasma frame the wall passes with a velocity v_{w} through the plasma and the particles interact with the boundary so that finally due to B-violating processes a net baryon number is frozen in the broken phase.

Let us finally comment on the wall velocity v_{w}. An estimate is given by Moore, who takes into account only the friction related to the infrared gauge field modes [55],

$$v_{\mathrm{w}} = \frac{32\pi L_{\mathrm{w}}}{11 g_2^2 T^3} \frac{\Delta V}{\ln(m_W L_{\mathrm{w}}) + \mathcal{O}(1)}, \qquad (2.51)$$

where g_2 is the $SU(2)$ coupling constant and m_W the W boson mass. This equation breaks down for large values of v_{w}. As we will see eq. (2.51) leads to a wall velocity of order unity in the case of a strong first order phase transition, which we are interested in. Thus the result is not reliable and we will treat v_{w} as a free parameter.

Chapter 3

Electroweak Baryogenesis

3.1 Introductory remarks

The electroweak phase transition offers in principle the possibility for a baryogenesis scenario if the PT is strongly first order. In addition CP-violating interactions as well as baryon number non-conserving processes are needed. The latter will be discussed in more detail in the following section. Here we first outline some general ideas for electroweak baryogenesis. Reviews of this topic can be found e.g. in refs. [56, 57]. The mechanism is based on CP-violating interactions of the particles in the plasma with the bubble wall, which create an excess in the left-handed quark density. Starting with a zero net baryon number in the symmetric phase and an equal amount of left- and right-handed quarks and antiquarks, one ends up with more left-handed particles than antiparticles and correspondingly with more right-handed antiparticles than particles. Note that there is not yet a B asymmetry. This is generated by sphaleron processes in front of the bubbles, i.e. the excess in the left-handed quark density is converted into an excess of particles over antiparticles. When the bubble wall sweeps over this region, the sphaleron rate is immediately switched off if the phase transition is strong enough, and the B-violating back-reactions are blocked. Thus, the baryon asymmetry is frozen in inside the bubbles, which expand, percolate and finally become our observable world.

3.2 CP- and B-violation in the Standard Model

It is well known that the weak interactions in the Standard Model violate CP. This fact is experimentally confirmed in the Kaon and B-meson systems and can

be theoretically explained due to the Cabibbo-Kobayashi-Maskawa (CKM) mixing matrix V_{CKM} [58]. The CKM matrix appears in the charged quark current

$$J_{cc}^{\mu} = \bar{u}_L \gamma^{\mu} V_{\mathrm{CKM}} d_L \tag{3.1}$$

which couples to the W bosons, where u and d denote the up- and down-type quarks, respectively. A phase $\delta_{\mathrm{CKM}} \neq 0$ or π in the CKM matrix is the source of CP-violation. The effects observed in the Kaon and B-meson systems can be well described by this mechanism. However, the amount of CP-violation is too small to produce a sufficiently large baryon number in an electroweak baryogenesis scenario [59–61]. Thus, one needs additional sources of CP-non-conservation. We will discuss such sources in more detail in the context of the two models under consideration in chapters 4 and 5.

Also baryon number violation is included in the Standard Model, although in present day experiments baryon, as well as lepton number, are good quantum numbers, which are conserved. As we will see B-violating processes are suppressed at today's temperatures and can therefore be neglected, but they were significant in the early universe at much higher temperatures. Let us briefly outline the non-perturbative origin of B- and also L-violation in the following.
The SM Lagrangian has a global $U(1)_B$ and $U(1)_L$ symmetry. Due to Noether's theorem one obtains at the Born level the conserved currents J_{μ}^B and J_{μ}^L,

$$\partial^{\mu} J_{\mu}^B = \partial^{\mu} \sum_q \frac{1}{3} \bar{q} \gamma_{\mu} q = 0, \tag{3.2}$$

$$\partial^{\mu} J_{\mu}^L = \partial^{\mu} \sum_l \bar{l} \gamma_{\mu} l = 0. \tag{3.3}$$

However, these equations no longer hold beyond the Born approximation because of the triangle (or Adler-Bell-Jackiw) anomaly [62, 63]. At quantum level one obtains the equation

$$\partial^{\mu} J_{\mu}^B = \partial^{\mu} J_{\mu}^L = \frac{n_F}{32\pi^2} (-g_2^2 W_{\mu\nu}^a \widetilde{W}^{a\mu\nu} + g_1^2 B_{\mu\nu} \widetilde{B}^{\mu\nu}) \tag{3.4}$$

where n_F is the number of generations, g_2 and g_1 are the $SU(2)$ and $U(1)$ gauge couplings and $W_{\mu\nu}^a$ as well as $B_{\mu\nu}$ the corresponding field strength tensors. This relation implies that the difference $J_{\mu}^B - J_{\mu}^F$ is still conserved. The right hand side of eq. (3.4) can be written as a divergence of a current K^{μ}, and it can be shown that a change in the baryon and lepton number coincides with a change of gauge field configurations according to

$$\Delta B = \Delta L = n_F \int \mathrm{d}^4 x \, \partial_{\mu} K^{\mu} = n_F \left[N_{\mathrm{CS}}(t_{\mathrm{f}}) - N_{\mathrm{CS}}(t_{\mathrm{i}}) \right] = n_F \, \Delta N_{\mathrm{CS}} \tag{3.5}$$
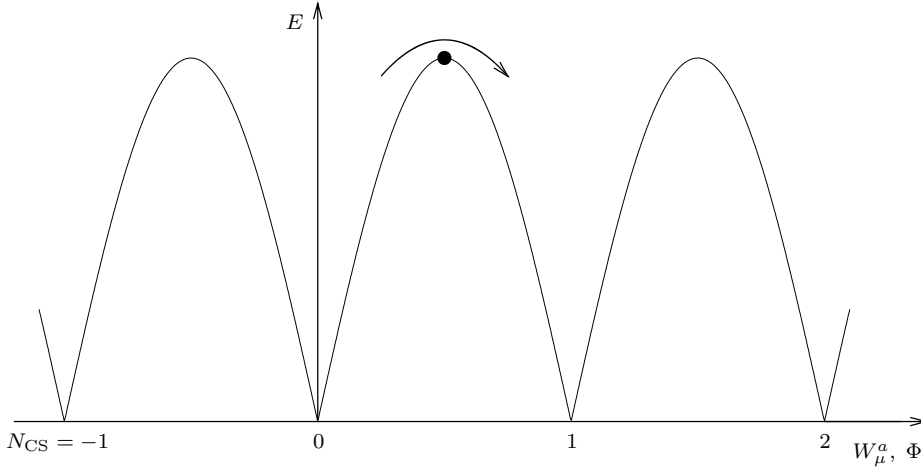
Figure 3.1: Schematic sketch of the energy of the gauge and Higgs field configu-
rations. The dot represents a sphaleron configuration. The indicated
transition changes the Chern-Simons number form 0 to 1.

where

$$N_{\mathrm{CS}} = \frac{g_2^2}{32\pi^2} \int \mathrm{d}^3x\, \varepsilon_{ijk} \left(W^{aij}W^{ak} - \frac{g_2}{3}\varepsilon^{abc}W^{ai}W^{bj}W^{ck} \right) \tag{3.6}$$

is the Chern-Simons number, which assigns a topological "charge" to the gauge
fields. N_{CS} itself depends on the gauge, but the difference ΔN_{CS} is gauge inde-
pendent. The electroweak theory has an infinite number of topologically different
vacuum states, characterized by N_{CS}. Fig. 3.1 illustrates the energy functional for
different gauge and Higgs field configurations, simplified to one dimension. The tran-
sition from one to a neighboring vacuum, separated by an energy barrier, changes
the Chern-Simons number by one. Therefore with $n_F = 3$ generations the baryon
and lepton numbers also change by

$$\Delta B = \Delta L = 3. \tag{3.7}$$

Thus, we have $(B+L)$-violation and $(B-L)$-conservation.

At zero temperature a transition through the barrier is classically forbidden, but
in principle possible via a tunneling process in quantum mechanics. However, the
probability is exponentially suppressed with a factor $\exp(-4\pi/\alpha_w) \approx 10^{-164}$, taking
$\alpha_w \approx 1/30$ [64, 65]. Therefore *B*- or *L*-violation is not observable at present-day
collider experiments.

At high temperatures the situation changes. The energy barrier between two vacua
can be overcome by thermal fluctuations. The gauge and Higgs field configuration
indicated with the dot in fig. 3.1 is called a "sphaleron", a saddle-point solution of the
classical field equations with half-integer Chern-Simons number [66, 67]. The energy
scale is given by the height of the barrier, which depends on the Higgs expectation

value $v_T = \langle 0|\Phi|0\rangle_T$ at finite temperature,

$$E_{\text{sph}} = \frac{4\pi}{g_2}\, v_T\, B(m_h/m_W) \tag{3.8}$$

where the function B is of $\mathcal{O}(1)$ [67]. For temperatures $T < T_c$, i.e. in the broken phase, the probability for the system to be found at the saddle-point solution and therefore the rate for sphaleron induced $(B + L)$-violating transitions is given by

$$\Gamma \sim \exp(-E_{\text{sph}}(T)/T). \tag{3.9}$$

For the symmetric phase, at $T > T_c$, the calculation of the sphaleron rate is rather difficult. Recent investigations yield [68, 69]

$$\Gamma \sim \ln(1/\alpha_w)\alpha_w^5 T^4. \tag{3.10}$$

Above the electroweak scale of $T \approx 100$ GeV up to about $T \approx 10^{12}$ GeV this rate exceeds the expansion rate of the universe, so that $(B + L)$-violating processes are efficient. Below the EWPT temperature the sphaleron processes are switched off if E_{sph} and therefore v_T are sufficiently large, which corresponds to the condition $E_{\text{sph}}(T_c)/T_c > 45$ [46, 47]. Otherwise, if the sphaleron processes are still rapid, a baryon asymmetry which is generated at the EWPT would be washed out afterwards. This translates into the before mentioned washout criterion (2.34), the requirement of a strong first order phase transition.

3.3 The semiclassical force

If the bubble wall is thick in comparison with the inverse critical temperature the interactions of the particles in the plasma with the wall can be treated in the WKB approximation. Due to CP-violation different dispersion relations and different semiclassical forces for particles and antiparticles arise. Since the largest contribution to the baryon asymmetry comes from top quark transport, one can restrict to the case of a single massive Dirac fermion. In the presence of CP-violation one has to consider a complex top mass term $\text{Re}(\mathcal{M}) + i\gamma^5\text{Im}(\mathcal{M})$ with

$$\mathcal{M} = m(z)e^{i\theta(z)} \tag{3.11}$$

where z denotes the coordinate perpendicular to the wall. If the momentum of the particle, which is typically of the order of the temperature, is much larger than L_{w}^{-1}, i.e. $TL_{\text{w}} \gg 1$, a WKB ansatz is justified. The WKB approach was used in several works studying electroweak baryogenesis in extensions of the SM [70–78]. Here we

follow the treatment of ref. [77]. A more detailed description of this procedure is presented in ref. [79]. The Dirac equation can be solved with the ansatz

$$\Psi \sim e^{-i\omega t + i \int^z p_{cz}(z')\mathrm{d}z'} \tag{3.12}$$

where p_{cz} is the canonical momentum in the z-direction. An expansion in gradients of $\mathcal{M}$ is then performed. The dispersion relation to first order in gradients reads

$$\omega = \sqrt{(p_{cz} - \delta_{CP})^2 + m^2} \mp \frac{s\theta'}{2} \tag{3.13}$$

where the upper (lower) sign corresponds to particles (antiparticles) and $s = +1\,(-1)$ to z-spin up (down). The prime denotes the derivative with respect to z. We introduced $\delta_{CP} = \delta' \pm \theta'/2$, which arises from an ambiguity in the definition of the canonical momentum, since one can replace Ψ by $e^{i\delta(z)}\Psi$. It was shown in refs. [71, 72] that δ_{CP} drops out when expressing all quantities in terms of the kinetic momentum. First one has to generalize the dispersion relation (3.13) by a boost to a general Lorentz frame. It was the main result of ref. [77] that then the corresponding equations of refs. [80, 81], in which the computations were performed in the Schwinger-Keldysh formalism, can be reproduced. The boost is carried out by replacing $\omega^2 \rightarrow \omega^2 + p_x^2 + p_y^2$, where we do not have to distinguish between canonical and kinetic momentum parallel to the wall. After using the relation between the kinetic z-momentum p_z and the energy ω, $p_z = \omega\, v_{gz}$, where v_{gz} is the group velocity of the WKB wave-packet, one finds for the dispersion relation to first order in gradients

$$E = E_0 \pm \Delta E = E_0 \mp s\frac{\theta' m^2}{2E_0 E_{0z}} \tag{3.14}$$

with $E_0 = \sqrt{p_x^2 + p_y^2 + p_z^2 + m^2}$ and $E_{0z} = \sqrt{p_z^2 + m^2}$. The symbol E denotes the energy in dependence of the kinetic momentum. The group velocity is given by

$$v_{gz} = \frac{p_z}{E_0}\left(1 \pm s\frac{\theta' m^2}{2E_0^2 E_{0z}}\right) \tag{3.15}$$

and the force in the z-direction which acts on a particle in the plasma reads

$$F_z = \dot{p}_z = -\frac{(m^2)'}{2E_0} \pm s\frac{(m^2\theta')'}{2E_0 E_{0z}} \mp s\frac{\theta' m^2 (m^2)'}{4E_0^3 E_{0z}}. \tag{3.16}$$

Note that the phase δ no longer appears in the above equations. According to eq. (3.16) different forces act on particles and antiparticles. This difference is second order in derivatives and arises due to the CP-violation. The CP-conserving part is only first order in derivatives.

3.4 Transport equations

Usually electroweak baryogenesis is described by a set of transport equations for the particle types in the hot plasma. In the semiclassical approximation the distributions f_i for each fluid of particle type i can be described by a Boltzmann equation in the rest frame of the wall,

$$(v_{gz}\partial_z + F_z\partial_{p_z})f_i = \mathcal{C}_i[f] \tag{3.17}$$

where the explicit time dependence drops, since we are looking for stationary solutions. The $\mathcal{C}_i$ are the collision terms summarizing the particle interactions which drive the system back to equilibrium. The fluid type ansatz for the phase space distributions in the equilibrium case is given by

$$f_i^{(\text{eq})}(z, p_z, p) = \frac{1}{e^{\beta\gamma_{\text{w}}(E_i+v_{\text{w}}p_z)} \pm 1} \tag{3.18}$$

where $\beta = 1/T$ is the inverse temperature, v_{w} denotes the wall velocity, $\gamma_{\text{w}} = 1/\sqrt{1-v_{\text{w}}^2}$ and plus (minus) refers to fermions (bosons). Due to the translational invariance parallel to the wall f_i only depends on z, p_z and $p = |\mathbf{p}|$. We model the deviations from the equilibrium particle densities with chemical potentials $\mu_i(z)$ and describe the movement of the particles in response to the force by perturbations δf_i. Thus, we use the following ansatz, which is inserted in the Boltzmann equation (3.17),

$$f_i(z, p_z, p) = \frac{1}{e^{\beta[\gamma_{\text{w}}(E_i+v_{\text{w}}p_z)-\mu_i]} \pm 1} + \delta f_i(z, p_z, p). \tag{3.19}$$

The δf_i do not contribute to the particle density, i.e. $\int \mathrm{d}^3 p\, \delta f_i = 0$. The perturbations are equal for particles and antiparticles to first order in derivatives, but have CP-even and CP-odd parts to second order. Therefore, we split them up as follows

$$\mu_i = \mu_{i,1\text{e}} + \mu_{i,2\text{o}} + \mu_{i,2\text{e}}, \qquad \delta f_i = \delta f_{i,1\text{e}} + \delta f_{i,2\text{o}} + \delta f_{i,2\text{e}}. \tag{3.20}$$

The distribution functions are expanded to second order in derivatives and after plugging these expansions into eq. (3.17) the results for particles and antiparticles are subtracted. The CP-odd parts of μ_i and δf_i drop out and the difference in particles and antiparticles is determined by

$$\mu_{i,2} = \mu_{i,2\text{o}} - \bar{\mu}_{i,2\text{o}}, \qquad \delta f_{i,2} = \delta f_{i,2\text{o}} - \bar{\delta} f_{i,2\text{o}}. \tag{3.21}$$

For the first order parts we take

$$\mu_{i,1} = \mu_{i,1\text{e}} + \bar{\mu}_{i,1\text{e}}, \qquad \delta f_{i,1} = \delta f_{i,1\text{e}} + \bar{\delta} f_{i,1\text{e}}. \tag{3.22}$$

The Boltzmann equations are averaged over momentum, weighted by 1 and p_z/E_0. Expanding also in the wall velocity up to linear order one ends up with the following

two equations for each particle type, where we omit the index i to simplify the notation

$$v_{\rm w}K_1\mu_2' + v_{\rm w}K_2(m^2)'\mu_2 + u_2' - \langle \mathcal{C}[f] \rangle \;=\; S_\mu \tag{3.23}$$

$$-K_4\mu_2' + v_{\rm w}\tilde{K}_5u_2' + v_{\rm w}\tilde{K}_6(m^2)'u_2 - \left\langle \frac{p_z}{E_0}\mathcal{C}[f] \right\rangle \;=\; S_\theta + S_u. \tag{3.24}$$

The source terms on the right hand sides are given by

$$S_\mu \;=\; K_7 m^2\theta'\mu_1' \tag{3.25}$$
$$S_\theta \;=\; -v_{\rm w}K_8(m^2\theta')' + v_{\rm w}K_9 m^2\theta'(m^2)' \tag{3.26}$$
$$S_u \;=\; -\tilde{K}_{10}m^2\theta'u_1'. \tag{3.27}$$

The coefficients K and $\tilde{K}$ are momentum averages, which contain the equilibrium distributions or its derivatives, normalized with the averaged massless Fermi-Dirac distribution. Here we will not go into further details, the particular definitions are listed in ref. [77]. In general these coefficients are z-dependent due to the z-dependence of the mass of the particle type under consideration. With u we denote the plasma velocities, given by the average including the perturbations δf,

$$u_2 = \left\langle \frac{p_z}{E_0}\delta f_2 \right\rangle. \tag{3.28}$$

The collision integrals which appear in eqs. (3.23) and (3.24) can be written in terms of inelastic and total interaction rates [72]

$$\langle \mathcal{C}[f] \rangle \;=\; \Gamma^{\rm inel}\sum_i \mu_{i,2} \tag{3.29}$$

$$\left\langle \frac{p_z}{E_0}\mathcal{C}[f] \right\rangle \;=\; -\Gamma^{\rm tot}u_2. \tag{3.30}$$

The total interaction rate is connected with a diffusion constant, which reads $D = K_4/(K_1\Gamma^{\rm tot})$ [72]. The source terms (3.25)-(3.27) in the Boltzmann equations (3.23) and (3.24) contain first order perturbations of μ and u. Thus, we need in addition a set of equations to first order, which is solved first. Then the derivatives μ_1' and u_1' of the solutions enter the second order equations (3.23) and (3.24). To first order one finds the following expressions for the Boltzmann equations

$$v_{\rm w}K_1\mu_1' + v_{\rm w}K_2(m^2)'\mu_1 + u_1' - \Gamma^{\rm inel}\sum_i \mu_{i,1} \;=\; v_{\rm w}K_3(m^2)' \tag{3.31}$$

$$-K_4\mu_1' + v_{\rm w}\tilde{K}_5u_1' + v_{\rm w}\tilde{K}_6(m^2)'u_1 + \Gamma^{\rm tot}u_1 \;=\; 0, \tag{3.32}$$

which are similar to the second order ones.
For the contributions to the chemical potential of left-handed quarks we take into account in the transport equations left-handed $SU(2)$ doublet tops $\mu_{t,2}$, left-handed

$SU(2)$ doublet bottoms $\mu_{b,2}$ and left-handed $SU(2)$ singlet tops $\mu_{t^c,2}$ and their corresponding velocity perturbations. We also include the Higgs bosons with $\mu_{h,2}$ and $u_{h,2}$. The chemical potential of left-handed quarks μ_{B_L} can be expressed in terms of the solutions of the transport equations [77]

$$\mu_{B_L} = \frac{1}{2}(1 + 4K_{1,t})\mu_{t,2} + \frac{1}{2}(1 + 4K_{1,b})\mu_{b,2} - 2K_{1,t}\mu_{t^c,2}. \qquad (3.33)$$

Finally, the baryon asymmetry is given by [72]

$$\eta_B = \frac{n_B}{s} = \frac{\Gamma_{ws}}{4\pi^2 v_{\mathrm{w}} g_* T} \int_0^\infty \mathrm{d}z\, \mu_{B_L}(z)\, e^{-\nu z} \qquad (3.34)$$

where Γ_{ws} is the weak sphaleron rate, which is only present in the symmetric phase. The exponent $\nu = 45\Gamma_{ws}/(4v_{\mathrm{w}})$ accounts for the relaxation of the baryon number if the wall moves very slowly. The effective number of degrees of freedom in the hot plasma is $g_* = 106.75$. The computation of the baryon asymmetry was performed in the wall frame, but to first order in v_{w} it is equal to that in the plasma frame.

Chapter 4

The Standard Model with a Dimension-Six Higgs Operator

4.1 The potential at zero temperature

We already saw that in the Standard Model (SM) the requirements for electroweak baryogenesis are not fulfilled. Insisting on electroweak phase transition (EWPT) as a mechanism for generating the baryon asymmetry of the universe one needs to introduce new physics beyond the Standard Model (BSM). Such a new theory could be e.g. an ordinary quantum field theory with an extension in the Higgs sector, as discussed in the following chapter, or a more fundamental theory, containing for instance extra dimensions. Provided that the new physics appears at a cut-off scale Λ we can parameterize its effects with higher dimensioned non-renormalizable operators. We have to require a low cut-off scale $\Lambda \lesssim 1$ TeV in order to get a relevant influence of a higher dimensional operator at EWPT temperatures $T \approx 100$ GeV. In this work we follow the idea of ref. [21] and add a dimension-six operator to the Standard Model tree-level Higgs potential:

$$V_0(\Phi) = -\mu^2 \Phi^\dagger \Phi + \lambda \left(\Phi^\dagger \Phi \right)^2 + \frac{1}{\Lambda^2} \left(\Phi^\dagger \Phi \right)^3 \tag{4.1}$$

where $\Phi = \begin{pmatrix} \phi^+ \\ \phi^0 \end{pmatrix}$ is the SM Higgs doublet. We achieve an effective theory with the SM Higgs where the new physics is summarized at low scales in the φ^6 interaction. If we parameterize the neutral component in the usual way, $\mathrm{Re}(\phi^0) = \frac{1}{\sqrt{2}} \varphi$, we obtain

$$V_0(\varphi) = -\frac{\mu^2}{2} \varphi^2 + \frac{\lambda}{4} \varphi^4 + \frac{1}{8\Lambda^2} \varphi^6. \tag{4.2}$$

The stabilization of the Higgs potential with this φ^6 interaction offers the possibility to obtain a strong first order phase transition also for Higgs masses above the

experimental bound [21–23]. The potential is now bounded below by the additional φ^6 term, not by the φ^4 coupling as in the Standard Model. This allows us to choose also a negative coupling λ. The potential barrier, which separates the broken and symmetric minimum and which triggers the phase transition, can be generated not only by the thermal one-loop corrections due to the gauge bosons but also by a negative λ. For a shorter notation let us denote our model with a dimension-six operator and a low cut-off just by the "φ^6 model".

In the Standard Model, without a φ^6 interaction, the Higgs mass is given by the expression $m_h = -\mu^2 + 3\lambda v^2$, where $v = \langle\varphi\rangle = 246$ GeV is the vacuum expectation value of the Higgs field. If one diagonalizes the mass matrix derived from the potential (4.1) instead of the SM case one obtains for the field dependent squared Higgs mass

$$m_h^2(\varphi) = -\mu^2 + 3\lambda\varphi^2 + \frac{15}{4\Lambda^2}\varphi^4 \tag{4.3}$$

and for the squared mass of the three Goldstone bosons

$$m_G^2(\varphi) = -\mu^2 + \lambda\varphi^2 + \frac{3}{4\Lambda^2}\varphi^4. \tag{4.4}$$

At zero-temperature we further add to the tree-level potential the one-loop correction from the top quark because it contributes due to its rather heavy mass. The one-loop expression reads [42]

$$V_1^{\text{top}}(\varphi) = -12\,\frac{1}{64\pi^2}m_t^4(\varphi)\ln\frac{m_t^2(\varphi)}{Q^2} \tag{4.5}$$

where we choose for the renormalization scale $Q = m_t = 178$ GeV. Inserting the field dependent top mass

$$m_t(\varphi) = \frac{y_t}{\sqrt{2}}\,\varphi \tag{4.6}$$

where y_t is the top Yukawa coupling, we derive for the one-loop potential the expression

$$V(\varphi) = V_0(\varphi) + V_1^{\text{top}}(\varphi) = -\frac{\mu^2}{2}\varphi^2 + \frac{\lambda}{4}\varphi^4 + \frac{1}{8\Lambda^2}\varphi^6 - \frac{3}{64\pi^2}y_t^4\varphi^4\ln\frac{y_t^2\varphi^2}{2Q^2}. \tag{4.7}$$

With the minimum condition

$$\left.\frac{\partial V(\varphi)}{\partial\varphi}\right|_{\varphi=v} = 0 \tag{4.8}$$

and the equation for the squared Higgs mass

$$\left.\frac{\partial^2 V(\varphi)}{\partial\varphi^2}\right|_{\varphi=v} = m_h^2 \tag{4.9}$$

we can express the two couplings μ^2 and λ in terms of the physical parameters v and m_h as well as in dependence of the cut-off scale Λ. Since $v = 246$ GeV is known we are left with the two free input parameters m_h and Λ. The solution of the above conditions (4.8) and (4.9) finally yields

$$
\begin{aligned}
\mu^2 &= \frac{1}{2}m_h^2 - \frac{3}{4\Lambda^2}v^4 + \frac{3y_t^4}{16\pi^2}v^2, \\
\lambda &= \frac{1}{2v^2}m_h^2 - \frac{3}{2\Lambda^2}v^2 + \frac{3y_t^4}{16\pi^2}\left(\frac{3}{2} + \ln\frac{y_t^2 v^2}{2Q^2}\right),
\end{aligned}
\tag{4.10}
$$

which we insert in the one-loop potential (4.7).

4.2 The finite temperature effective potential

At finite temperature we take into account the contributions from the top quark, the W- and Z-bosons, the Higgs and the three Goldstone bosons. We can use the high temperature expansions of the bosonic and fermionic functions (2.27) and (2.28) since the relevant mass over temperature range is small enough so that the expansions can be regarded as valid. For the bosons we take the approximation up to the cubic term

$$
\Delta V_{\mathrm{eff},T}^{B}(\varphi, T) = T^4 \sum_B n_B \left[\frac{-\pi^2}{90} + \frac{(m_B/T)^2}{24} - \frac{(m_B/T)^3}{12\pi}\right]
\tag{4.11}
$$

with the field dependent Higgs masses given in eqs. (4.3) and (4.4). The degrees of freedom are $n_h = 1$, $n_G = 3$, $n_W = 6$ and $n_Z = 3$. In the cubic term of eq. (4.11) we count only the transverse degrees of freedom of the weak gauge bosons, i.e. we introduced a factor 2/3 in this term, which corresponds to the simplest way to implement resummation. The squared masses of the gauge bosons read

$$
\begin{aligned}
m_W^2(\varphi) &= \frac{g_2^2}{4}\varphi^2, \\
m_Z^2(\varphi) &= \frac{g_1^2 + g_2^2}{4}\varphi^2
\end{aligned}
\tag{4.12}
$$

where $g_2 = 0.6516$ and $g_1 = 0.35$ are the $SU(2)_L$ and $U(1)_Y$ gauge couplings. In the fermionic sector we consider the top quark as the heaviest one with its contribution due to the high temperature expansion (2.31),

$$
\Delta V_{\mathrm{eff},T}^{\mathrm{top}}(\varphi, T) = 12\,T^4 \left[\frac{-7\pi^2}{720} + \frac{(m_t/T)^2}{48} + \frac{(m_t/T)^4}{64\pi^2}\ln\frac{(m_t/T)^2}{c_F}\right].
\tag{4.13}
$$

Finally we add to the effective potential the thermal two-loop contribution from the Higgs bosons,

$$\Delta V_{\text{eff,T}}^{2-\text{loop}}(\varphi, T) = \frac{1}{8\Lambda^2}\, T^4 \varphi^2, \tag{4.14}$$

in order to test its influence on the phase transition. Summing up the zero-temperature part (4.7) and the thermal parts (4.11), (4.13) and (4.14) we end up with the effective potential

$$
\begin{aligned}
V_{\text{eff,T}}(\varphi, T) \;\; = \;\; & \frac{1}{2}\left[-\mu^2 + \left(\frac{1}{2}\lambda + \frac{1}{16}g_1^2 + \frac{3}{16}g_2^2 + \frac{1}{4}y_t^2\right)T^2\right]\varphi^2 \\
& -\frac{g_2^3}{16\pi}\, T\varphi^3 + \frac{\lambda}{4}\,\varphi^4 + \frac{3y_t^4}{64\pi^2}\,\varphi^4 \ln\frac{Q^2}{c_\text{F}T^2} \\
& +\frac{1}{8\Lambda^2}\left(\varphi^6 + 2\,T^2\varphi^4 + T^4\varphi^2\right)
\end{aligned}
\tag{4.15}
$$

where we have dropped terms not depending on the field φ, which corresponds only to a shift in the potential, so that it is normalized to $V_{\text{eff,T}}(0, T) = 0$. On the other hand we further simplified the expression by neglecting the gauge coupling g_1 in the cubic term of the expansion $\Delta V_{\text{eff,T}}^{\text{B}}$ since the dominant contribution arises from g_2. The effect on the strength of the PT is less than one percent if we drop g_1.

4.3 The strength of the phase transition

We first analyze the parameter range with regard to the strength ξ of the phase transition. As we will see, the cut-off parameter Λ has to be less than about 850 GeV for a strong first order transition. We require $\Lambda \gtrsim 400$ GeV in order to make an expansion in v/Λ reasonable. The Higgs mass range is bounded from below by the experimental constraint $m_h \gtrsim 115$ GeV. We extend the m_h-interval up to around 200 GeV where we still find $\xi \approx 1$ for small Λ.

The critical temperature T_c, at which the phase transition takes place, and the non-zero expectation value $\langle\varphi\rangle_T = v_c$ of the broken minimum are defined by the two conditions

$$
\begin{aligned}
\left.\frac{\partial V_{\text{eff,T}}(\varphi, T_c)}{\partial\varphi}\right|_{\varphi=v_c} &= 0, \\
V_{\text{eff,T}}(v_c, T_c) &= 0.
\end{aligned}
\tag{4.16}
$$

It is not possible to solve the above equations for v_c and T_c analytically because the temperature appears both in the polynomial and in the log-term of the effective potential (4.15). But the solutions can easily be found for a given parameter set with numerical methods. The strength of the phase transition

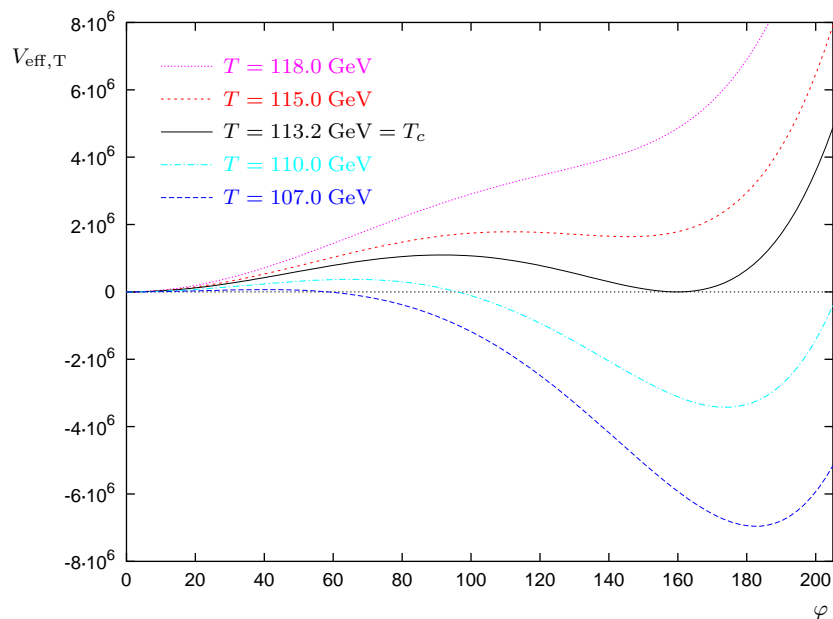$$\xi = \frac{v_c}{T_c} \tag{4.17}$$

Figure 4.1: The shape of the effective potential for several temperatures at $\Lambda = 550$ GeV and $m_h = 150$ GeV. φ is given in units of GeV, $V_{\text{eff,T}}$ in GeV^4.

has to be greater than about one due to the washout criterion, eq. (2.34), so that the sphaleron processes in the broken phase are suppressed and the generated baryon asymmetry is conserved. In order to get an idea of the evolution of the effective potential with temperature we show in fig. 4.1 an example for $\Lambda = 550$ GeV and $m_h = 150$ GeV. Here the broken minimum is located at $v_c \approx 160$ GeV at a critical temperature $T_c \approx 113$ GeV, which results in a strength $\xi \approx 1.4$.

We are also interested in the influence of the different loop contributions on the strength of the phase transition. We altered the effective potential and tested for several parameter sets the change in ξ compared with the result derived from the original potential (4.15). We successively omit in this potential the cubic term $\sim T\varphi^3$, the log term, the one-loop contribution due to the dimension-six Higgs operator $\sim T^2\varphi^4$ and the two-loop contribution $\sim T^4\varphi^2$. When the logarithmic part is neglected one has to take into account that also the tree-level relations (4.10) between the couplings μ and λ in the potential (4.2) and the parameters m_h and Λ change. Moreover we examine the relevance of an additional higher dimensional operator $\sim \varphi^8$. Therefore we add to the effective potential the expression

$$\frac{1}{16M^4}\,\varphi^8. \tag{4.18}$$

The effects of the various contributions are listed in table 4.1, which shows the corresponding values of ξ for six sets of m_h and Λ covering the physically interesting parameter space. The cubic term has a favorable effect on the strength for ξ close to one. Leaving it out weakens the phase transition. It gets less important for increasing ξ, but reaching $\xi \approx 2$ turns around the influence and it now lowers the

m_h/GeV	Λ/GeV	full φ^6 pot.	without				with φ^8
			cubic	log	1-loop	2-loop	
120	800	1.00	0.64	1.15	1.35	0.99	0.99
120	700	1.62	1.55	2.08	1.83	1.61	1.60
120	600	2.44	2.51	3.47	2.39	2.42	2.39
150	600	1.02	0.90	1.13	1.36	1.00	1.01
150	500	1.87	1.90	2.36	1.87	1.84	1.82
180	450	1.23	1.21	1.40	1.41	1.17	1.19

Table 4.1: The influence of different contributions on the strength ξ. The column "full φ^6 potential" represents ξ evaluated with the potential (4.15). See the text for a detailed explanation of the further columns.

strength marginally. In general we agree with the results of Grojean et al. [23], who also found that the cubic interaction tends to make the transition somewhat stronger in the relevant parameter region. In ref. [23] the logarithmic part was neglected, too. But here we discovered an enhancement of $\mathcal{O}(10\%)$ in the strength if one neglects the log term. Thus, one should take it into account in the computations. The importance of the one-loop contribution arising from the φ^6 operator is similar to that of the cubic one. The influence is largest for small ξ, but in contrast to the φ^3 coupling it decreases the strength of the phase transition. It also becomes less relevant for larger ξ. The different one-loop contributions partially cancel each other and therefore we agree quite well with the results of ref. [23], although they located the boundary $\xi = 1$ at slightly larger values of Λ. The two-loop term as well as the additional φ^8 coupling affect ξ only at the order of about one percent. Consequently, a dimension eight operator can be safely neglected in our further calculations.

Let us analyze the dependence of the strength of the EWPT on the model parameters m_h and Λ. Therefore we varied the scale Λ from 400 up to 850 GeV in steps of 25 or 50 GeV. For each given Λ the effective potential was evaluated for Higgs masses in steps of 0.5 GeV starting from $m_h = 115$ GeV and ending when $\xi \lesssim 1$. For the observables under consideration we performed smooth interpolations of the evaluated points, e.g. in order to determine the boundary $\xi = 1$ in dependence of m_h and Λ. As expected the phase transition becomes stronger for decreasing Higgs masses. We demonstrate the behavior considering as example the case of fixed $\Lambda = 500$ GeV, shown in fig. 4.2a. The slope of the curve gets steeper for small masses and ξ raises rapidly. One obtains a very similar shape for the function $\xi(\Lambda)$ at constant m_h. Part (b) illustrates the Λ-dependence at $m_h = 120$ GeV. Both curves end at a minimal m_h or Λ, respectively. Below these endpoints the non-trivial, i.e. the symmetry breaking minimum, is not the global one even for zero-temperature. Then a tunneling from the symmetric into the broken local minimum will never start and the universe will get stuck in the false vacuum at $\varphi = 0$. In the limit of two
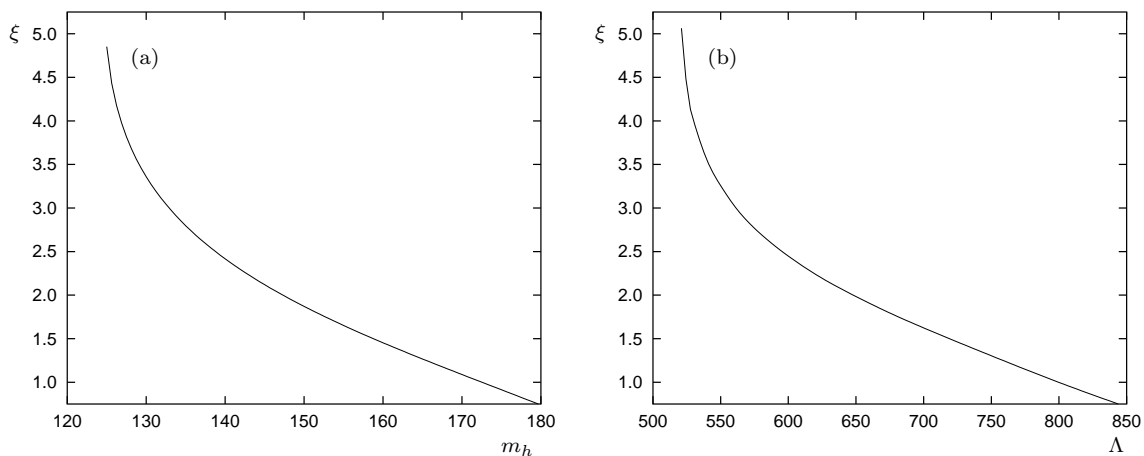
Figure 4.2: The dependence of ξ on the Higgs mass m_h at fixed $\Lambda = 500$ GeV (a) and on the scale Λ at fixed $m_h = 120$ GeV (b). m_h and Λ are given in units of GeV in the plots.

degenerate minima at $T = 0$ the potential satisfies the equation

$$
\begin{aligned}
V(\varphi = v) &= 0 \\
\Leftrightarrow \quad -\frac{1}{8}m_h^2 v^2 + \frac{v^6}{8\Lambda^2} - \frac{3y_t^4 v^4}{128\pi^2} &= 0
\end{aligned}
\tag{4.19}
$$

where we inserted in the second line the expressions (4.10) for μ^2 and λ. Solving it for Λ yields

$$
\Lambda = \frac{4\pi v^2}{\sqrt{16\pi^2 m_h^2 + 3y_t^4 v^2}},
\tag{4.20}
$$

which sets a lower bound on the scale Λ for a given Higgs mass. We analyze the whole parameter space with regard to the strength of the phase transition, taking into account the bound given by eq. (4.20) and the requirement $\xi \geq 1$. The results are presented in fig. 4.3 where lines of constant ξ together with the above function (4.20), labeled with "wrong global minimum", are shown. Starting from the region with a strong first order phase transition, i.e. $\xi \gtrsim 1$, one first reaches the "metastability" regime at $\xi \approx 3$ before approaching the line of the wrong global minimum. The metastability line indicates the case when the probability of thermal tunneling from the symmetric into the broken minimum becomes too small, so that the universe already remains in the false vacuum. The requirements for thermal tunneling are discussed in more detail together with the bubble properties in the following section 4.4. As can be seen from fig. 4.3 one finds a large part of the parameter space which fulfills the requirement of a strong EWPT. For small Higgs masses we can extend the Λ-range from ≈ 600 up to ≈ 800 GeV. At $m_h = 165$ GeV we reach for large ξ the lower bound of $\Lambda = 400$ GeV, which we set, and still find for Higgs masses up to about 200 GeV the possibility of a strong first order phase transition. A favorable effect is provided by the opportunity that the coupling λ can be negative since the
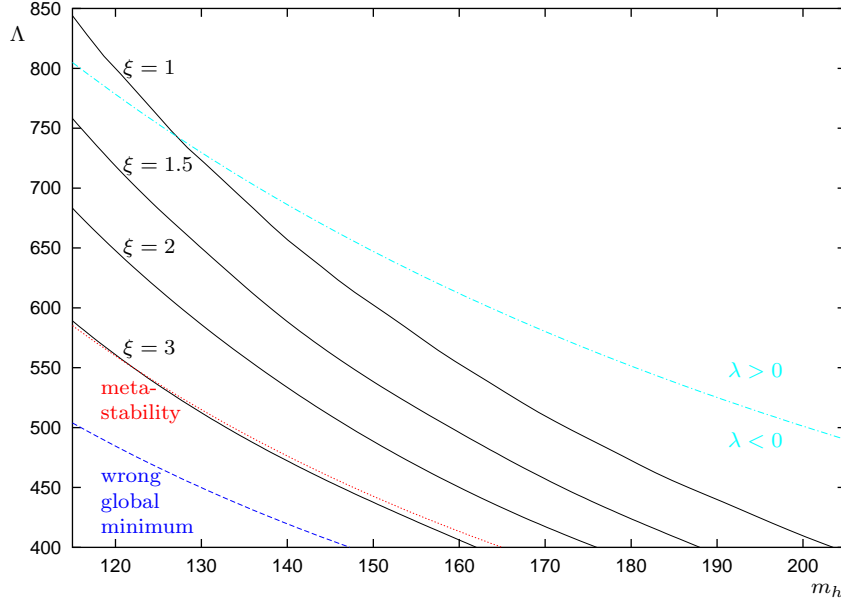
Figure 4.3: Lines of constant ξ in the Λ-m_h-plane. Below the dashed blue line the non-trivial minimum is not the global one, below the dotted red line the tunneling probability is too small and the dashed-dotted turquoise line divides the regions of $\lambda > 0$ and $\lambda < 0$. Λ and m_h are given in units of GeV.

potential is stabilized by the φ^6 operator. The turquoise line in the figure indicates the case $\lambda = 0$, which corresponds to the relation

$$\Lambda = \frac{4\sqrt{3}\pi v^2}{\sqrt{16\pi^2 m_h^2 + 3y_t^4 v^2 \left(3 + 2\ln\frac{y_t^2 v^2}{2Q^2}\right)}} \tag{4.21}$$

derived from eq. (4.10). Note that almost in the whole parameter region with $\xi > 1$ the coupling λ is actually negative.

4.4 Bubble properties

In this section we will have a closer look on the nucleating bubbles and their properties. Especially the thickness of the bubble wall enters the computation of the baryon asymmetry. As stated already in section 2.4, the bubbles of the non-zero Higgs expectation value start to nucleate at a temperature T_n slightly below the critical temperature T_c. The determination of this temperature T_n is not trivial and we can only give an estimate. In order to determine T_n we first approximate
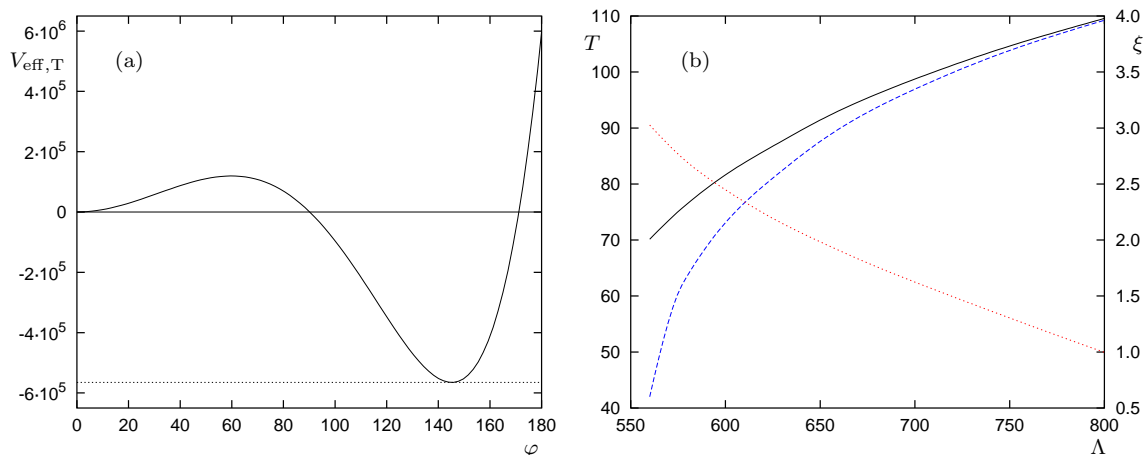
Figure 4.4: (a) The effective potential at $T = T_n \approx 103.8$ GeV for $m_h = 120$ GeV
and $\Lambda = 750$ GeV. The dotted line shows $-\Delta V \approx -5.65 \cdot 10^5$ GeV^4.
(b) The critical temperature T_c (black line) and the nucleation tempera-
ture T_n (dashed blue line) versus Λ for constant $m_h = 120$ GeV (left
scale) and the corresponding ξ (dotted red line, right scale).
$V_{\mathrm{eff,T}}$ is given in units of GeV^4, φ, T and Λ in GeV.

the three-dimensional Euclidean action according to the condition (2.41) for the
tunneling probability by

$$S_3 \approx 130\, T_c \tag{4.22}$$

where we used the fact that $T_n \approx T_c$. We follow the thin wall approximation where
the surface tension (2.45) is given by the integral

$$S_1 = \int_0^{v_c} \mathrm{d}\varphi \sqrt{2 V_{\mathrm{eff,T}}(\varphi, T_c)}. \tag{4.23}$$

Using the result (2.47), $S_3 = 16\pi S_1^3/\Delta V^2$, and inserting the above equations (4.22)
and (4.23) yields for the energy difference $\Delta V = V_{\mathrm{eff,T}}(\varphi_{\mathrm{sym}}, T) - V_{\mathrm{eff,T}}(\varphi_{\mathrm{brk}}, T)$

$$\Delta V = \sqrt{\frac{16\pi S_1^3}{3 S_3}}. \tag{4.24}$$

Since the symmetric minimum at the origin is normalized to $V_{\mathrm{eff,T}}(0, T) = 0$, one
has to tune the temperature such that

$$V_{\mathrm{eff,T}}(\varphi = \varphi_{\mathrm{brk}}, T = T_n) = -\Delta V \tag{4.25}$$

where φ_{brk} shall be understood as the non-trivial minimum at the nucleation tem-
perature T_n. Close to $\xi = 1$ the potential varies rapidly with the temperature and
the amount ΔV of supercooling is soon reached. Thus, T_n is in fact close to T_c.
We demonstrate the evolution of the effective potential in fig. 4.4a considering as

an example the parameter set $m_h = 120$ GeV and $\Lambda = 750$ GeV. For this case we find $T_n \approx 103.8$ GeV, which is barely 1% lower than the critical temperature $T_c \approx 104.6$ GeV. The validity of our approximation scheme should be regarded as valid as long as T_n differs not considerably from T_c, say roughly 10%. The deviation increases with rising strength ξ. The dependence of both T_c and T_n on the scale Λ is illustrated in fig. 4.4b for the example under consideration with $m_h = 120$ GeV. In addition the corresponding ξ is also plotted. For large Λ, or small ξ, the gap between T_c and T_n is of order 1%. At $\Lambda \approx 600$ GeV it approaches 10% when ξ is about 2.5. Then our approximation breaks down. Therefore we should limit the parameter space with regard to the computation of the baryon asymmetry to the region where $1 \lesssim \xi \lesssim 2.5$.

CP-violation

The higher-dimensional operator in our model under consideration provides new sources of CP-violation, which is necessary for the generation of the baryon asymmetry. The CP-violation results in a complex fermion mass. The couplings of such non-standard operators to the top quark were discussed in ref. [82] where an operator of the form

$$\overline{\Psi}_L \frac{x}{\Lambda^2}(\Phi^\dagger \Phi)\Phi \Psi_R \tag{4.26}$$

was taken into account. In the following we ignore flavor mixing in the quark sector and also focus only on the top quark, whose mass arises from the Lagrangian

$$\mathscr{L}_\mathrm{m} = \overline{T}_L\left(y_\mathrm{t} + \frac{x_\mathrm{t}}{\Lambda^2}\Phi^\dagger \Phi\right)\widetilde{\Phi}\, t_R + \mathrm{h.c.} \tag{4.27}$$

where $\overline{T}_L = (\bar{t}_L, \bar{b}_L)$ and $\widetilde{\Phi} = i\sigma_2\Phi^* = \left(\begin{smallmatrix} \phi^{0*} \\ -\phi^- \end{smallmatrix}\right)$. y_t is the SM Yukawa coupling and x_t is a new coupling, which can in general contain a complex phase. There are similar terms for the other fermions. For the top quark x_t may be of order unity like y_t, but for the lighter fermions the corresponding couplings should respect the hierarchy of the SM ones and should be therefore much smaller. Inserting the Higgs vacuum expectation value v in the Lagrangian (4.27) leads to the mass term for the top quark,

$$M = \left(y_\mathrm{t} + \frac{x_\mathrm{t}}{2}\frac{v^2}{\Lambda^2}\right)\frac{v}{\sqrt{2}} = y_\mathrm{eff}\frac{v}{\sqrt{2}} \tag{4.28}$$

with y_eff defined as an effective Yukawa coupling. If we assume a complex parameter $x_\mathrm{t} = |x_\mathrm{t}|e^{i\varphi_\mathrm{t}}$ then we derive for the absolute value of the complex top mass $M = me^{i\theta}$ the expression

$$m = |M| = \frac{v}{\sqrt{2}}\sqrt{y_\mathrm{t}^2 + \frac{|x_\mathrm{t}|^2}{4}\frac{v^4}{\Lambda^4} + y_\mathrm{t}|x_\mathrm{t}|\cos\varphi_\mathrm{t}\frac{v^2}{\Lambda^2}} \tag{4.29}$$

and for the phase

$$\tan \theta = \frac{|x_{\rm t}|/2 \, \sin \varphi_{\rm t} \, v^2/\Lambda^2}{y_{\rm t} + |x_{\rm t}|/2 \, \cos \varphi_{\rm t} \, v^2/\Lambda^2}. \tag{4.30}$$

The corrections to $y_{\rm t}$ which are proportional to $\cos \varphi_{\rm t}$ are suppressed by $\mathcal{O}(v^2/\Lambda^2)$ and we therefore can ignore a real part of $x_{\rm t}$, i.e. setting $\varphi_{\rm t} = \pi/2$, which corresponds to maximal CP-violation. Neglecting the even more suppressed contribution $\sim v^4/\Lambda^4$ we find for the top mass and its phase

$$\begin{aligned} m &= y_{\rm t}\frac{v}{\sqrt{2}}, \\ \tan \theta &= \frac{|x_{\rm t}|v^2}{2y_{\rm t}\Lambda^2}. \end{aligned} \tag{4.31}$$

Since the SM Yukawa coupling is of order one we also choose for $x_{\rm t}$ in the following the fixed value $|x_{\rm t}| = 1$. During the phase transition when the particles pass through the bubble wall their masses become space-time dependent, as is discussed in the next section.

The wall profile

The Higgs expectation value changes along the bubble wall from the symmetric to the broken minimum. If the nucleating bubbles have reached a sizable extent and expand with constant velocity then we can boost into the rest frame of the bubble wall and assume a planar wall, translationally invariant in the x- and y-directions. The Higgs field and thereby the top mass depend only on the z-coordinate. Then the modulus and phase of the top mass become according to eqs. (4.31)

$$\begin{aligned} m(z) &= y_{\rm t}\frac{\varphi(z)}{\sqrt{2}}, \\ \theta(z) &= \arctan \frac{\varphi^2(z)}{2y_{\rm t}\Lambda^2}. \end{aligned} \tag{4.32}$$

The value of $\varphi(z)$ changes from zero in the symmetric phase ($z > 0$) to v_c in the broken one ($z < 0$). But we are left with the problem of how to determine the bubble wall profile, which separates the two phases. In section 2.4 we already discussed the example of a simple φ^4 theory where the bubble wall is described by a tanh-curve and the wall thickness is determined with the height V_b of the potential barrier,

$$\begin{aligned} \varphi(z) &= \frac{v_c}{2}\left(1 - \tanh \frac{z}{L_{\rm w}}\right), \tag{4.33} \\ L_{\rm w} &= \frac{v_c}{\sqrt{8V_b}}. \tag{4.34} \end{aligned}$$

We will use these equations for an approximation of $L_{\rm w}$ and the wall profile, but also discuss and compare further methods in the following.

A second and direct way to derive the profile is to solve the field equation numerically. Here we also use the thin wall approximation where the field equation reads (see section 2.4)

$$\frac{\mathrm{d}^2\varphi(z)}{\mathrm{d}z^2} = \frac{\mathrm{d}V_{\mathrm{eff,T}}(\varphi(z), T_c)}{\mathrm{d}\varphi(z)} \tag{4.35}$$

with boundary conditions $\varphi(z \to -\infty) \to v_c$ and $\varphi(z \to \infty) \to 0$. For practical reasons one has of course to restrict to a finite interval in which the equation is solved. We do not treat the equation as a boundary value problem, but initialize at one z-position $z = z_1 < 0$ the values of φ and its derivative, which is nearly zero but slightly negative in the broken phase. Thus we start with the two initial conditions

$$\varphi(z_1) = v_c \qquad \text{and} \qquad \left.\frac{\mathrm{d}\varphi(z)}{\mathrm{d}z}\right|_{z=z_1} = -1\cdot10^{-7} \tag{4.36}$$

and solve the differential equation in an interval $[z_1 : z_2]$. We tested several values around $-1\cdot10^{-7}$ for the initial slope and found no significant difference in the resulting wall profile. The lower bound z_1 is adjusted so that $\varphi(z = 0) = v/2$ according to the tanh-curve (4.33), which also falls off to $v/2$ at $z = 0$.

We will discuss the calculations for several examples, which give large, median and small wall thicknesses. Let us first discuss the parameter set $\Lambda = 700$ GeV and $m_h = 120$ GeV in detail. Using eq. (4.34) as an approximation leads to a wall thickness $L_{\mathrm{w}}^{(1)} = 6.7/T_c$ where the index (1) labels the first of three ways of computation. The numerical solution of the differential equation (4.35) is rather similar to a tanh-curve,
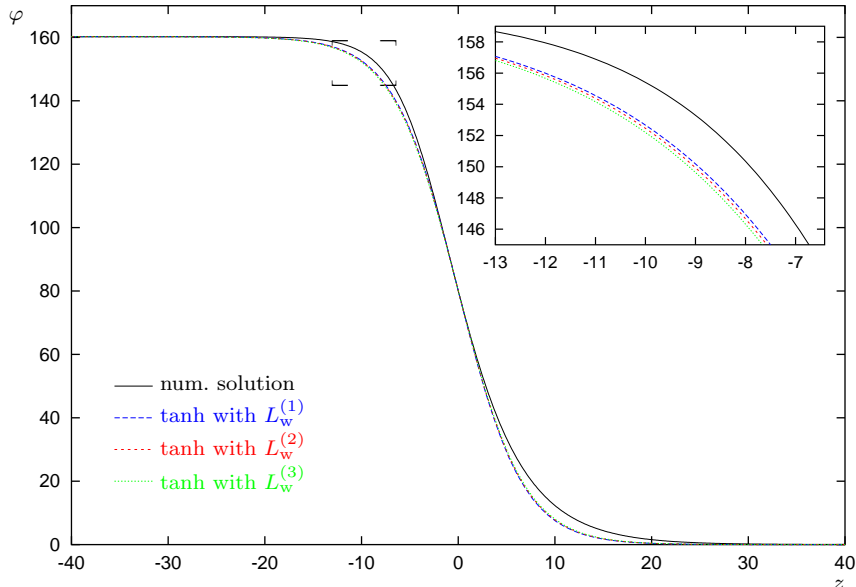

Figure 4.5: The wall profile for the parameter set $\Lambda = 700$ GeV and $m_h = 120$ GeV, derived with different methods (see the text for details). The inset is a magnification of the marked rectangle. φ is given in GeV, z in T_c^{-1}.

as can be seen in fig. 4.5. The black line is the numerical solution and the blue one corresponds to eq. (4.33) with $L_{\mathrm{w}} = L_{\mathrm{w}}^{(1)}$, i.e. using the height of the potential barrier for an approximation. The curves match quite well at the left and right boundaries as well as in the central region around $z = 0$. In-between the numerically calculated one is a bit higher than the tanh-function. In order to determine a wall thickness also for the numerical solution we fit the data to the equation (4.33) with L_{w} as the fit parameter. We denote this fit result with $L_{\mathrm{w}}^{(2)}$ and find for the considered example $L_{\mathrm{w}}^{(2)} = 6.7/T_c$, which is in excellent agreement with $L_{\mathrm{w}}^{(1)}$. This method takes into account the whole curve. A third approach consists of using only the derivative at $z = 0$, which may also define the wall thickness. Again we start from the tanh-function (4.33) and differentiate it,

$$\frac{\mathrm{d}}{\mathrm{d}z}\varphi(z) = -\frac{v_c}{2}\frac{1}{L_{\mathrm{w}}}\operatorname{sech}\frac{z}{L_{\mathrm{w}}},\tag{4.37}$$

so that L_{w} can be found by

$$L_{\mathrm{w}}^{(3)} = -\frac{\varphi(0)}{\varphi'(0)}\tag{4.38}$$

where the prime denotes the derivative with respect to z, which is also calculated numerically. This method results in $L_{\mathrm{w}}^{(3)} = 6.8/T_c$, which is very close to the first two values. In fig. 4.5 also the two tanh-functions with $L_{\mathrm{w}}^{(2)}$ and $L_{\mathrm{w}}^{(3)}$ are shown. For a better comparison of the four plotted curves we zoomed the region around $z = -10$ where the deviations are maximal. Since the approximations with the kink
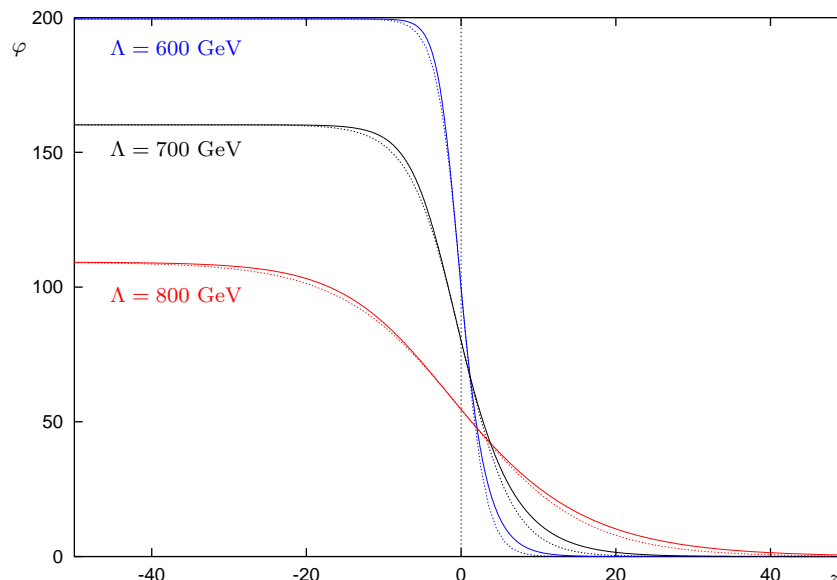

Figure 4.6: The wall profile for $m_h = 120$ GeV and $\Lambda = 600$, 700 and 800 GeV. The solid lines show the numerical solution, the dotted lines the used tanh-ansatz with $L_{\mathrm{w}}^{(1)}$. φ is given in GeV, z in T_c^{-1}.

m_h/GeV	Λ/GeV	T_c/GeV	$L_{\mathrm{w}}^{(1)} \cdot T_c$	$L_{\mathrm{w}}^{(2)} \cdot T_c$	$L_{\mathrm{w}}^{(3)} \cdot T_c$
120	800	109.6	15.7	15.7	15.9
120	700	98.7	6.7	6.7	6.8
120	600	81.6	3.1	3.3	3.2
150	600	122.7	11.2	11.2	11.4
150	500	100.7	3.6	3.7	3.7
180	450	127.0	6.0	6.2	6.1

Table 4.2: Comparison of the wall thickness L_{w} derived with different methods for six parameter sets. See the text for detailed information.

(4.33) differ near $z = \pm 10$ in this example only slightly from the numerically derived solution and the three ways of determining the wall thickness agree quite well, we will use eq. (4.33) together with (4.34), i.e. $L_{\mathrm{w}}^{(1)}$, to describe the wall profile and its thickness and drop the index (1) in the following. This approach allows for a simple computation of L_{w} without the necessity to solve a differential equation and to search for an appropriate interval $[z_1 : z_2]$ for each parameter set in the m_h-Λ-plane. Moreover we have an analytic expression at hand, which enters via eqs. (4.32) the computation of the baryon asymmetry. The example discussed is also a typical representative for the whole parameter range which we analyzed. The wall has always the kink profile shown above. We present the results of our approximation together with the numerical solution in fig. 4.6 for three parameter sets. Beside the example discussed above with a median wall thickness we show two further ones with a large and small L_{w}. In table 4.2 the different wall thicknesses for a total of six m_h-Λ-combinations are listed, which cover the interesting parameter region.
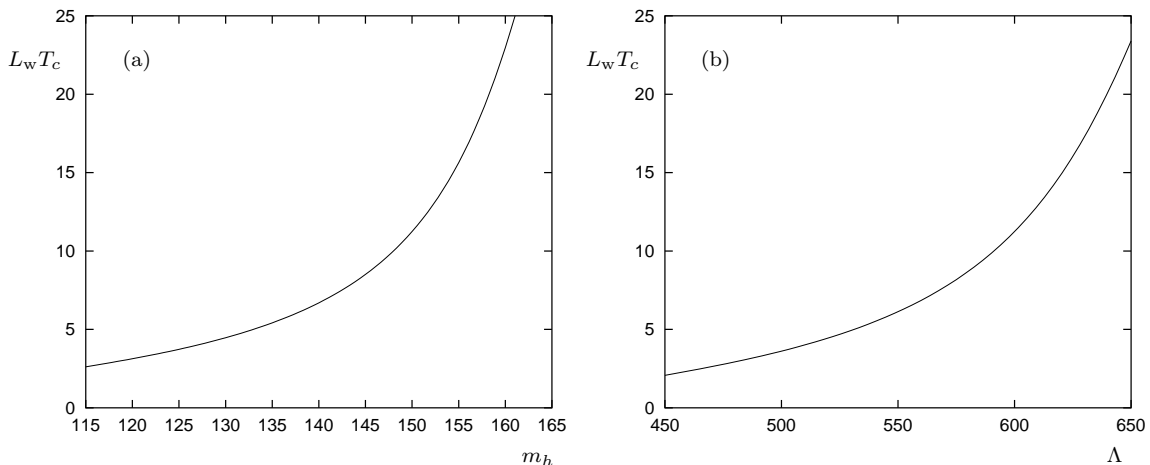

Figure 4.7: The wall thickness in dependence of m_h for constant $\Lambda = 600$ GeV (a) and in dependence of Λ for constant $m_h = 150$ GeV (b).
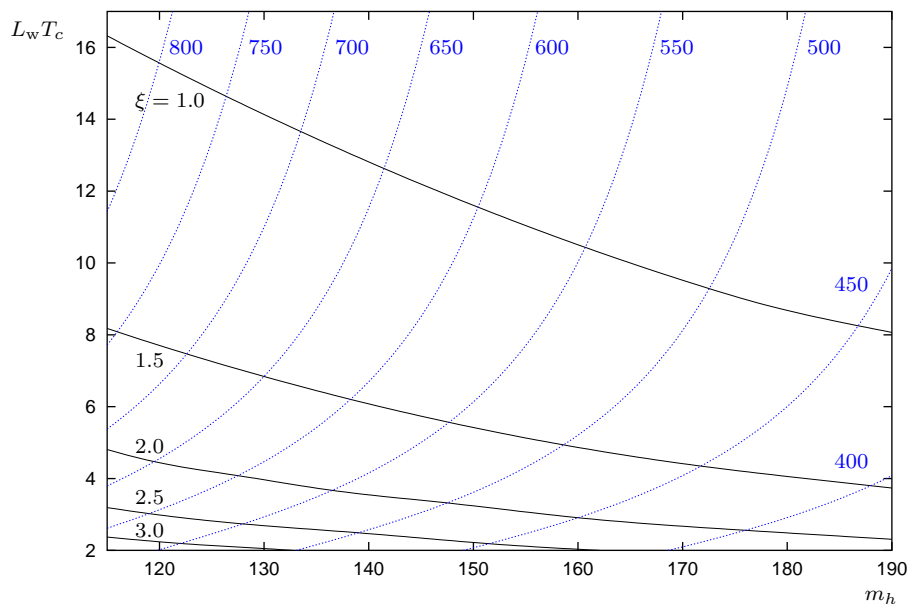
Figure 4.8: Lines of constant ξ (solid black) and Λ (dotted blue) in the L_{w}-m_h-plane. Λ and m_h are given in units of GeV.

The three methods are always consistent with each other.

The dependence of the so computed wall thickness on the Higgs mass and the scale Λ is shown in fig. 4.7. In part (a) we fixed $\Lambda = 600$ GeV and in part (b) $m_h = 150$ GeV. The behavior of L_{w} as a function of m_h and Λ is quite similar. It rises approximately exponentially with increasing m_h and Λ. We find that L_{w} times the critical temperature varies form about two to 25 in the parameter region analyzed. However, the strength of the PT drops below one for large values of L_{w}. Thus, if we restrict ourselves to the case of a strong first order PT, one obtains $2 \lesssim L_{\mathrm{w}} \cdot T_c \lesssim 16$. The connection of L_{w} with ξ is illustrated in fig. 4.8. Here, lines of constant ξ and Λ are plotted in the L_{w}-m_h-plane. The upper limit of $L_{\mathrm{w}} \approx 16/T_c$ can be reached for $m_h \lesssim 120$ GeV and $\Lambda \gtrsim 800$ GeV. Moving along the $\xi = 1$ contour the wall thickness decreases to about $8/T_c$ for $m_h = 190$ GeV. In conclusion, a large part of the parameter space meets the requirements for electroweak baryogenesis. Both the phase transition is strong enough and the wall thickness can be computed well in the thin wall approximation.

The wall velocity

Let us close the discussion of the bubble properties with a short analysis of the wall velocity. We compute v_{w} according to eq. (2.51), stated already in section 2.4. Since we do not know the actual size of the $\mathcal{O}(1)$-correction in this formula, we tested two

		$\xi = 1.0$	$\xi = 1.1$	$\xi = 1.2$	$\xi = 1.3$	$\xi = 1.4$	$\xi = 1.5$	$\xi = 1.6$
$m_h =$ 120 GeV	$v_{\mathrm{w}}^{(0)}$	0.23	0.34	0.49	0.70	0.98	1.30	1.78
	$v_{\mathrm{w}}^{(1)}$	0.14	0.21	0.29	0.41	0.57	0.75	1.00
	ln	1.62	1.57	1.51	1.44	1.38	1.33	1.27
$m_h =$ 150 GeV	$v_{\mathrm{w}}^{(0)}$	0.32	0.49	0.74	1.07	1.52	2.12	-
	$v_{\mathrm{w}}^{(1)}$	0.18	0.27	0.40	0.56	0.78	1.05	-
	ln	1.32	1.25	1.18	1.11	1.04	0.98	-
$m_h =$ 180 GeV	$v_{\mathrm{w}}^{(0)}$	0.47	0.75	1.13	1.69	2.46	-	-
	$v_{\mathrm{w}}^{(1)}$	0.24	0.37	0.53	0.75	1.05	-	-
	ln	1.04	0.96	0.88	0.81	0.75	-	-

Table 4.3: The two wall velocities $v_{\mathrm{w}}^{(0)}$ and $v_{\mathrm{w}}^{(1)}$ according to eqs. (4.39) and (4.40) for different Higgs masses and strengths ξ. The rows labeled with "ln" represent the contribution of the logarithmic term $\ln(m_W L_{\mathrm{w}})$ to the denominator. Results for $v_{\mathrm{w}}^{(1)} \gg 1$ are omitted.

different versions, where we set the $\mathcal{O}(1)$-correction to zero and one, respectively,

$$v_{\mathrm{w}}^{(0)} \;=\; \frac{32\pi L_{\mathrm{w}}}{11 g_2^2 T^3} \frac{\Delta V}{\ln(m_W L_{\mathrm{w}})}, \tag{4.39}$$

$$v_{\mathrm{w}}^{(1)} \;=\; \frac{32\pi L_{\mathrm{w}}}{11 g_2^2 T^3} \frac{\Delta V}{\ln(m_W L_{\mathrm{w}}) + 1}. \tag{4.40}$$

In table 4.3 we present the results for three different Higgs masses, covering our relevant parameter space. Moving to stronger phase transitions the wall velocity reaches unphysical values greater than one. The limit $v_{\mathrm{w}} \approx 1$ is exceeded with the underlying approximations at $\xi \approx 1.4 - 1.6$ for $m_h = 120$ GeV and at $\xi \approx 1.2 - 1.4$ for $m_h = 180$ GeV. We omit results $v_{\mathrm{w}}^{(1)} \gg 1$ with no physical significance in table 4.3. Unfortunately the size of the term $\ln(m_W L_{\mathrm{w}})$ in the denominator is of order one and therefore the additional order unity correction is not negligible. This reduces the wall velocity by a factor of about two. Moreover v_{w} is reduced further by latent heat of the nucleating bubbles. The estimates for v_{w} contain large uncertainties and may only give an upper limit of the actual velocity. In general the wall moves faster for stronger phase transitions and larger Higgs masses. Due to these uncertainties we treat in the following the wall velocity as a free parameter in the computation of the baryon asymmetry in both models which we analyze.

4.5 Electric dipole moments

In general, this model with a low cut-off is expected to lead to non-standard physics at high energies due to higher dimensional operators, which e.g. affect $K-\bar{K}$ mixing. Therefore, effects like flavor changing neutral currents or electric dipole moments (EDMs) arise. We should not be in conflict with experimental electroweak data, as long as restricting to $\Lambda \gtrsim 500$ GeV [76]. We will have a closer look at the influence on the EDMs in the φ^6 model and derive some estimates, which can be compared with the experimental upper bounds.

As a theoretical constraint both P and T have to be violated to obtain a non-zero EDM [83–87]. The electric dipole moment $\mathbf{d}$ of a classical charge distribution $\rho(\mathbf{x})$ is given by

$$\mathbf{d} = \int \mathrm{d}^3 x \, \mathbf{x} \, \rho(\mathbf{x}). \tag{4.41}$$

For elementary particles the orientation of $\mathbf{d}$ has to be coupled to the spin $\mathbf{S}$ since there is no other defining vector. The interaction Hamiltonian of the spin $\mathbf{S}$ and an electric field $\mathbf{E}$ reads

$$\mathscr{H}_E = -d_E \, \mathbf{S} \cdot \mathbf{E} \tag{4.42}$$

where d_E is the electric dipole moment strength. Under a parity transformation the vector $\mathbf{E}$ changes its sign while $\mathbf{S}$ does not, and under time reversal $\mathbf{S}$ changes its sign whereas $\mathbf{E}$ remains the same. Thus, we have for the product $\mathbf{S} \cdot \mathbf{E}$:

$$P(\mathbf{S} \cdot \mathbf{E}) = -\mathbf{S} \cdot \mathbf{E} \qquad \text{and} \qquad T(\mathbf{S} \cdot \mathbf{E}) = -\mathbf{S} \cdot \mathbf{E} \tag{4.43}$$

which means that both P and T are violated if d_E is not equal zero. Because CPT is regarded to be a good symmetry T-violation means also CP-violation. We know since the experiments of Wu in 1957 [88] and those of Cronin and Fitch in 1964 [89] that both P and CP are violated in nature, so that there is the possibility of non-zero EDMs of elementary particles. Already some years earlier, in 1950, the experimental search for EDMs started with the work of Purcell and Ramsey [83] who computed on the basis of existing experimental data an upper bound for the neutron EDM. They derived $|d_n| < 3 \cdot 10^{-18} \, e\,\mathrm{cm}$. The latest experimental limits for the neutron [90] and electron [91] EDMs, which are the quantities measured with the highest sensitivity, are at 90% confidence level

$$|d_n| \leq 3.0 \cdot 10^{-26} \, e\,\mathrm{cm}, \tag{4.44}$$

$$|d_e| \leq 1.6 \cdot 10^{-27} \, e\,\mathrm{cm}. \tag{4.45}$$

In the Standard Model the only source of CP-violation originates from the Cabibbo-Kobayashi-Maskawa matrix in the quark sector [58]. It has been shown that contributions to the EDMs arise first at the three-loop level [92, 93], which results in a natural suppression by several orders of magnitude. Theories beyond the Standard

Model allow in principle much higher values of EDMs. Since in the φ^6 model as well in the two Higgs doublet model new sources of CP-violation arise we have to take care not to exceed the experimental constraints for the EDMs. We will have a closer look at the EDMs in the 2HDM in section 5.8 and discuss the ones in the φ^6 model in the following.

An overview of the different contributions to the EDMs of fermions can be found in ref. [94]. The dominant contribution to the electron electric dipole moment arises from two-loop diagrams discussed by Barr and Zee [95]. We will not go into detail of this computation and follow the results of Zhang et al. [82] who applied the two-loop calculations of ref. [95] to a model with a non-standard top quark Yukawa coupling as it occurs in the model with a dimension-six Higgs operator. They derived from the top-loop with an $H\gamma\gamma$-vertex the approximation [82]

$$
\begin{aligned}
d_{\mathrm{e}}/e &\approx \frac{m_e}{v}\frac{1}{27}\frac{|x_{\mathrm{t}}|\sin\varphi_{\mathrm{t}}}{2y_{\mathrm{t}}}\frac{\alpha_{em}}{\pi v}\frac{1}{16\pi^2}\ln\frac{m_{\mathrm{t}}^2}{m_h^2}\left(\frac{\mathrm{TeV}}{\Lambda}\right)^2 \\
&\approx 4.5\cdot 10^{-29}\,\mathrm{cm}\cdot\ln\frac{m_{\mathrm{t}}^2}{m_h^2}\left(\frac{\mathrm{TeV}}{\Lambda}\right)^2
\end{aligned}
\tag{4.46}
$$

where we again have assumed maximal CP-violation, i.e. $\sin\varphi_{\mathrm{t}}=1$, and $|x_{\mathrm{t}}|=1$. The value of d_{e} is largest for a small Higgs mass and a small cut-off parameter Λ. We find e.g. $d_{\mathrm{e}}\approx 0.25\cdot 10^{-27}\,e\,\mathrm{cm}$ for $m_h=115\,\mathrm{GeV}$ and $\Lambda=400\,\mathrm{GeV}$, which is still one order of magnitude below the experimental limit. d_{e} decreases with increasing
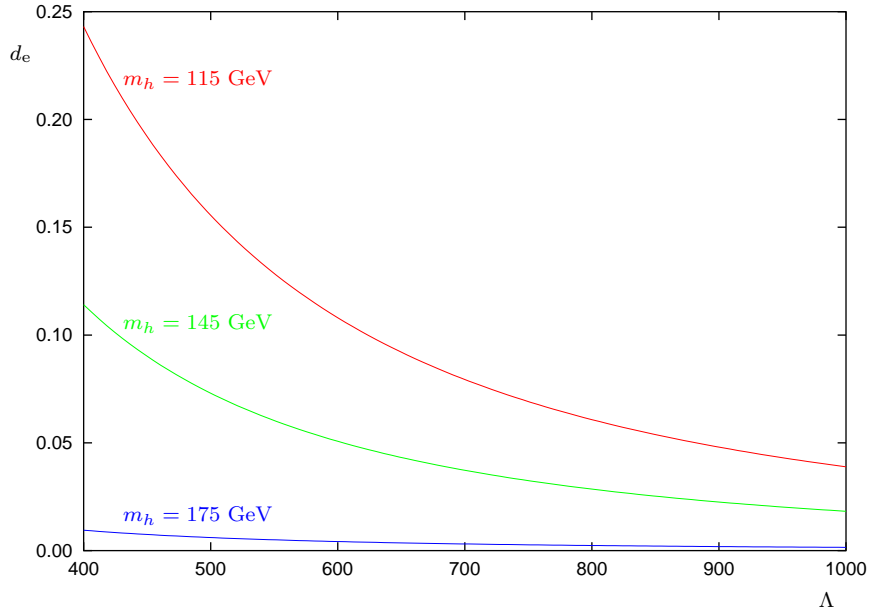

Figure 4.9: The electron EDM in units of $10^{-27}\,e\,\mathrm{cm}$ in dependence of Λ (given in GeV) for three different Higgs masses.

m_h and is also suppressed with Λ^2. Its dependence of Λ^2 and m_h is shown in figure 4.9. In the whole parameter region which fulfills the requirements of baryogenesis the electron EDM is not in conflict with the experimental bound. An improvement of the measurements by one or two orders of magnitude opens the possibility of detecting d_{e} in the near future.

In contrast to the electron EDM the neutron electric dipole moment d_{n} contains large theoretical uncertainties. One has to deal with hadronic effects, which make the relation to the partonic EDMs difficult. Several proposals have been made in the literature, see e.g. ref. [96] for a recent overview. The neutron EDM receives contributions from the up- and down-quark EDMs as well as from the color EDMs. In this work we will also not go into a detailed calculation of d_{n}, but follow again ref. [82] and approximate it by the relation

$$d_{\mathrm{n}} \approx \frac{4}{3}d_d - \frac{1}{3}d_u \approx \frac{m_d}{m_e}d_{\mathrm{e}} \approx (8-16)d_{\mathrm{e}}. \qquad (4.47)$$

This leads to $d_{\mathrm{n}} \approx (0.2 - 0.4)\cdot 10^{-26}\,e\,\mathrm{cm}$ for the example $m_h = 115$ GeV and $\Lambda = 400$ GeV. Since the experimental upper bound of the neutron EDM is about a factor 20 larger than the one of the electron EDM, we also do not exceed the limit anywhere in our parameter range.

4.6 The baryon asymmetry in the φ^6 model

Up to now we have shown that the phase structure of the φ^6 model offers the necessary ingredients for electroweak baryogenesis. In the following we will discuss the resulting baryon asymmetry for several parameter combinations in the m_h-Λ-plane and ask if the experimental value of $\eta_B = 8.7\cdot 10^{-11}$ can be achieved in this model. A detailed analysis was performed by Fromme in ref. [79]. In that work the influence of the different source term contributions and the shape of the single chemical potentials of the involved particles are also studied. Here we will not go into further details and only present the results of ref. [79]. The set of Boltzmann equations (3.23) and (3.24), introduced in section 3.4, can only be solved numerically. It is treated as a boundary value problem. The chemical potentials are fixed to zero at the boundaries of the domain, in which the equations are solved. It turned out that the source terms S_μ and S_u, eqs. (3.25) and (3.27), which depend on the first order perturbations, can be neglected for the computation of the baryon asymmetry. Thus, we are left with the source S_θ, eq. (3.26), and we do not need to solve the first order Boltzmann equations (3.31) and (3.32). Moreover a source term only appears in the equations for the top quark, which is the only massive particle in our treatment. The particles taken into account are the left-handed $SU(2)$ doublet tops,

left-handed $SU(2)$ doublet bottoms, left-handed $SU(2)$ singlet tops and the Higgs boson with chemical potentials $\mu_{t,2}$, $\mu_{b,2}$, $\mu_{t^c,2}$, $\mu_{h,2}$ and velocity perturbations $u_{t,2}$, $u_{b,2}$, $u_{t^c,2}$, $u_{h,2}$, respectively. The following interaction rates and diffusion constants are used: the weak sphaleron rate [97], the strong sphaleron rate [98], the top Yukawa rate [99], the top helicity flip rate [99], the Higgs number violating rate [99], the quark diffusion constant [99] and the Higgs diffusion constant [72] with the numerical values

$$\Gamma_{ws} = 1.0{\cdot}10^{-6}T, \quad \Gamma_{ss} = 4.9{\cdot}10^{-4}T, \quad \Gamma_y = 4.2{\cdot}10^{-3}T, \quad \Gamma_m = \frac{m_t^2(z,T)}{63T},$$

$$\Gamma_h = \frac{m_W^2(z,T)}{50T}, \quad D_q = \frac{6}{T}, \quad D_h = \frac{20}{T}. \tag{4.48}$$

The finite W-scattering rate is approximated in the transport equations by $\Gamma_W = \Gamma_h^{\text{tot}}$, where $\Gamma_i^{\text{tot}} = (D_i K_{1,i})/K_{4,i}$. We finally end up with a set of eight coupled differential equations

$$3v_{\text{w}}K_{1,t}\mu_{t,2}' + 3v_{\text{w}}K_{2,t}(m_t^2)'\mu_{t,2} + 3u_{t,2}'$$
$$-3\Gamma_y(\mu_{t,2} + \mu_{t^c,2} + \mu_{h,2}) - 6\Gamma_m(\mu_{t,2} + \mu_{t^c,2}) - 3\Gamma_W(\mu_{t,2} - \mu_{b,2})$$
$$-3\Gamma_{ss}[(1 + 9K_{1,t})\mu_{t,2} + (1 + 9K_{1,b})\mu_{b,2} + (1 - 9K_{1,t})\mu_{t^c,2}] = 0 \tag{4.49}$$

$$3v_{\text{w}}K_{1,b}\mu_{b,2}' + 3u_{b,2}'$$
$$-3\Gamma_y(\mu_{b,2} + \mu_{t^c,2} + \mu_{h,2}) - 3\Gamma_W(\mu_{b,2} - \mu_{t,2})$$
$$-3\Gamma_{ss}[(1 + 9K_{1,t})\mu_{t,2} + (1 + 9K_{1,b})\mu_{b,2} + (1 - 9K_{1,t})\mu_{t^c,2}] = 0 \tag{4.50}$$

$$3v_{\text{w}}K_{1,t}\mu_{t^c,2}' + 3v_{\text{w}}K_{2,t}(m_t^2)'\mu_{t^c,2} + 3u_{t^c,2}'$$
$$-3\Gamma_y(\mu_{t,2} + \mu_{b,2} + 2\mu_{t^c,2} + 2\mu_{h,2}) - 6\Gamma_m(\mu_{t,2} + \mu_{t^c,2})$$
$$-3\Gamma_{ss}[(1 + 9K_{1,t})\mu_{t,2} + (1 + 9K_{1,b})\mu_{b,2} + (1 - 9K_{1,t})\mu_{t^c,2}] = 0 \tag{4.51}$$

$$2v_{\text{w}}K_{1,h}\mu_{h,2}' + 2u_{h,2}'$$
$$-3\Gamma_y(\mu_{t,2} + \mu_{b,2} + 2\mu_{t^c,2} + 2\mu_{h,2}) - 2\Gamma_h\mu_{h,2} = 0 \tag{4.52}$$

$$-3K_{4,t}\mu_{t,2}' + 3v_{\text{w}}\tilde{K}_{5,t}u_{t,2}' + 3v_{\text{w}}\tilde{K}_{6,t}(m_t^2)'u_{t,2} + 3\Gamma_t^{\text{tot}}u_{t,2} =$$
$$-3v_{\text{w}}K_{8,t}(m_t^2\theta_t')' + 3v_{\text{w}}K_{9,t}m_t^2\theta_t'(m_t^2)' \tag{4.53}$$

$$-3K_{4,b}\mu_{b,2}' + 3v_{\text{w}}\tilde{K}_{5,b}u_{b,2}' + 3\Gamma_b^{\text{tot}}u_{b,2} = 0 \tag{4.54}$$

$$-3K_{4,t}\mu_{t^c,2}' + 3v_{\text{w}}\tilde{K}_{5,t}u_{t^c,2}' + 3v_{\text{w}}\tilde{K}_{6,t}(m_t^2)'u_{t^c,2} + 3\Gamma_t^{\text{tot}}u_{t^c,2} =$$
$$-3v_{\text{w}}K_{8,t}(m_t^2\theta_t')' + 3v_{\text{w}}K_{9,t}m_t^2\theta_t'(m_t^2)' \tag{4.55}$$

$$-2K_{4,h}\mu_{h,2}' + 2v_{\text{w}}\tilde{K}_{5,h}u_{h,2}' + 2\Gamma_h^{\text{tot}}u_{h,2} = 0. \tag{4.56}$$
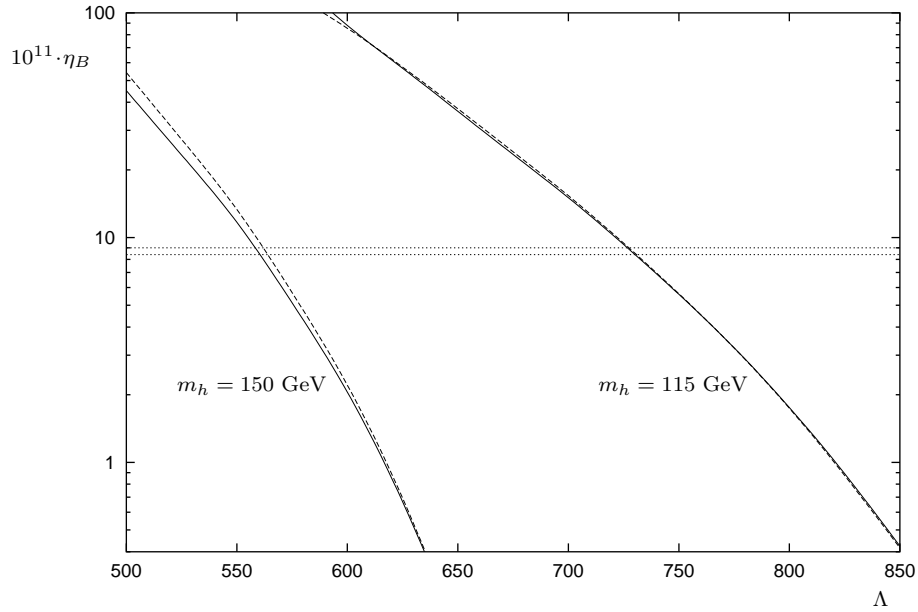
Figure 4.10: The baryon asymmetry in the φ^6 model for two Higgs masses as a function of Λ (in units of GeV). The solid lines represent $v_{\mathrm{w}} = 0.01$ and the dashed $v_{\mathrm{w}} = 0.3$. The dotted horizontal lines indicate the error band of the observed value.
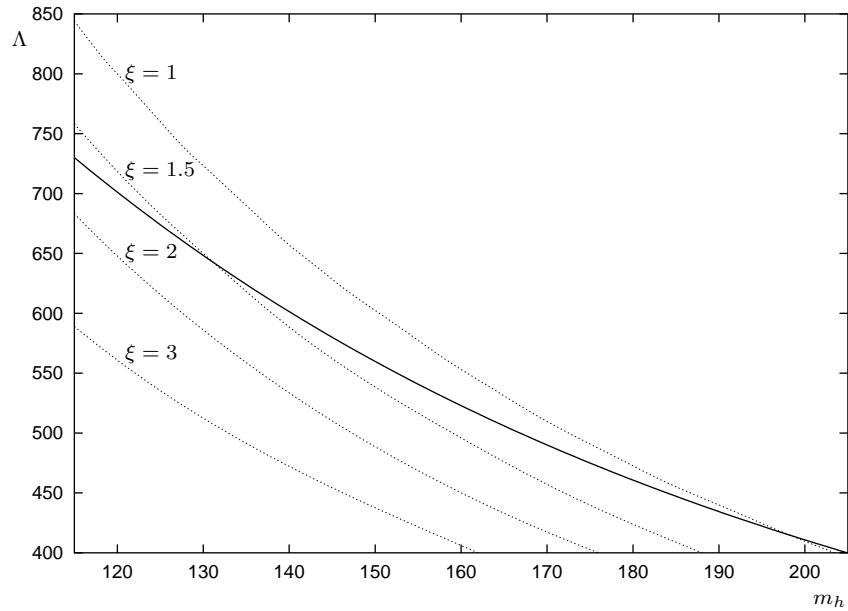

Figure 4.11: The line of constant $\eta_B = 8.7 \cdot 10^{-11}$ (solid curve) in the Λ-m_h-plane. In addition lines of constant ξ (dotted curves) as in fig. 4.3 are shown. Λ and m_h are given in units of GeV.

Eqs. (4.49)-(4.52) correspond to eq. (3.23) for t, b, t^c and h, respectively, and eqs. (4.53)-(4.56) to eq. (3.24). For a given parameter combination of m_h and Λ and the corresponding wall profile $\varphi(z)$ as well as the profile for the phase $\theta(z)$, which enter the above equations, they can be solved for a fixed value of v_{w}. According to eqs. (3.33) and (3.34) we finally derive the baryon asymmetry as a function of m_h, Λ and v_{w}.

As an example we show in fig. 4.10 the baryon asymmetry for two different Higgs masses, $m_h = 115$ and 150 GeV, in dependence of the cut-off parameter Λ. The baryon asymmetry is calculated for a small wall velocity, $v_{\mathrm{w}} = 0.01$, and a rather large value of $v_{\mathrm{w}} = 0.3$. In general η_B depends only weakly on v_{w}. The influence of v_{w} is negligible for small Higgs masses and increases only slightly for larger values of m_h. We cover a wide range of about two orders of magnitude in the baryon asymmetry, which includes also the measured value of $\eta_B = (8.7 \pm 0.3)\cdot10^{-11}$. If we move along the lines of constant $m_h = 115$ GeV the strength of the phase transition varies from $\xi \approx 1$ at $\Lambda = 850$ GeV to $\xi \approx 2.8$ for $\Lambda = 600$ GeV. The baryon asymmetry $\eta_B = 8.7\cdot10^{-11}$ is met at $\xi \approx 1.7$. In the case of $m_h = 150$ GeV one finds $\xi \approx 0.8$ at $\Lambda = 630$ GeV and $\xi \approx 1.9$ at $\Lambda = 500$ GeV as well as $\xi \approx 1.3$ for $\eta_B = 8.7\cdot10^{-11}$. In order to predict in the φ^6 model the observed asymmetry we can tune the Higgs mass up to $190 - 200$ GeV where we approach the limit $\xi = 1$ for a strong first order PT. Fig. 4.11 connects the model parameters and the strength of the PT with the value of η, which we want to explain. It shows the same parameter region and lines of constant ξ as in fig. 4.3, but in addition the line of constant $\eta_B = 8.7\cdot10^{-11}$. The wall thickness is nearly constant along this line and varies in the range $(6 - 7)\cdot T_c^{-1}$. The electric dipole moments of the electron and neutron are largest for the smallest Higgs mass. We find within our approximations $d_{\mathrm{e}} \approx 7\cdot10^{-29}\,e\,\mathrm{cm}$ and $d_{\mathrm{n}} \approx (5 - 11)\cdot10^{-28}\,e\,\mathrm{cm}$ for $m_h = 115$ GeV, which is in each case two orders of magnitude below the experimental bounds. Thus, the model presented can explain the measured baryon asymmetry for natural values of the model parameters.

Chapter 5

The Two-Higgs-Doublet Model

5.1 The tree-level potential

The simplest but rather rich extension of the Standard Model with regard to the electroweak phase transition is the two-Higgs-doublet model (2HDM) with two complex scalar fields Φ_1 and Φ_2 [100]. In its most general form flavor changing neutral currents (FCNC) are unsuppressed at tree-level. In order to forbid them a discrete symmetry is required, restricting the coupling of all fermions of a given electric charge to at most one Higgs doublet. In the "type I" model both up and down type quarks couple only to Φ_2, and in the "type II" case down type quarks couple to Φ_1, while up type quarks couple to Φ_2. The Higgs fields transform according to $\Phi_1 \to -\Phi_1$ and the down type quarks via $d_i^c \to \pm d_i^c$ for type I and II, respectively. As we only take into account the coupling of the top quark, we do not need to distinguish between the two types. If the above Z_2 symmetry is exact, also CP would be conserved. Since CP-violation is essential for baryogenesis, we can break the symmetry softly by allowing a term of the form $\Phi_1^\dagger \Phi_2$ in the potential without reintroducing FCNC at tree-level [100]. Then the potential reads

$$
\begin{aligned}
V(\Phi_1, \Phi_2) \;=\; & -\mu_1^2 \Phi_1^\dagger \Phi_1 - \mu_2^2 \Phi_2^\dagger \Phi_2 - (\mu_3^2 e^{i\alpha} \Phi_1^\dagger \Phi_2 + \text{h.c.}) \\
& + \frac{\lambda_1}{2}(\Phi_1^\dagger \Phi_1)^2 + \frac{\lambda_2}{2}(\Phi_2^\dagger \Phi_2)^2 + \lambda_3(\Phi_1^\dagger \Phi_1)(\Phi_2^\dagger \Phi_2) \\
& + \lambda_4 |\Phi_1^\dagger \Phi_2|^2 + \left(\frac{\lambda_5}{2}(\Phi_1^\dagger \Phi_2)^2 + \text{h.c.} \right).
\end{aligned}
\tag{5.1}
$$

The Yukawa interaction for the top quark is

$$
\mathscr{L}_y = y_\text{t} \overline{T}_L \widetilde{\Phi}_2 t_R + \text{h.c.}
\tag{5.2}
$$

with $\widetilde{\Phi}_2 = i\sigma_2 \Phi_2^*$. The potential contains nine parameters: five couplings λ_i, three masses μ_i and one phase α, which ensures explicit CP-violation.

In the literature this model is well known and many of its aspects have been studied so far. The 2HDM was analyzed in the context of the electroweak phase transition and baryogenesis e.g. in refs. [24–32]. An early analytic treatment was performed in ref. [24] by Bochkarev, Kuzmin and Shaposhnikov, a numerical approach was realized in ref. [27] by Turok and Zadrozny. Since the lower experimental bound on the Higgs mass was around 50 GeV at this time, they analyzed the parameter region corresponding to Higgs masses only up to 120 GeV. With regard to the current experimental limit of 115 GeV one has to enlarge the mass range. In this work we supplement the studies with the focus on requirements for electroweak baryogenesis, i.e. we scan the parameter range with regard to a strong first order phase transition, we estimate the wall thickness of the nucleating bubbles and we also check that we do not exceed experimental constraints. The results will be compared with those of the recent literature.

We follow the common practice and simplify the analysis by restricting the parameters from now on to

$$\mu_1^2 = \mu_2^2 \text{ and } \lambda_1 = \lambda_2, \tag{5.3}$$

which reduces the dimension of the parameter space from nine to seven.

CP-conserving case

In a first step we consider the CP-conserving case, i.e. $\alpha = 0$. We parameterize the neutral components of the Higgs fields via $\Phi_1^0 = h_1$ and $\Phi_2^0 = h_2$. Note that we do not introduce the usual factor $1/\sqrt{2}$. Then the potential reads

$$V(h_1, h_2) = -\mu_1^2(h_1^2 + h_2^2) - 2\mu_3^2 h_1 h_2 + \frac{\lambda_1}{2}(h_1^4 + h_2^4) + (\lambda_3 + \lambda_4 + \lambda_5)h_1^2 h_2^2. \tag{5.4}$$

Eq. (5.3) implies the symmetry $\Phi_1 \leftrightarrow \Phi_2^\dagger$, so that the minimum is at $\langle h_1 \rangle = \langle h_2 \rangle = h$ and therefore

$$\tan(\beta) = \frac{\langle h_2 \rangle}{\langle h_1 \rangle} = 1. \tag{5.5}$$

For the minimum conditions

$$\left. \frac{\partial V}{\partial h_1} \right|_{h_1 = h_2 = h} = \left. \frac{\partial V}{\partial h_2} \right|_{h_1 = h_2 = h} = 0 \tag{5.6}$$

we get the equation

$$-\mu_1^2 - \mu_3^2 + (\lambda_1 + \lambda_3 + \lambda_4 + \lambda_5)h^2 = 0. \tag{5.7}$$

The mass matrix, which is an 8×8 matrix, is block diagonal with 2×2 blocks and gives the following particle spectrum: three massless Goldstone bosons $(G^0, G^\pm)$, two charged Higgs bosons $(H^\pm)$, one neutral and CP-odd (A^0), and two neutral and

CP-even Higgs bosons (H^0, h^0). Their squared masses in terms of the parameters are:

$$\begin{aligned}
m_{H^\pm}^2 &= 2\mu_3^2 - 2(\lambda_4 + \lambda_5)h^2, & (5.8)\\
m_{A^0}^2 &= 2\mu_3^2 - 4\lambda_5 h^2, & (5.9)\\
m_{H^0}^2 &= 2\mu_3^2 - 2(-\lambda_1 + \lambda_3 + \lambda_4 + \lambda_5)h^2, & (5.10)\\
m_{h^0}^2 &= 2(\lambda_1 + \lambda_3 + \lambda_4 + \lambda_5)h^2. & (5.11)
\end{aligned}$$

For our analysis of the phase structure we want to specify physical quantities, not the parameters in eq. (5.1). Thus, we write the six parameters of the potential in terms of four masses and one vacuum expectation value. However, one parameter remains as a free input value, for which we choose μ_3^2. Then the set of equations reads

$$\begin{aligned}
\lambda_1 &= \frac{1}{4h^2}(m_{h^0}^2 + m_{H^0}^2 - 2\mu_3^2),\\[4pt]
\lambda_3 &= \frac{1}{4h^2}(m_{h^0}^2 - m_{H^0}^2 + 2m_{H^\pm}^2 - 2\mu_3^2),\\[4pt]
\lambda_4 &= \frac{1}{4h^2}(m_{A^0}^2 - 2m_{H^\pm}^2 + 2\mu_3^2),\\[4pt]
\lambda_5 &= \frac{-1}{4h^2}(m_{A^0}^2 - 2\mu_3^2). & (5.12)
\end{aligned}$$

In the case of degenerate heavy Higgs masses, $m_{H^\pm} = m_{A^0} = m_{H^0}$, one finds the equalities $\lambda_1 = \lambda_3$ and $\lambda_4 = \lambda_5$.

CP-violating case

Let us now switch on the CP-violating phase α. The neutral Higgs components can be parameterized by

$$\Phi_1^0 = h_1 e^{-i\theta_1} \quad \text{and} \quad \Phi_2^0 = h_2 e^{i\theta_2}. \qquad (5.13)$$

Note that the potential depends only on the sum $\theta = \theta_1 + \theta_2$. And at the minimum we can always choose the gauge such that $\theta_1 = \theta_2 = \theta/2$. Then we obtain for the potential

$$\begin{aligned}
V(h_1, h_2, \theta) &= -\mu_1^2(h_1^2 + h_2^2) - 2\mu_3^2 h_1 h_2 \cos(\theta + \alpha) + \frac{\lambda_1}{2}(h_1^4 + h_2^4)\\
&\quad + (\lambda_3 + \lambda_4 + \lambda_5 \cos 2\theta)h_1^2 h_2^2. & (5.14)
\end{aligned}$$

Again we get one equation from the minimum conditions (5.6), evaluated at the VEVs $\langle h_1 \rangle = \langle h_2 \rangle = h$ and $\langle \theta \rangle = \theta_0$,

$$-\mu_1^2 - \mu_3^2 \cos(\theta_0 + \alpha) + (\lambda_1 + \lambda_3 + \lambda_4 + \lambda_5 \cos 2\theta_0)h^2 = 0, \qquad (5.15)$$

and a second equation from the derivative of V with respect to θ,

$$\mu_3^2 \sin(\theta_0 + \alpha) - \lambda_5 h^2 \sin 2\theta_0 = 0. \tag{5.16}$$

The mass matrix still splits into a part for the charged and a part for the neutral Higgs fields, but the sub-matrices are no longer block diagonal. The computation of the Higgs masses is carried out in appendix A. Due to the CP-violation the mass eigenstates in the neutral sector are mixtures of CP odd and even states, and we now label the Higgs masses with $H_1, H_2,$ and H_3 where H_1 refers to the light and the two others to the heavier Higgs bosons. The resulting squared masses are

$$m_{H^\pm}^2 = -2\mu_1^2 + 2(\lambda_1 + \lambda_3)h^2, \tag{5.17}$$

$$m_{H_3}^2 = -\mu_1^2 + 2(\lambda_1 + \lambda_3 + \lambda_4)h^2 + \sqrt{\mu_1^4 + 4\lambda_5 \cos(2\theta_0)\mu_1^2 h^2 + 4\lambda_5^2 h^4}, \tag{5.18}$$

$$m_{H_2}^2 = -2\mu_1^2 + 4\lambda_1 h^2, \tag{5.19}$$

$$m_{H_1}^2 = -\mu_1^2 + 2(\lambda_1 + \lambda_3 + \lambda_4)h^2 - \sqrt{\mu_1^4 + 4\lambda_5 \cos(2\theta_0)\mu_1^2 h^2 + 4\lambda_5^2 h^4}. \tag{5.20}$$

With α we have an additional parameter, and therefore also an additional VEV, θ_0. Since we chose μ_3^2 as a free input parameter, we treat the related phase α in the same manner. In contrast to the CP-conserving case it is no longer possible to invert the set of equations (5.15)-(5.20) analytically. But we can solve it for the parameters $\mu_1^2, \lambda_1, \lambda_3, \lambda_4, \lambda_5, \theta_0$ numerically for given values of $m_{H^\pm}^2, m_{H_3}^2, m_{H_2}^2, m_{H_1}^2, \mu_3^2, \alpha,$ and h. We set $h = 123$ GeV in order to obtain the measured VEV $v = \sqrt{2}\sqrt{\langle h_1 \rangle^2 + \langle h_2 \rangle^2} = 246$ GeV where the factor $\sqrt{2}$ is due to our field normalization.

In the following we restrict ourselves to the case of degenerate heavy Higgs masses to decrease the dimension of the parameter space and introduce the notation $m_h = m_{H_1}$ and $m_H = m_{H_2} = m_{H_3} = m_{H^\pm}$. We still find $\lambda_1 = \lambda_3$ as in the CP-conserving case, but the equality between λ_4 and λ_5 is broken now, roughly at the order θ^2.

5.2 The one-loop potential

Up to now we dealt with the tree-level potential, which we will label with the subscript "0" in the following:

$$\begin{aligned}
V_0(\Phi_1, \Phi_2) &= -\mu_1^2 \left(\Phi_1^\dagger \Phi_1 + \Phi_2^\dagger \Phi_2 \right) - \mu_3^2 \left(e^{i\alpha} \Phi_1^\dagger \Phi_2 + e^{-i\alpha} \Phi_2^\dagger \Phi_1 \right) \\
&\quad + \frac{\lambda_1}{2} \left((\Phi_1^\dagger \Phi_1)^2 + (\Phi_2^\dagger \Phi_2)^2 \right) + \lambda_3 (\Phi_1^\dagger \Phi_1)(\Phi_2^\dagger \Phi_2) \\
&\quad + \lambda_4 (\Phi_1^\dagger \Phi_2)(\Phi_2^\dagger \Phi_1) + \frac{\lambda_5}{2} [(\Phi_1^\dagger \Phi_2)^2 + (\Phi_2^\dagger \Phi_1)^2]. \tag{5.21}
\end{aligned}$$

For the analysis of the EWPT we have to take into account one-loop corrections given by the Coleman-Weinberg expression [42]

$$V_1(\Phi_1, \Phi_2) = \sum_i \pm n_i \frac{1}{64\pi^2} m_i^4 \ln \frac{m_i^2}{Q^2}, \qquad (5.22)$$

where m_i are the field dependent tree-level masses of the particles involved and n_i count the degrees of freedom. Plus and minus refer to bosons and fermions, respectivly. For the renormalization scale we take $Q = v/\sqrt{2} = 246/\sqrt{2}$ GeV. The major contributions come from the heavy particles in the theory, thus we include the four heavy Higgs bosons and the top quark in the one-loop term. The degrees of freedom for the Higgs bosons are $n_{\mathrm{Higgs}} = 1$ and for the top quark $n_{\mathrm{t}} = 12$. The squared Higgs masses are the eigenvalues of the tree-level mass matrix, which we evaluate numerically for given field configurations, and the squared top mass is given by

$$m_{\mathrm{t}}^2 = y_{\mathrm{t}}^2 \Phi_2^\dagger \Phi_2 \qquad (5.23)$$

where we use for the Yukawa top coupling $y_{\mathrm{t}} = 1.3415$. In practice one has to deviate slightly from the case of degenerate heavy Higgs masses, to which we originally restricted, because we need to assign the eigenvalues of the mass matrix to the corresponding mass eigenstates in a unique manner. Therefore we choose in the following

$$m_{H^\pm} = m_H + 1 \text{ GeV}, \qquad m_{H_3} = m_H, \qquad m_{H_2} = m_H - 1 \text{ GeV}.$$

Since the masses are of the order of a few hundred GeV the deviations are very small and we still call this case "degenerate".

The VEVs and the mass matrix derived from the potential $V_0 + V_1$ would of course differ from those due to the tree-level contribution V_0. As a consequence we have to renormalize the parameters in order to recover the four tree-level values for the Higgs masses and the three appropriate minimum conditions for the fields h_1, h_2 and θ. This requires seven renormalization conditions and the introduction of a counter-term potential

$$
\begin{aligned}
V_{\mathrm{C}}(\Phi_1, \Phi_2) &= -\delta\mu_1^2 \left(\Phi_1^\dagger \Phi_1 + \Phi_2^\dagger \Phi_2\right) - \delta\mu_3^2 \left(e^{i\alpha}\Phi_1^\dagger \Phi_2 + e^{-i\alpha}\Phi_2^\dagger \Phi_1\right) \\
&\quad + \frac{\delta\lambda_1}{2}(\Phi_1^\dagger \Phi_1)^2 + \frac{\delta\lambda_2}{2}(\Phi_2^\dagger \Phi_2)^2 + \delta\lambda_3(\Phi_1^\dagger \Phi_1)(\Phi_2^\dagger \Phi_2) \\
&\quad + \delta\lambda_4(\Phi_1^\dagger \Phi_2)(\Phi_2^\dagger \Phi_1) + \frac{\delta\lambda_5}{2}[(\Phi_1^\dagger \Phi_2)^2 + (\Phi_2^\dagger \Phi_1)^2]. \qquad (5.24)
\end{aligned}
$$

Due to the coupling of the top quark to only one of the Higgs doublets the symmetry of eq. (5.3) no longer holds. Therefore we have to distinguish between the counter-term couplings $\delta\lambda_1$ and $\delta\lambda_2$. An other choice would have been $\delta\mu_1^2$ and $\delta\mu_2^2$. One disadvantageous but inevitable feature is the renormalization of μ_3^2, which we chose as an input parameter. The counter-term potential changes the VEV θ_0 due to the

$(\Phi_1^\dagger \Phi_2 + \text{h.c.})$-term in V_0, which is the source for the necessary CP-violation. The renormalization condition of fixing θ_0 results in a counter term for either μ_3^2 or α. Since the phase α appears in sine and cosine functions, one cannot solve the set of renormalization conditions even numerically for $\delta\alpha$. Thus, the only possibility is to introduce $\delta\mu_3^2$, which gives a set of linear, quadratic and cubic equations, as we will show in the following.

First we parameterize the potential to one-loop order with the fields h_1, h_2 and θ,

$$V(h_1, h_2, \theta) = V_0(h_1, h_2, \theta) + V_C(h_1, h_2, \theta) + V_1(h_1, h_2, \theta). \tag{5.25}$$

The three minimum conditions read

$$\left.\frac{\partial V}{\partial h_1}\right|_{h_1=h_2=h,\, \theta=\theta_0} = 0, \tag{5.26}$$

$$\left.\frac{\partial V}{\partial h_2}\right|_{h_1=h_2=h,\, \theta=\theta_0} = 0, \tag{5.27}$$

$$\left.\frac{\partial V}{\partial \theta}\right|_{h_1=h_2=h,\, \theta=\theta_0} = 0 \tag{5.28}$$

where the derivatives of V_0 and V_C can be performed analytically, but the derivatives of V_1 have to be approximated by the difference quotients

$$\left.\frac{\partial V_1}{\partial h_1}\right|_{h_1=h_2=h,\, \theta=\theta_0} = \frac{1}{2\varepsilon_h}\Big(V_1(h+\varepsilon_h, h, \theta_0) - V_1(h-\varepsilon_h, h, \theta_0)\Big), \tag{5.29}$$

$$\left.\frac{\partial V_1}{\partial h_2}\right|_{h_1=h_2=h,\, \theta=\theta_0} = \frac{1}{2\varepsilon_h}\Big(V_1(h, h+\varepsilon_h, \theta_0) - V_1(h, h-\varepsilon_h, \theta_0)\Big), \tag{5.30}$$

$$\left.\frac{\partial V_1}{\partial \theta}\right|_{h_1=h_2=h,\, \theta=\theta_0} = \frac{1}{2\varepsilon_\theta}\Big(V_1(h, h, \theta_0+\varepsilon_\theta) - V_1(h, h, \theta_0-\varepsilon_\theta)\Big). \tag{5.31}$$

We adjust $\varepsilon_h = 0.1$ and $\varepsilon_\theta = 0.001$ to the magnitudes of h and θ, which are $\mathcal{O}(h) = 100$ and $\mathcal{O}(\theta) = 1$.

In order to derive the renormalization conditions for the Higgs masses we parameterize the doublets with eight real fields

$$\Phi_1 = \begin{pmatrix} \varphi_1 + i\,\varphi_2 \\ \varphi_5 + i\,\varphi_6 \end{pmatrix} \quad \text{and} \quad \Phi_2 = \begin{pmatrix} \varphi_3 + i\,\varphi_4 \\ \varphi_7 + i\,\varphi_8 \end{pmatrix} \tag{5.32}$$

and compute the tree-level and the one-loop mass matrices

$$M_0 = \frac{1}{2}\left.\frac{\partial^2 V_0}{\partial\varphi_i \partial\varphi_j}\right|_{\text{VEV}}, \tag{5.33}$$

$$M = \frac{1}{2}\left.\frac{\partial^2 V}{\partial\varphi_i \partial\varphi_j}\right|_{\text{VEV}} \tag{5.34}$$

where VEV means $\varphi_1 = \varphi_2 = \varphi_3 = \varphi_4 = 0$, $\varphi_5 = \varphi_7 = h\cos(\theta_0/2)$, $\varphi_6 = -\varphi_8 = -h\sin(\theta_0/2)$. We cannot directly compare the tree-level and one-loop masses because this requires the knowledge of how to diagonalize the matrices analytically. M is a function of the renormalization parameters and therefore cannot be treated numerically either. We restrict to the comparison of only the characteristic polynomials of M_0 and M, which is also sufficient. If the characteristic polynomials of two matrices are equal then also their eigenvalues coincide.

M_0 and M split in each case into a part for the charged and neutral components

$$M_0 = \begin{pmatrix} C_0 & 0 \\ 0 & N_0 \end{pmatrix}, \tag{5.35}$$

$$M = \begin{pmatrix} C & 0 \\ 0 & N \end{pmatrix}. \tag{5.36}$$

Again we have to approximate the second derivative for the V_1 part by

$$\frac{\partial^2 V_1}{\partial \varphi_i \partial \varphi_j} = \frac{1}{(2\varepsilon)^2}\Big(V_1(\vec{\varphi} + \varepsilon\hat{e}_i + \varepsilon\hat{e}_j) + V_1(\vec{\varphi} - \varepsilon\hat{e}_i - \varepsilon\hat{e}_j)$$
$$- V_1(\vec{\varphi} + \varepsilon\hat{e}_i - \varepsilon\hat{e}_j) - V_1(\vec{\varphi} - \varepsilon\hat{e}_i + \varepsilon\hat{e}_j)\Big) \tag{5.37}$$

with the notation $\vec{\varphi} = (\varphi_1, \ldots, \varphi_8)$ and $\hat{e}_i =$ unit vector in i-direction. We take $\varepsilon = 0.1$.

As the part C_0 yields two charged mass-degenerated and two massless Higgs bosons its characteristic polynomial P_c^0 factorizes in the following way:

$$\begin{aligned} P_c^0(x) &= \det\Big(C_0|_{\text{VEV}} - x\,\mathbb{1}_4 \Big) \\ &= (x - m_{H^\pm}^2)^2\, x^2 \\ &= x^4 \underbrace{-2m_{H^\pm}^2}_{c_3^0} x^3 + \underbrace{m_{H^\pm}^4}_{c_2^0} x^2 \end{aligned} \tag{5.38}$$

where we denote in general the coefficients of x^i with c_i^0. The same holds for P_c, the characteristic polynomial of the matrix C,

$$\begin{aligned} P_c(x) &= \det\Big(C|_{\text{VEV}} - x\,\mathbb{1}_4 \Big) \\ &= x^4 + c_3\, x^3 + c_2\, x^2 \end{aligned} \tag{5.39}$$

where the c_i are polynomials of the renormalized parameters. Due to our numerical approximation the coefficients c_1 and c_0 are not exactly zero as in the equation above but rather small. Anyway, it is sufficient to demand the equality of c_3^0 and c_3, which gives us a linear equation for the fourth renormalization condition

$$c_3^0 = c_3. \tag{5.40}$$

In an analogous manner we treat the neutral parts N_0 and N. We derive the polynomials P_n^0 and P_n

$$
\begin{aligned}
P_n^0(x) &= \det\left(N_0|_{\text{VEV}} - x\,\mathbb{1}_4\right) \\
&= x^4 + n_3^0\,x^3 + n_2^0\,x^2 + n_1^0\,x, \qquad\qquad (5.41) \\
P_n(x) &= \det\left(N|_{\text{VEV}} - x\,\mathbb{1}_4\right) \\
&= x^4 + n_3\,x^3 + n_2\,x^2 + n_1\,x \qquad\qquad (5.42)
\end{aligned}
$$

and set up the last three conditions

$$
\begin{aligned}
n_3^0 &= n_3, \qquad\qquad\qquad\qquad (5.43) \\
n_2^0 &= n_2, \qquad\qquad\qquad\qquad (5.44) \\
n_1^0 &= n_1, \qquad\qquad\qquad\qquad (5.45)
\end{aligned}
$$

which are linear, quadratic and cubic equations in the renormalization parameters, respectively. This set of seven equations, (5.26)-(5.28), (5.40), (5.43)-(5.45), can be solved numerically.

In general, it has six solutions, from which two are complex and four real in the case of $\alpha \approx 0$ and the opposite way for non-vanishing α. The real solutions, which we are only interested in, differ slightly in their values for the parameters. By construction these cases lead to the same pre-determined eigenvalues of the mass matrix, but to
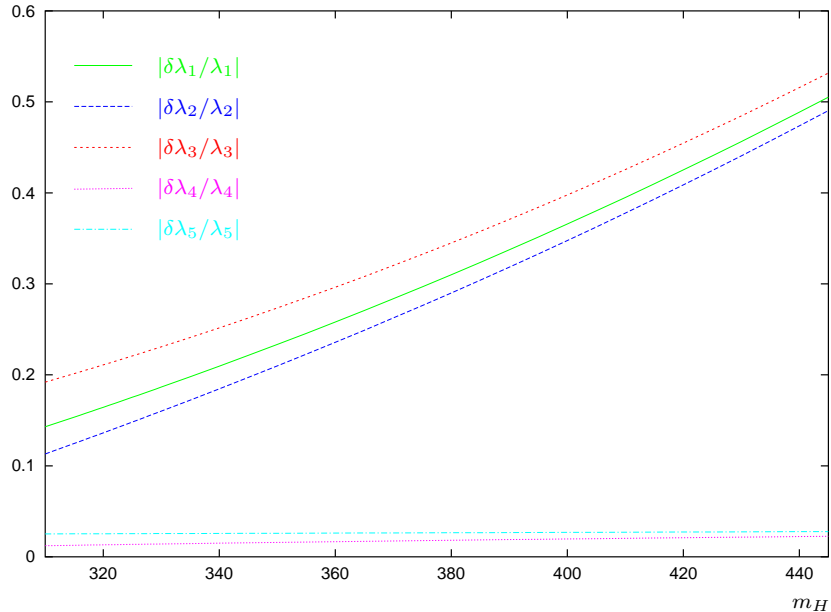
Figure 5.1: $|\delta\lambda_i/\lambda_i|$ in dependence of m_H for $\mu_3^2 = 10000$ GeV^2, $\alpha = 0.2$, and $m_h = 150$ GeV. m_H is given in units of GeV.
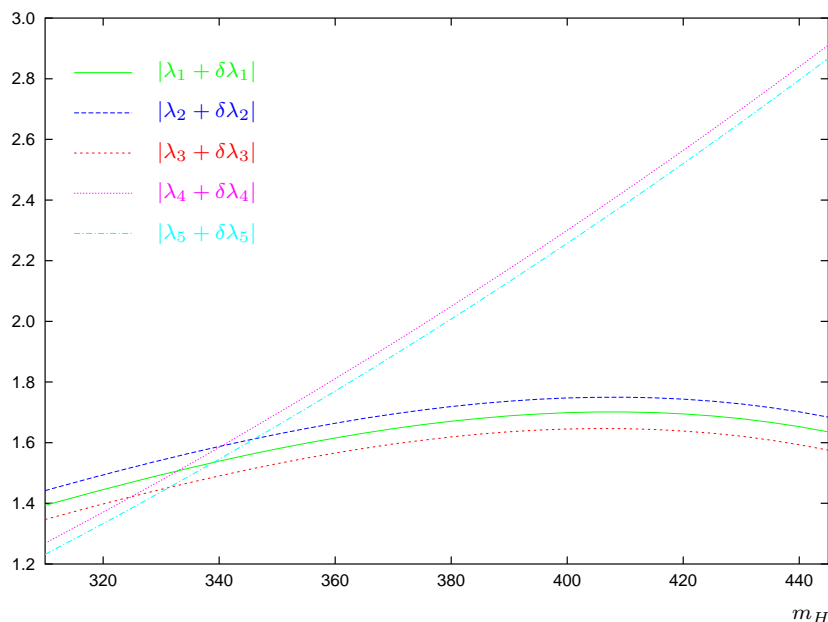
Figure 5.2: $|\lambda_i + \delta\lambda_i|$ in dependence of m_H (in units of GeV) for $\mu_3^2 = 10000\,\mathrm{GeV}^2$, $\alpha = 0.2$, and $m_h = 150\,\mathrm{GeV}$.

different eigenvectors. We have to set up a unique criterion of choosing one of the solutions. We do not specify and analyze the degree of mixing between the fields, but we pay attention to the relative deviation of the parameters. Thus we select the solution with the smallest ratio of the renormalization parameters to the tree-level values. If the corrections of $\lambda_1, \ldots, \lambda_5$ become too large then perturbation theory no longer holds. In order to avoid this problem we impose an upper limit of 0.5 on the ratio $|\delta\lambda_i/\lambda_i|$, $i = 1, \ldots, 5$, which constrains the parameter space. We found that in the parameter region analyzed the dominant ratio always originates from $|\delta\lambda_3/\lambda_3|$ while $|\delta\lambda_1/\lambda_1|$ and $|\delta\lambda_2/\lambda_2|$ are somewhat lower. The corrections of λ_4 and λ_5 are negligible. Moreover the ratios show a rather weak dependence of the light Higgs mass, but they become larger with increasing heavy Higgs mass. A change in the phase α affects them only very little, and an increasing μ_3^2 results in a small shift to lower values. The behavior of $|\delta\lambda_i/\lambda_i|$ in dependence of m_H is shown in fig. 5.1 for the example $\mu_3^2 = 10000\,\mathrm{GeV}^2$, $\alpha = 0.2$, $m_h = 150\,\mathrm{GeV}$, which is a typical representative.

The order of the absolute values of the one-loop parameters $|\lambda_i + \delta\lambda_i|$ is contrary to the ratios. In a wide range $|\lambda_4 + \delta\lambda_4|$ and $|\lambda_5 + \delta\lambda_5|$ are the dominant parameters and they grow approximately linearly with increasing m_H. The other three parameters show a weaker dependence on the heavy Higgs mass and reach a maximum. This behavior is presented for the above example in fig. 5.2. The equality of λ_1 and λ_3 is broken on one hand due to the slightly different heavy masses at tree-level by about two percent, and on the other hand at the one-loop level. $\lambda_1 + \delta\lambda_1$ and $\lambda_3 + \delta\lambda_3$ differ by about three to five percent.

5.3 The effective potential at finite temperature

Recall the thermal contribution to the effective potential at one-loop order, (2.29),

$$\Delta V_{\text{eff,T}} = T^4 \sum_B n_B \, f_{\text{B}}(m_B/T) \; + \; T^4 \sum_F n_F \, f_{\text{F}}(m_F/T). \qquad (5.46)$$

The degrees of freedom are for the Higgs bosons $n_{\text{Higgs}} = 1$, for the gauge bosons $n_{\text{W}} = 6$ and $n_{\text{Z}} = 3$ and for the top quark $n_{\text{t}} = 12$, which are the particles we take into account. The W and Z masses are given by

$$m_W^2 \;\; = \;\; \frac{g_2^2}{2} \left(\Phi_1^\dagger \Phi_1 + \Phi_2^\dagger \Phi_2 \right) \qquad (5.47)$$

$$m_Z^2 \;\; = \;\; \frac{g_1^2 + g_2^2}{2} \left(\Phi_1^\dagger \Phi_1 + \Phi_2^\dagger \Phi_2 \right). \qquad (5.48)$$

In the Higgs sector we consider only the four heavy bosons. The approximations for the bosonic and fermionic functions f_{B} and f_{F} in the high temperature limit (m/T small) read up to the quartic term:

$$f_{\text{B}}^{\text{HT}}(m/T) \;\; \approx \;\; \frac{-\pi^2}{90} + \frac{(m/T)^2}{24} - \frac{(m/T)^3}{12\pi} - \frac{(m/T)^4}{64\pi^2} \ln \left[\frac{(m/T)^2}{c_{\text{B}}} \right], \quad (5.49)$$

$$f_{\text{F}}^{\text{HT}}(m/T) \;\; \approx \;\; \frac{-7\pi^2}{720} + \frac{(m/T)^2}{48} + \frac{(m/T)^4}{64\pi^2} \ln \left[\frac{(m/T)^2}{c_{\text{F}}} \right] \qquad (5.50)$$

with $c_{\text{F}} = \pi^2 \exp(3/2 - 2\gamma_e) \approx 13.94$ and $c_{\text{B}} = 16 c_{\text{F}}$. The error of the high temperature expansion is less than ten percent up to $m/T \lesssim 2.5$ for $f_{\text{B}}^{\text{HT}}(m/T)$ and up to $m/T \lesssim 1.9$ for $f_{\text{F}}^{\text{HT}}(m/T)$. Since rather heavy Higgs masses of the order of a few hundred GeV occur in our model and the typical critical temperature T_c of the phase transition is about 100 GeV, we exceed the range where the expansion f_{B}^{HT} can be regarded as valid. As an example fig. 5.3 shows the field dependent mass $m_{H_3}(h_1, h_2, \theta)$ divided by $T \approx T_c$ for two different sets of m_h and m_H. The ratio is plotted versus h_1 along the line $h_1 = h_2$ and $\theta = 0$ in the field hyperplane. The two examples cover the range of m/T appearing in our analysis. While for the first parameter set (dotted red line) the ratio is partly quite small and the high T expansion is valid, in the second example (dashed blue line) m/T is considerably larger. In order to still deal with analytic rather than integral expressions it is convenient to use the high temperature expansion for small m/T, a low temperature expansion for large m/T and a smooth interpolation in-between to avoid discontinuities. The horizontal dotted lines in fig. 5.3 divide the three regions. In the low temperature limit f_{B} and f_{F} can be approximated by

$$f^{\text{LT}}(m/T) \;\; = \;\; f_{\text{B}}^{\text{LT}}(m/T) = f_{\text{F}}^{\text{LT}}(m/T)$$

$$\approx \;\; -\left(\frac{m/T}{2\pi} \right)^{3/2} e^{-m/T} (1 + \frac{15}{8} \, m/T). \qquad (5.51)$$

We follow the choice in ref. [101] and define for the bosonic and fermionic functions the approximations

$$
\tilde{f}_B(x) = \begin{cases} f_B^{HT}(x) & x < 1.8 \\ \frac{-0.39 + 0.05069x}{5.2186 - 1.8874x + x^2} & 1.8 < x < 4.5 \\ f^{LT}(x) & x > 4.5 \end{cases} ,
\tag{5.52}
$$

$$
\tilde{f}_F(x) = \begin{cases} f_F^{HT}(x) & x < 1.1 \\ \frac{-0.6087 + 0.0856x}{6.321 - 0.725x + x^2} & 1.1 < x < 3.4 \\ f^{LT}(x) & x > 3.4 \end{cases} .
\tag{5.53}
$$

Their derivatives are continuous so that numerical minimization algorithms based on derivatives can be used to determine the broken minimum of the effective potential. The deviations from the integral expressions are less then four percent in the whole range.

Now we end up with the one-loop effective potential at finite temperature by taking the sum of the different contributions, eqs. (5.21), (5.22), (5.24) and (5.46),

$$
V_{\text{eff,T}}(h_1, h_2, \theta, T) = V_0 + V_1 + V_C + \Delta V_{\text{eff,T}}.
\tag{5.54}
$$
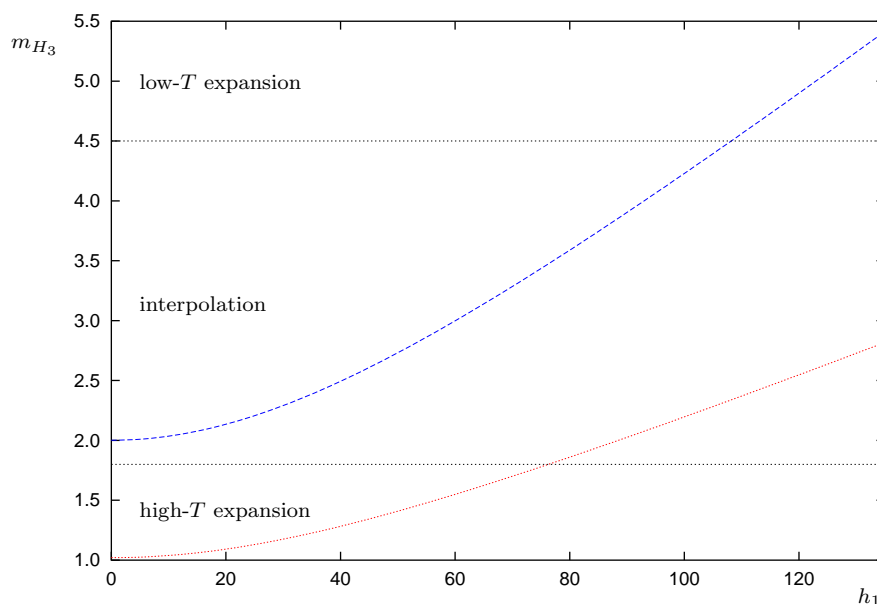
Figure 5.3: The ratio $m_{H_3}(h_1, h_1, 0)/T$ in dependence of h_1 for the parameter sets $m_h = 190$ GeV, $m_H = 390$ GeV, $T = 150$ GeV (dotted red) and $m_h = 120$ GeV, $m_H = 450$ GeV, $T = 90$ GeV (dashed blue), both at $\mu_3^2 = 20000$ GeV^2, $\alpha = 0.2$. h_1 is given in units of GeV.

5.4 The shape of the effective potential

For successful baryogenesis the parameter space has to be scanned for a strong first order phase transition. We first determine the critical temperature T_c for a given set of parameters by minimizing the thermal effective potential with respect to the fields h_1, h_2 and θ. At T_c the potential develops two degenerate minima. The broken minimum is located at $\langle h_1 \rangle_T = h_{1,\mathrm{brk}}$, $\langle h_2 \rangle_T = h_{2,\mathrm{brk}}$ and $\langle \theta \rangle_T = \theta_{\mathrm{brk}}$. The non-zero expectation value at the critical temperature is defined by

$$v_c = \sqrt{2} \sqrt{h_{1,\mathrm{brk}}^2 + h_{2,\mathrm{brk}}^2} \tag{5.55}$$

and the strength of the phase transition is

$$\xi = \frac{v_c}{T_c}. \tag{5.56}$$

While at zero-temperature the relation $\tan(\beta) = 1$ is fixed, at T_c the angle between $h_{1,\mathrm{brk}}$ and $h_{2,\mathrm{brk}}$ differs slightly from $\pi/4$ and we define

$$\tan(\beta_T) = \frac{h_{2,\mathrm{brk}}}{h_{1,\mathrm{brk}}}. \tag{5.57}$$

In the symmetric minimum h_1 and h_2 are equal to zero and θ is actually not specified. But one can define a phase in this case as the limit

$$\theta_{\mathrm{sym}} = \lim_{\substack{h_1 \to 0 \\ h_2 \to 0}} \theta_{\mathrm{min}}(h_1, h_2) \tag{5.58}$$

where θ_{min} is the value that minimizes $V_{\mathrm{eff,T}}$ for given h_1 and h_2.

Let us discuss the shape of the effective potential considering as example the parameter set $\mu_3^2 = 10000$ GeV^2, $\alpha = 0.2$, $m_h = 150$ GeV and $m_H = 350$ GeV. The critical temperature turns out to be $T_c \approx 126.33$ GeV. T_c and further observables are summarized in table 5.1. Since we cannot solve the minimum condition $V_{\mathrm{eff,T}}(h_{1,\mathrm{brk}}, h_{2,\mathrm{brk}}, \theta_{\mathrm{brk}}, T_c) = 0$ exactly we require

$$\frac{V_{\mathrm{eff,T}}(h_{1,\mathrm{brk}}, h_{2,\mathrm{brk}}, \theta_{\mathrm{brk}}, T_c)}{V_b(T_c)} \leq 3\% \tag{5.59}$$

$T_c/$GeV	$v_c/$GeV	ξ	$\tan(\beta_T)$	θ_{sym}	θ_{brk}	$V_b/$GeV^4	L_{w}/T_c	$\delta\lambda_3/\lambda_3$
126.33	165.67	1.31	0.913	-0.290	-0.061	$2.48{\cdot}10^6$	4.70	0.27

Table 5.1: Observables for the example $\mu_3^2 = 10000$ GeV^2, $\alpha = 0.2$, $m_h = 150$ GeV, $m_H = 350$ GeV.

where V_b is the height of the potential barrier separating the two minima. The determination of V_b is not trivial because the effective potential depends on three parameters. A first and rather simply computable estimate would be the maximum of $V_{\text{eff,T}}$ along the direct line $h_2/h_1 = \tan(\beta_T)$ and $\theta = \theta_{\text{brk}}$. Let us denote this estimate with $\widetilde{V}_b$. Moreover $\widetilde{V}_b$ deviates from the actual barrier as we will see below. In order to determine V_b we first search for a minimum of $V_{\text{eff,T}}$ in the variables h_2 and θ for fixed h_1 and $T = T_c$. This procedure is carried out for several discrete values of h_1 between 0 and $h_{1,\text{brk}}$. A smooth interpolation of these values results in a line, parameterized by h_1, in the h_1-h_2-θ-space, which characterizes the path along which a classical particle would travel form one minimum into the other with minimal energy. We refer to this line as the "minimum line". The maximum of the effective potential along the minimum line is the potential barrier V_b. The shape of the potential is shown in fig. 5.4 for three different temperatures to get an idea how it evolves with T. Another type of illustration is a contour plot in the h_1-h_2-plane, see fig. 5.5, which points out the surface of the potential together with the minimum line. We choose the axes perpendicular to the h_1 and h_2 axes because the potential rises steeply off the diagonal direction $h_1 = h_2$ and the detailed structure would not become clear otherwise. The phase θ is fixed at θ_{brk} in the plot. The potential barrier in this example is $V_b = 2.48 \cdot 10^6 \text{ GeV}^4$, which is considerably lower than the maximal height of the potential along the straight line between the two minima. Here $\widetilde{V}_b$ reaches $3.13 \cdot 10^6 \text{ GeV}^4$. In general, the ratio $V_b/\widetilde{V}_b$ is less than, but close to one. In most cases it varies from about 0.5 to about one, for some
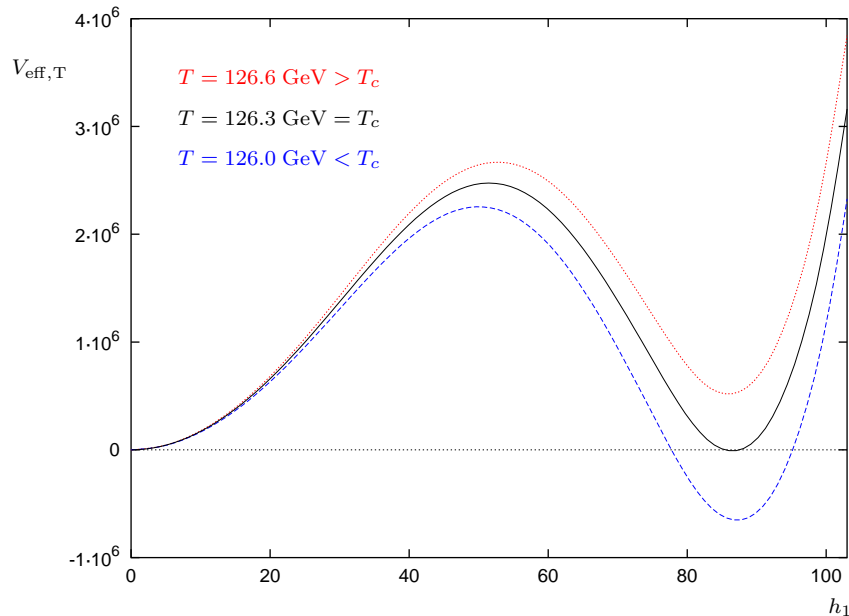

Figure 5.4: $V_{\text{eff,T}}$ (in units of GeV^4) versus h_1 (in GeV) along the minimum line in the h_1-h_2-θ-hyperplane for three different temperatures and the parameter set $\mu_3^2 = 10000 \text{ GeV}^2$, $\alpha = 0.2$, $m_h = 150 \text{ GeV}$, $m_H = 350 \text{ GeV}$.
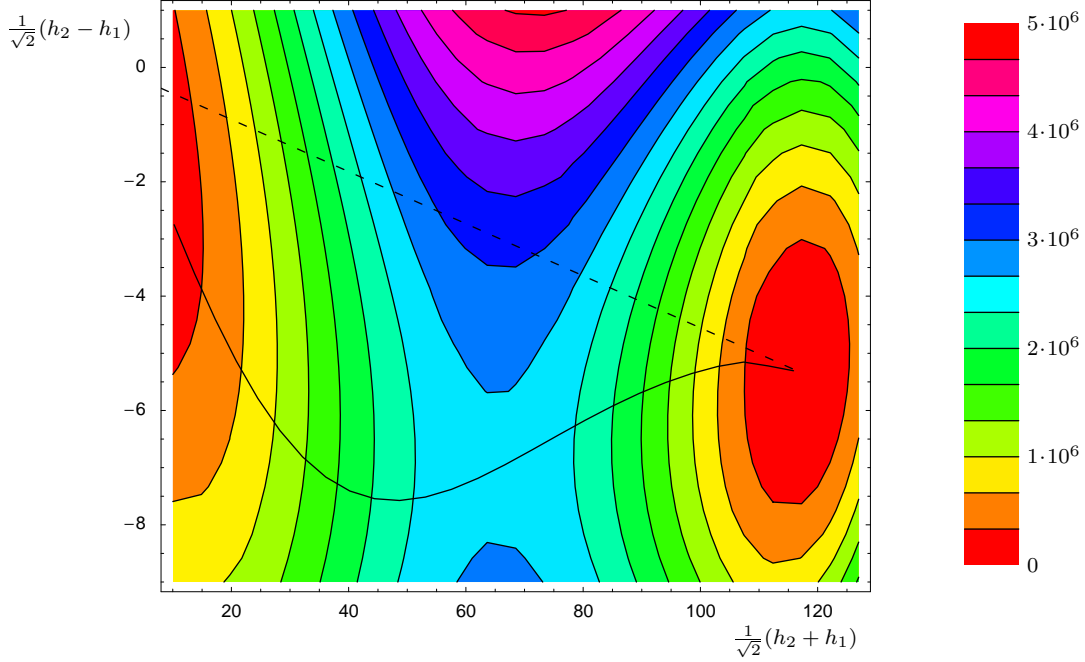
Figure 5.5: A contour plot of $V_{\text{eff,T}}$ for the above example at $T = T_c$ and fixed $\theta = \theta_{\text{brk}}$. The height is encoded by the color spectrum from 0 to $5 \cdot 10^6$ GeV^4. The solid line indicates the minimum line, the dashed one the straight connection between the minima. h_1 and h_2 are given in units of GeV.

extreme cases, when m_h is small and $\xi \approx 1$ it can decrease down to about 0.2. Since the deviations of the estimate $\widetilde{V}_b$ from V_b can become large and the height of the potential barrier enters the computation of the bubble wall thickness we use V_b in our further calculations.

The different shapes of the potential along various paths in the field space are illustrated in fig. 5.6. The solid black curves correspond to the one of fig. 5.4 and to the solid line in fig. 5.5. The dashed blue curves show the potential along the dashed line of fig. 5.5. Note the deviation of the two barrier heights. If one minimizes the potential in θ instead of fixing the value θ_{brk} the difference is only marginal, see the dotted red curve in fig. 5.6a. The same holds for the red line in (b) for fixed θ_{brk} and minimized in the h_2 direction. But the potential rises steeply if $\theta = \theta_{\text{sym}}$ is held constant and does not develop a second minimum, see the dashed-dotted green curve in (a). A deviation from the constraint $h_2/h_1 = \tan(\beta_T)$ to $h_2/h_1 = 1$ results in a rise of the potential, but it still has a second minimum, cf. the green line in (b).

Let us close the discussion with two graphs, fig. 5.7, showing the dependence of h_2 and θ along the minimum line parameterized by h_1. The field h_2 roughly equals h_1 and at least in the broken minimum the deviation from $h_2/h_1 = 1$ is small so that we can assume $\tan(\beta_T) \approx 1$. The phase θ changes smoothly from θ_{sym} to θ_{brk}. The
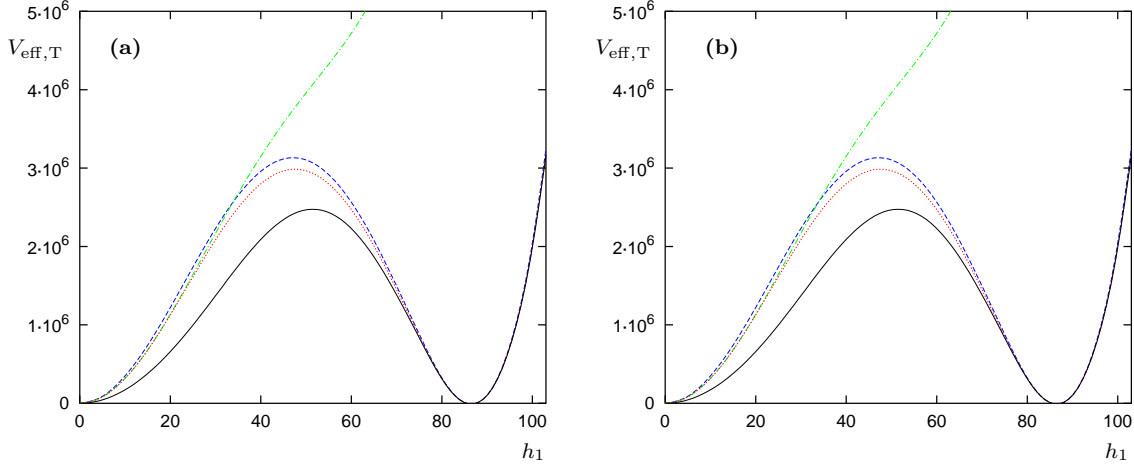
Figure 5.6: $V_{\text{eff,T}}$ (in GeV^4) in dependence of h_1 (in GeV) along the minimum line (solid black), along $h_2 = \tan(\beta_T)h_1$ and $\theta = \theta_{\text{brk}}$ (dashed blue) and for $h_2 = \tan(\beta_T)h_1$ and minimized in the θ-direction (a, dotted red), $h_2 = \tan(\beta_T)h_1$ and $\theta = \theta_{\text{sym}}$ (a, dashed-dotted green) and for $\theta = \theta_{\text{brk}}$, minimized in the h_2-direction (b, dotted red), $\theta = \theta_{\text{brk}}$ and $h_2 = h_1$ (b, dashed-dotted green).
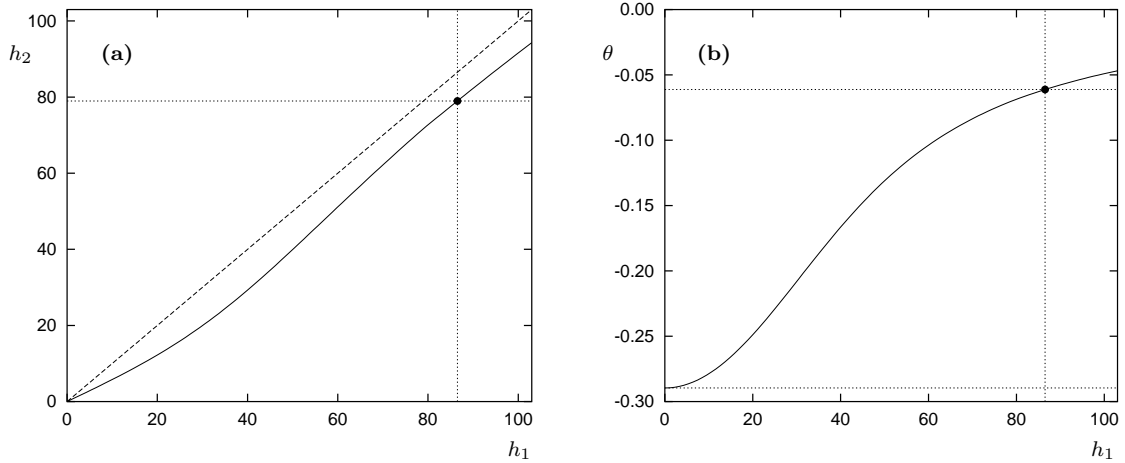
Figure 5.7: The fields h_2 (a) and θ (b) in dependence of h_1 along the minimum line (in units of GeV). h_1 changes from 0 at the symmetric to 86.5 GeV at the broken minimum, h_2 from 0 to 79.0 GeV and θ from -0.290 to -0.061. The diagonal line in (a) indicates the direction $h_1 = h_2$.

easiest, but quite appropriate way to approximate this curve is to use a tanh-profile. We will return to this topic and treat it in more detail in section 5.7. The presented example is a typical representative for almost the whole parameter region analyzed. Some difficulties occur for $m_h \gtrsim 200$ GeV or for large values of α and small heavy Higgs masses, as we discuss below.

5.5 The strength of the phase transition

The constraint on the strength of the phase transition due to the washout criterion (2.34) is $\xi \gtrsim 1$.[1] The strength depends basically on the Higgs masses and falls off with decreasing m_H or increasing m_h. Thus the washout criterion sets a lower limit on m_H and an upper limit on m_h. On the other hand the experimental results for the search of a light neutral Higgs boson require $m_h \gtrsim 115$ GeV. Keeping in mind these boundaries we analyze the parameter space for two values of μ_3^2, i.e. $\mu_3^2 = 10000$ and 20000 GeV^2, and for three different CP-phases, $\alpha = 0.0001$ as the limit of vanishing phase as well as $\alpha = 0.2$ and 0.4. We perform these analyses each with m_h varying form 115 to 190 GeV in steps of 5 GeV and tune m_H in steps of one to five GeV for each given m_h. In order to explore the observables we are interested in, e.g. the strength ξ, as functions of m_H we connect the measured data with spline interpolations. We extend the range for the light Higgs mass only up to 190 GeV because for larger values the effective potential (5.54) gets a complex part. Then the field dependent squared heavy Higgs masses, which also depend implicitly on m_h, become negative for small h_1 or h_2 and the bosonic distribution function in the thermal contribution (5.46) has an imaginary argument. Since we will show that the requirements for baryogenesis and the achievement of the measured baryon asymmetry can be fulfilled in the range 115 GeV $\leq m_h \leq$ 190 GeV we restrict the analysis to this interval.

Beside the first order phase transition, whose properties were illustrated in the previous section, for some parameter combinations the effective potential develops two non-trivial minima and a two-stage transition takes place. For high temperatures $V_{\mathrm{eff,T}}$ has only one, i.e. the symmetric minimum. With decreasing temperature the global minimum at $h_1 = h_2 = 0$ moves continuously away from the symmetric phase and a second local broken minimum develops. The Higgs fields get first non-zero expectation values via a second order phase transition. Then, with further decreasing temperature the second local broken minimum becomes the global one, which induces a tunneling process driven by a first order transition. Such a case is shown in fig. 5.8 for the parameters $\mu_3^2 = 10000$ GeV^2, $\alpha = 0.4$, $m_h = 125$ GeV and $m_H = 324$ GeV. We find that the occurrence of a two-stage transition depends

---

[1]Since the sphaleron energy in the 2HDM is of the same order of magnitude as in the SM [102] we still require $\xi \gtrsim 1$ for the washout criterion.

on the phase α. Among the three values 0.0001, 0.2 and 0.4 for α we observe this behavior only for the largest one. An analysis of this special case in the 2HDM was performed by Land and Carlson in ref. [103]. They found that the second transition can be strongly of first order under certain conditions. However, in the parameter region, which we analyze, the PT turns out to be too weak and therefore we exclude such cases from our analysis and focus on a pure first order phase transition. Moreover in the parameter region which is relevant for a generation of the observed baryon asymmetry, i.e. a small phase α as we will see, a two-stage transition does not occur.

Fig. 5.9 summarizes the dependence of the strength ξ of the input parameters. Together with lines of constant ξ also lines of constant wall thickness L_{w} are shown whose computation will be discussed in the next section. The strength varies from $\xi = 1.0$ up to $\xi \approx 2.5$. The upper limit of the m_H-range shown and accordingly the upper ξ-limit result from the constraint $|\delta\lambda_3/\lambda_3| \leq 0.5$, which is marked with the dashed red lines. The ratio $|\delta\lambda_3/\lambda_3|$ decreases down to about $0.2 - 0.3$ in the presented region for small heavy Higgs masses.

The mass m_H as a function of m_h for constant values of ξ grows nearly linear in the plotted regions. The slope increases for larger ξ. We do not in general explore the behavior of ξ beyond the m_H-intervals presented because then the one-loop corrections to the λ_i become too large and also the wall thickness becomes too small. But as an example we enlarged the mass range for the parameter set of fig. 5.9a and $m_h = 130$ GeV. At $m_H \approx 480$ GeV the non-trivial minimum remains higher than
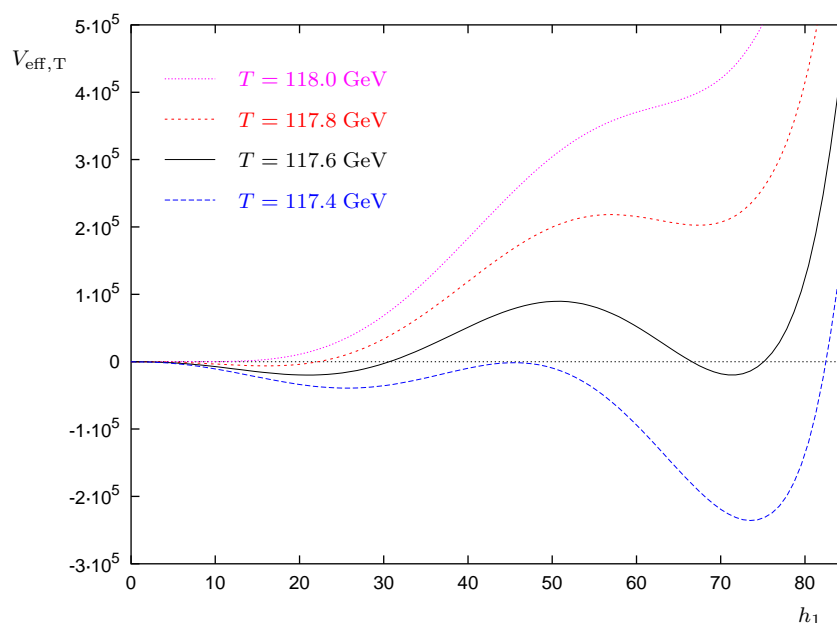

Figure 5.8: The effective potential (in units of GeV^4) versus h_1 (in GeV) for four different temperatures and the parameter set $\mu_3^2 = 10000$ GeV^2, $\alpha = 0.4$, $m_h = 125$ GeV, $m_H = 324$ GeV.
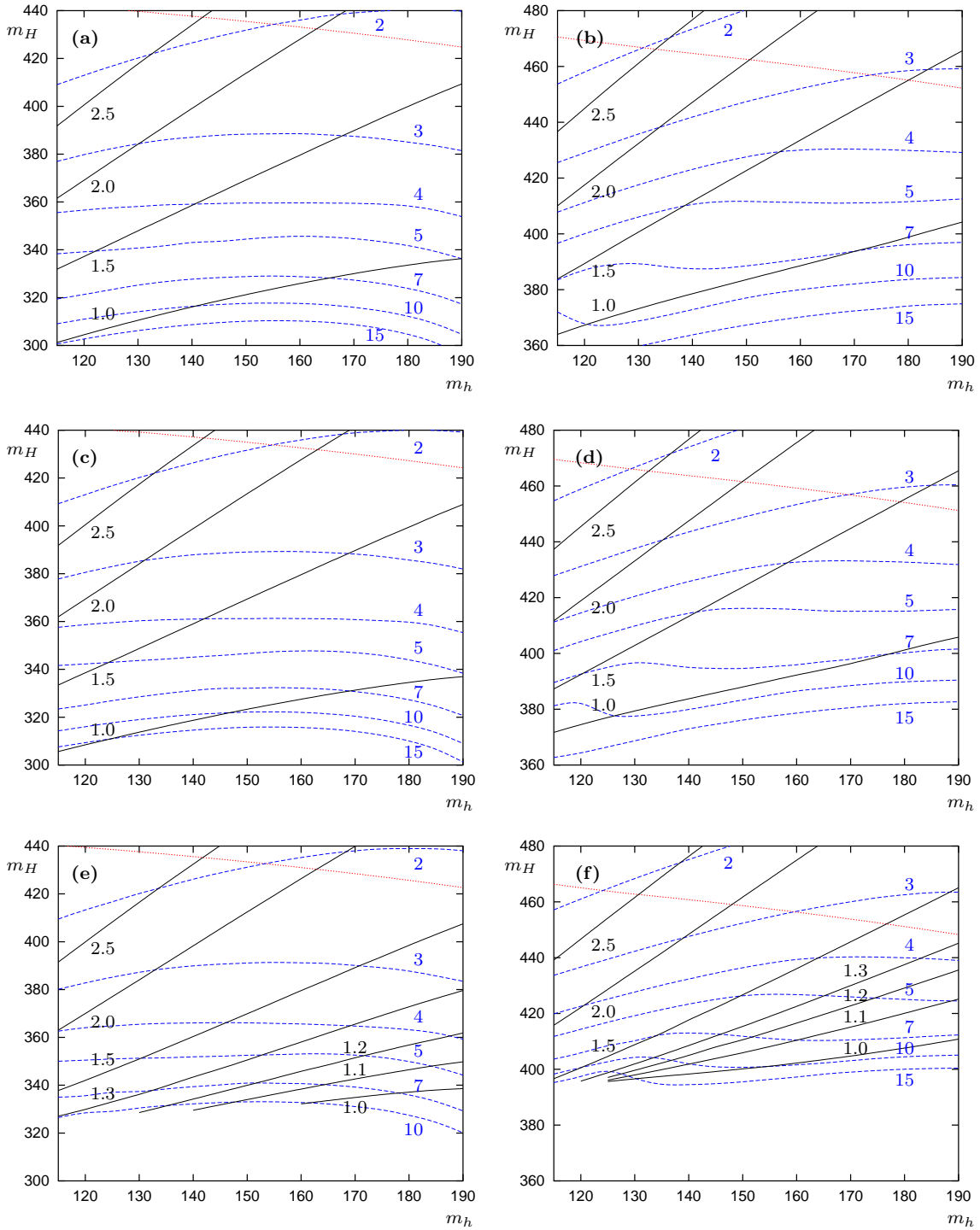
Figure 5.9: Lines of constant ξ (solid black) and $L_{\mathrm{w}} \cdot T_c$ (dashed blue) in dependence of m_h and m_H (in GeV). In the left column we take $\mu_3^2 = 10000 \,\mathrm{GeV}^2$ and in the right $\mu_3^2 = 20000 \,\mathrm{GeV}^2$. The rows represent top down $\alpha = 0.0001,\ 0.2,$ and 0.4. The dotted red lines mark the upper bound $|\delta\lambda_3/\lambda_3| = 0.5$.
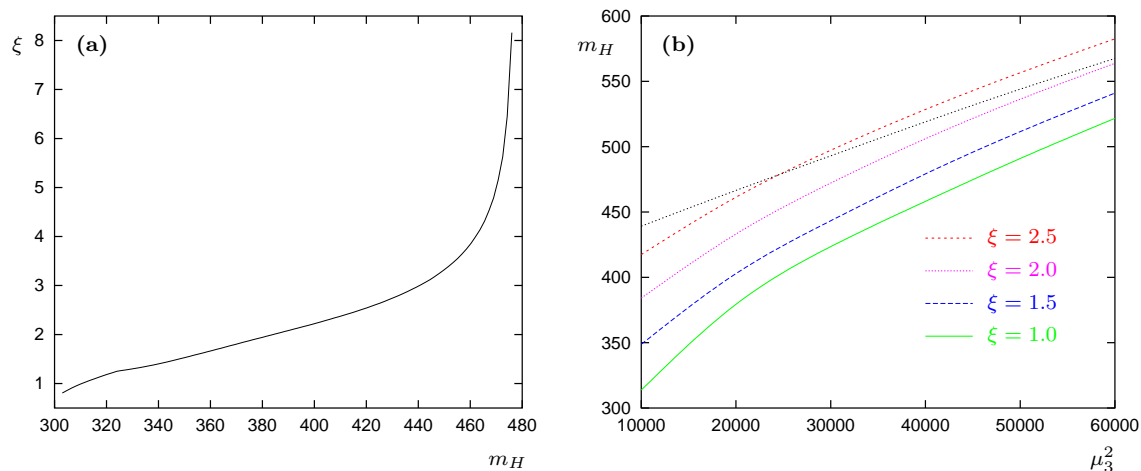
Figure 5.10: (a) ξ versus m_H for $\mu_3^2 = 10000\,\text{GeV}^2$, $\alpha = 0.0001$, and $m_h = 130$ GeV.
           (b) m_H versus μ_3^2 for $m_h = 130$ GeV, $\alpha = 0.2$ and fixed ξ. The dotted black line marks the limit $|\delta\lambda_3/\lambda_3| = 0.5$.

the symmetric one even at zero temperature and no phase transition takes place. Here we reach the limit of the wrong global minimum. The dependence of ξ on m_H is shown in fig. 5.10a for this example.

As already mentioned above, in the case of $\alpha = 0.4$ the first order phase transition changes in certain regions with decreasing m_H into a two-stage transition before one reaches $\xi = 1.0$. This limits slightly the acceptable mass region in fig. 5.9e. Beside the truncation of the ξ-lines for $\alpha = 0.4$ in general the phase has a small effect on the strength ξ. The lines of constant ξ differ in their slopes. The largest effect occurs for small ξ and for small m_H and m_h. At $\xi = 2$ the variations in mass amount only to a few GeV. In addition the changes are more distinct for $\mu_3^2 = 20000$ than $10000\,\text{GeV}^2$.

Let us now discuss the influence of μ_3^2 on the phase transition properties. The corresponding left and right plots in fig. 5.9 look quite similar, but note the different m_H-scales. With increasing μ_3^2 the lines of constant ξ are shifted to larger masses. Moreover the plotted mass interval shrinks from 140 to 120 GeV. In order to analyze this dependence in more detail we enlarged the μ_3^2-range up to $60000\,\text{GeV}^2$ for one example at $\alpha = 0.2$ and $m_h = 130$ GeV. The m_H-interval where ξ varies between 1.0 and 2.5 moves from about [315 GeV : 415 GeV] to [520 GeV : 580 GeV] while μ_3^2 changes from 10000 to $60000\,\text{GeV}^2$. Thus, the extent contracts from 100 to 60 GeV, and larger μ_3^2 leads to a smaller baryogenesis-allowed parameter space. Moreover the condition $|\delta\lambda_i/\lambda_i| \leq 0.5$ shrinks the interval by an additional 10 GeV at $\mu_3^2 = 60000\,\text{GeV}^2$. This behavior is illustrated in fig. 5.10b.

We close the discussion of this section with a short review to the recent literature dealing with the electroweak phase transition in the two-Higgs-doublet model. Cline and Lemieux [31] restricted to the case of a purely real μ_3^2 coupling, but they implemented several improvements in comparison to earlier studies. For example they did

not limit the mass over temperature range to the high temperature expansion. They used a similar treatment as in our work but connected the high and low T-ranges with the step function Θ rather than a smooth interpolation. Moreover they used different methods of ring summation for the bosonic thermal loop contributions, which we do not take into account, since the largest contributions arise from the heavy Higgs bosons and the effect of ring summation should be small. Indeed, we are in quite good agreement with their lines of constant $\xi = 1$ for the parameter sets $\mu_3^2 = 30000$ and 60000 GeV^2, as we have checked. In contrast to a work of Davies et al. [29] they also found that the strength ξ does not necessarily grow with increasing μ_3^2, which we can confirm with our studies. In ref. [29] a statistical approach was adopted by analyzing the phase transition for randomly selected parameter combinations, including also complex μ_3^2. Since Davies et al. chose the heavy Higgs masses not necessarily degenerate and the mass range was only investigated up to about 300 GeV, this does not match with our analysis and a direct comparison is not possible.

5.6 The wall thickness

For the computation of the baryon asymmetry the wall profile of the expanding Higgs bubbles has to be known. In principle one has to solve the field equation (2.35) for the different Higgs fields. We found in the previous chapter that for the φ^6 model the wall profile can be described adequately with a tanh-curve. Solving the field equations is associated with great effort and we do not expect a significant improvement compared with the tanh-profile. Thus we use the same estimate (2.50) as for the φ^6 model and compute the wall thickness by means of the potential barrier height

$$L_{\mathrm{w}} = \sqrt{\frac{v_c^2}{8V_b}}. \tag{5.60}$$

The shape of the bubble wall, parameterized with

$$h = \sqrt{2}\sqrt{h_1^2 + h_2^2}, \tag{5.61}$$

is modeled by the function

$$h(z) = \frac{v_c}{2}\left(1 - \tanh\frac{z}{L_{\mathrm{w}}}\right), \tag{5.62}$$

which approaches the broken limit $h = v_c$ for $z \to -\infty$ and the symmetric one $h = 0$ for $z \to +\infty$.

The wall thickness in units of T_c^{-1} varies in the analyzed parameter space of fig. 5.9 between about 2 and 15. In general L_{w} decreases for increasing heavy Higgs masses
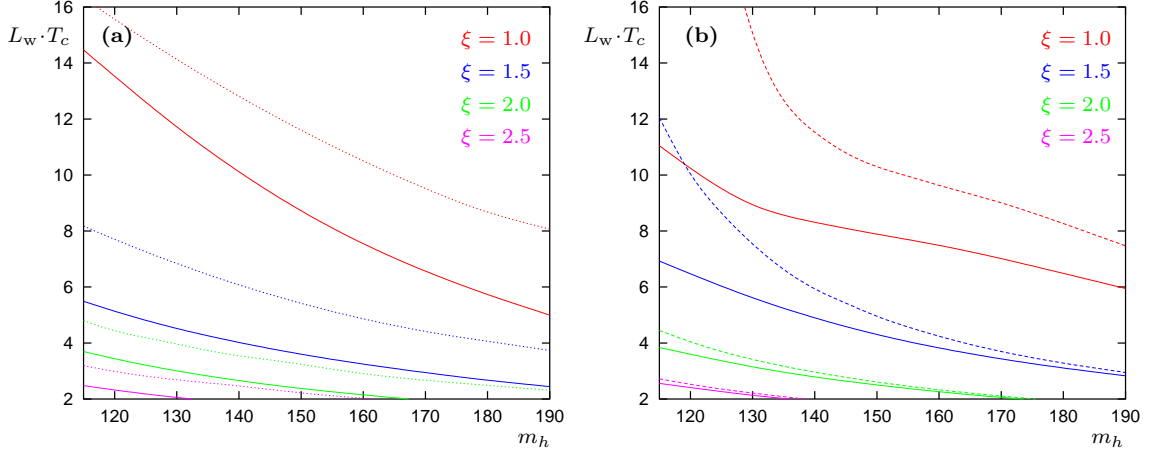
Figure 5.11: The wall thickness versus m_h (in GeV) for fixed ξ at $\mu_3^2 = 10000 \text{ GeV}^2$, $\alpha = 0.0001$ (a, solid lines) compared with the φ^6 model (a, dotted) and for $\mu_3^2 = 20000 \text{ GeV}^2$, $\alpha = 0.0001$ (b, solid) compared with $\mu_3^2 = 20000 \text{ GeV}^2$, $\alpha = 0.4$ (b, dashed).

while the dependence on the light mass is weaker. In the case of $\mu_3^2 = 10000 \text{ GeV}^2$ the lines of constant L_w are functions of m_h with uniform curvature. They rise and then fall off with increasing m_h. At larger μ_3^2 this behavior is similar in a wide parameter range, but in the lower left corners of figs. 5.9b,d,f one notices some fluctuations. These originate from the height of the potential barrier. Normally the square root of V_b, which enters the computation of L_w, increases nearly linear as a function of m_H for fixed μ_3^2, α and m_h. In the regions of small Higgs masses the barrier height shows a deviation form this behavior and exhibits an additional gain, which results in the mentioned fluctuations. Anyway, the estimate for the wall thickness gets worse for larger L_w because of the thin wall approximation, which we use for its computation. However, our aim is not a high precision calculation, but to find a region of the parameter space that fulfills the requirements for electroweak baryogenesis and for which we are able to reach the right order of magnitude of the measured baryon asymmetry of the universe.

Let us now connect the wall thickness to the strength of the phase transition as was already done for the φ^6 model in the previous chapter. Fig. 5.11 shows lines of constant ξ in the L_w-m_h-plane for different parameter sets, which corresponds to fig. 4.8 of the φ^6 model. Part (a) compares the combination $\mu_3^2 = 10000 \text{ GeV}^2$, $\alpha = 0.0001$ (solid lines) with the results of the φ^6 model (dotted lines). The shapes of the curves are similar, but the wall thickness is for this example in general smaller than that for the φ^6 model at corresponding values of ξ. In the 2HDM the wall thickness at constant ξ depends of course also on the parameters μ_3^2 and α. L_w increases, especially for small ξ, with increasing phase α, as is illustrated in part (b) of fig. 5.11. In this graph we take $\mu_3^2 = 20000 \text{ GeV}^2$, and $\alpha = 0.0001$ (solid lines) is compared with $\alpha = 0.4$ (dashed lines). L_w is even more enhanced for small

light Higgs masses than for larger ones. This effect is also visible in the graphs of fig. 5.9. Varying μ_3^2 affects the correlation of ξ and L_w also mostly for small values of ξ. The effect of increasing μ_3^2 on the lines of constant ξ is a shift to larger L_w in combination with a decrease for small m_H as well as an enhancement for large m_H. All changes are moderate for $\xi \gtrsim 2$ and more significant for $\xi \lesssim 1.5$.

5.7 CP-violation

As already mentioned CP-violation is one of the necessary conditions from Sakhorov for any baryogenesis szenario. In the two-Higgs-doublet model sufficiently large CP-violation enters via a complex coupling in the potential. This results in a complex fermion mass. Consider a single fermion, e.g. the top quark in our case, which acquires its mass through the coupling to the Higgs doublet Φ_2. The free Dirac equation then reads

$$(i\gamma^\mu \partial_\mu - MP_L - M^*P_R)\Psi = 0. \tag{5.63}$$

When the particle passes through the bubble wall during the phase transition its mass becomes space-time dependent since the Higgs field expectation value changes. Following the arguments we already used for the φ^6 model we boost into the rest frame of the bubble wall and assume a plane wall. Then the Higgs field and the top mass are only z-dependent. With our parameterization (5.13) of the neutral Higgs component we find for the top mass the relation

$$M(z) = y_\mathrm{t} h_2\, e^{i\theta(z)/2} = m(z)\, e^{i\theta(z)/2}. \tag{5.64}$$

Note that the space dependence of the phase is essential for the contribution to the CP-violation since a constant θ could be absorbed by a redefinition of the fermion field.

In order to deal with analytic expressions in the computation of the baryon asymmetry, which is shown in detail in ref. [79], we approximate both functions $m(z)$ and $\theta(z)$ with a tanh-profile. According to the wall profile modeled by eq. (5.62) the modulus $m(z)$ is given by

$$m(z) = y_\mathrm{t} \frac{h(z)}{\sqrt{2}} \sin \beta_T \approx y_\mathrm{t} \frac{h(z)}{2} \tag{5.65}$$

where we have used the fact that the angle β_T between the fields h_1 and h_2 stays roughly constant at $\pi/4$.

In an analogous way we treat the phase $\theta(z)$. We already argued at the end of section 5.5 that the variation of θ along the minimum line from the symmetric to the broken minimum can be described with a tanh-curve. We set for the θ-profile

$$\theta(z) = \theta_\mathrm{brk} - \frac{\Delta\theta}{2} \left(1 + \tanh \frac{z}{L_\mathrm{w}}\right) \tag{5.66}$$
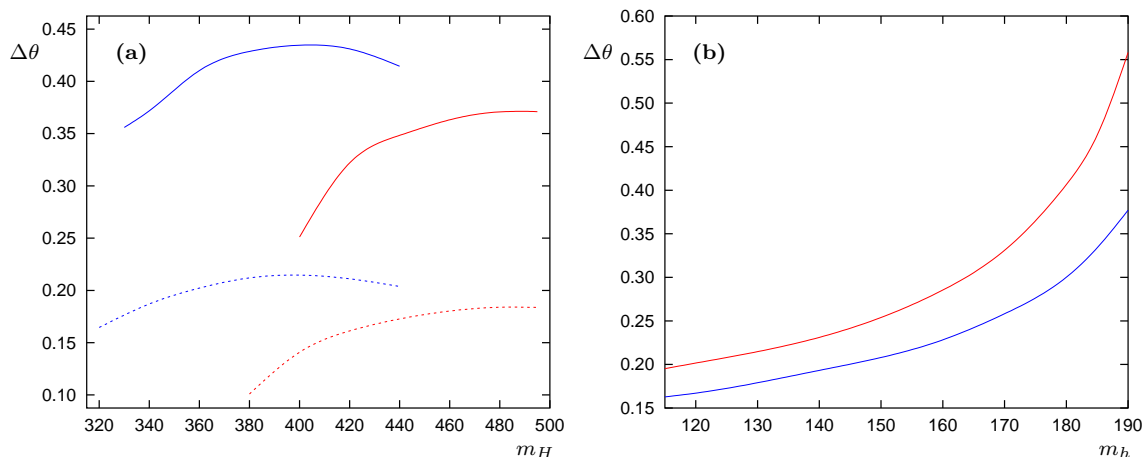
Figure 5.12: (a) The change $\Delta\theta$ versus m_H for $m_h = 130$ GeV and the combinations: $\mu_3^2 = 10000$ (blue) and 20000 GeV^2 (red), $\alpha = 0.2$ (dashed) and 0.4 (solid).

(b) $\Delta\theta$ versus m_h at $\mu_3^2 = 10000$ GeV^2, $\alpha = 0.2$ and $m_H = 330$ (blue) and 400 GeV (red).

where

$$\Delta\theta = \theta_{\text{brk}} - \theta_{\text{sym}} \tag{5.67}$$

so that θ approaches θ_{brk} for $z \to -\infty$ and θ_{sym} for $z \to +\infty$.[2] Since the derivative of $\theta(z)$ enters the source terms in the Boltzmann equations when the baryon asymmetry is computed, a large value of $\Delta\theta$ increases the baryon asymmetry [79].

In the following we discuss the dependence of $\Delta\theta$ on the input parameters, which is a measure for the *CP*-violation and enters the computation of the baryon asymmetry. As a representative example fig. 5.12a shows $\Delta\theta$ as a function of m_H for the sets $\mu_3^2 = 10000$ and 20000 GeV^2 combined with $\alpha = 0.2$ and 0.4 at fixed $m_h = 130$ GeV. The function $\Delta\theta(m_H)$ increases, reaches a maximum and falls off again. With regard to the particular m_H-interval, which corresponds to the ξ-range we are interested in, the maximum is shifted to larger masses while we raise μ_3^2. In the case of $\mu_3^2 = 20000$ GeV^2 it is already located just at the upper limit of the interval shown. By further increasing μ_3^2 one would solely observe the rising part of the curve, which in addition gets steeper and steeper. Moreover the average $\Delta\theta$ in the interval considered decreases. In comparison with the modulus μ_3^2 the phase α has a more significant influence on $\Delta\theta$. As can be seen from the figure the quantity $\Delta\theta$ approximately doubles if α is tuned form 0.2 to 0.4, except for small values of m_H. Here it increases with a factor less than two. But in general one observes the expected behavior that $\Delta\theta$ as a measure of *CP*-violation scales roughly linearly with α. In order to discuss finally the dependence on the light Higgs mass we show in fig. 5.12b the function $\Delta\theta(m_h)$ for $\mu_3^2 = 10000$ GeV^2 and $\alpha = 0.2$. We take as an example $m_H = 330$ GeV, which corresponds to the lower end of the curve in plot

---

[2]Note that $\theta(z)$ defined in ref. [79] corresponds to $\theta(z)/2$ in our notation.

(a), as well as $m_H = 400$ GeV, which represents the maximum. One finds that $\Delta\theta$ strongly depends on m_h. It increases with rising slope and covers a wide $\Delta\theta$-range in the presented interval. In conclusion large Higgs masses and a large phase α are favorable to baryogenesis.

5.8 Electric dipole moments

A brief introduction to electric dipole moments (EDMs) was already given in section 4.5. We will now focus on the relevance of EDMs to the 2HDM where additional CP-violation is caused by a non-zero phase α. In this model dipole moments arise due to scalar-pseudoscalar mixing in the neutral Higgs sector. The contributions can be computed in terms of the parameters $\mathrm{Im}(Z)$, which measure the degree of CP-non-conservation and which are the imaginary parts of the Higgs field normalization constants. They are related to the neutral Higgs propagators in the following way [104]:

$$\frac{1}{\langle\bar{\Phi}_1^0\rangle\langle\Phi_2^0\rangle}\langle\bar{\Phi}_1^0\Phi_2^0\rangle_q \;=\; \sum_i \frac{\sqrt{2}G_F}{q^2 + M_i^2} Z_{0i},$$

$$\frac{1}{\langle\Phi_1^0\rangle\langle\Phi_2^0\rangle}\langle\Phi_1^0\Phi_2^0\rangle_q \;=\; \sum_i \frac{\sqrt{2}G_F}{q^2 + M_i^2} \widetilde{Z}_{0i},$$

$$\frac{1}{\langle\Phi_1^0\rangle\langle\Phi_1^0\rangle}\langle\Phi_1^0\Phi_1^0\rangle_q \;=\; \sum_i \frac{\sqrt{2}G_F}{q^2 + M_i^2} Z_{1i},$$

$$\frac{1}{\langle\Phi_2^0\rangle\langle\Phi_2^0\rangle}\langle\Phi_2^0\Phi_2^0\rangle_q \;=\; \sum_i \frac{\sqrt{2}G_F}{q^2 + M_i^2} Z_{2i} \tag{5.68}$$

where M_i^2 are the eigenvalues of the neutral mass matrix M_n^2, see eq. (A.10), and

$$G_F = \frac{1}{2\sqrt{2}\left(|\langle\Phi_1^0\rangle|^2 + |\langle\Phi_2^0\rangle|^2\right)} \tag{5.69}$$

is the Fermi coupling constant. The notation $\langle\chi\eta\rangle_q$ for two scalar fields χ and η is an abbreviation for [104]

$$\langle\chi\eta\rangle_q = \int \mathrm{d}^4x \; \langle T[\chi(x)\eta(x)]\rangle_{\mathrm{vac}} \, e^{-iqx}. \tag{5.70}$$

The several CP-violating parameters

$$\mathrm{Im}(Z_{0i}), \quad \mathrm{Im}(\widetilde{Z}_{0i}), \quad \mathrm{Im}(Z_{1i}), \quad \mathrm{Im}(Z_{2i}), \tag{5.71}$$

which enter the calculation of the EDMs, can be expressed in terms of components of the Higgs mass matrix eigenvectors. This computation is shown in detail in appendix B.1. The Goldstone bosons do not contribute to these factors since the corresponding Z's are purely real. Thus, the sum can be restricted to the three massive neutral bosons. Note that the parameters respect the sum rules [104]

$$\sum_i \mathrm{Im}(Z_{0i}) = \sum_i \mathrm{Im}(\widetilde{Z}_{0i}) = \sum_i \mathrm{Im}(Z_{1i}) = \sum_i \mathrm{Im}(Z_{2i}) = 0, \qquad (5.72)$$

which means that the CP-violation vanishes if the masses of the neutral Higgs bosons are degenerate.

Electron EDM

In the 2HDM the dominant contributions to the electron EDM are two-loop amplitudes which were computed by Barr and Zee in 1990 [95]. They showed that the effect is significantly enhanced with respect to the standard one-loop contribution [105]. Further loop-diagrams including the W-boson were taken into account in investigations of Gunion and Vega [106], Chang et al. [107] as well as Leigh et al. [108]. In this work we follow the results of Chang et al. ignoring some minor corrections discussed in ref. [108]. The relevant loops and their calculations are listed in appendix B.2. For the electron EDM we finally end up with the sum of eqs. (B.12)–(B.17)

$$\begin{aligned} d_{\mathrm{e}}/e &= (d_{\mathrm{e}}/e)^{H\gamma\gamma}_{t-\mathrm{loop}} + (d_{\mathrm{e}}/e)^{HZ\gamma}_{t-\mathrm{loop}} + (d_{\mathrm{e}}/e)^{H\gamma\gamma}_{W-\mathrm{loop}} \\ &\quad + (d_{\mathrm{e}}/e)^{HZ\gamma}_{W-\mathrm{loop}} + (d_{\mathrm{e}}/e)^{H\gamma\gamma}_{G-\mathrm{loop}} + (d_{\mathrm{e}}/e)^{HZ\gamma}_{G-\mathrm{loop}}. \end{aligned} \qquad (5.73)$$

Now we discuss its relevance for the 2HDM. We found that in the parameter region analyzed the value of d_{e} is about five to thirty times smaller than the experimental limit of $1.6 \cdot 10^{-27}\, e\,\mathrm{cm}$ [91]. Thus, no additional constraints emerge to the parameters. On the other hand the present sensitivity of experiments does not suffice to confirm or rule out our scenario.

Let us focus on the importance of the different contributions to d_{e} and on the dependence of d_{e} on the input parameters. Since an EDM arises due to CP-violation we expect a larger value for an increasing CP-phase α. Indeed we find that d_{e} approximately doubles if we change α from 0.2 to 0.4. As an example some values are listed in table 5.2 for four parameter sets. Here we compare $\mu_3^2 = 10000$ and $20000\ \mathrm{GeV}^2$ and $\alpha = 0.2$ and 0.4 for median Higgs masses, which in each case correspond to a strength $\xi \approx 1.2 - 1.3$. Also raising μ_3^2 enhances d_{e}. Concerning the single contributions to d_{e} the largest ones originate from the top- and W-loop with $(d_{\mathrm{e}})_{W-\mathrm{loop}} > 0$ whereas $(d_{\mathrm{e}})_{t-\mathrm{loop}} < 0$. The absolute value of $(d_{\mathrm{e}})_{t-\mathrm{loop}}$ is somewhat smaller, but of the same order of magnitude as $(d_{\mathrm{e}})_{W-\mathrm{loop}}$. Consequently the sum is about a factor $5 - 10$ smaller than the single values and is then of the same order of magnitude as

μ_3^2	α	m_h	m_H	d_e	$(d_e)_{t-\mathrm{loop}}$	$(d_e)_{W-\mathrm{loop}}$	$(d_e)_{G-\mathrm{loop}}$
10000	0.2	150	350	0.075	-0.233	0.269	0.040
20000	0.2	150	410	0.107	-0.336	0.381	0.063
10000	0.4	150	350	0.149	-0.462	0.533	0.078
20000	0.4	150	410	0.212	-0.668	0.758	0.122

Table 5.2: The electron EDM and the single contributions from the top-, W- and Higgs-loop for different parameter sets. Mass units are GeV, the EDMs are given in units of $10^{-27}\, e\,\mathrm{cm}$.

the Goldstone-loop contribution. Thus, all three parts are decisive for the electron EDM. We observe this behavior in the whole parameter region analyzed. We also investigate the dependence of d_e on the Higgs masses. Both for increasing m_h and m_H the value of d_e decreases. We find that the larger μ_3^2 gets the weaker is the dependence on the heavy Higgs mass. This tendency becomes apparent in fig. 5.13 where we compare lines of constant electron and neutron EDMs in the m_h-m_H-plane. The latter is discussed in more detail below. The plots (a)-(d) of fig. 5.13 correspond to the graphs (c)-(f) of fig. 5.9, i.e. we take $\mu_3^2 = 10000$ and $20000\ \mathrm{GeV}^2$ in the left and right column, respectivly, as well as $\alpha = 0.2$ in the upper and 0.4 in the lower row. The slopes of the curves shown become even steeper for further increasing μ_3^2, which case is not shown in this figure, but tested up to $\mu_3^2 = 60000\ \mathrm{GeV}^2$. Here d_e is rather independent of m_H, at least in the parameter region which satisfies the requirements for electroweak baryogenesis.

Neutron EDM

In the Standard Model the neutron EDM is very small and far away from the reach of an experimental discovery. Beginning with proposals of Weinberg [109] there have been various calculations, which pointed out that sizeable contributions from previously ignored terms can arise in models with CP-violation in the Higgs sector, such as the 2HDM. See e.g. ref. [96] for a recent overview. Weinberg took into account a three-gluon-operator of the form [109]

$$\mathcal{O}_g = \frac{1}{3} w f^{abc} G^a_{\mu\nu} \widetilde{G}^{\nu\beta,b} G^{\mu,c}_{\beta} \qquad (5.74)$$

where $G^a_{\mu\nu}$ is the gluon field strength tensor and $\widetilde{G}^{\mu\nu,a} = 1/2\, \varepsilon^{\mu\nu\rho\sigma} G^a_{\rho\sigma}$. We will also test its influence for our model. Barr and Zee considered two-loop graphs related to the EDMs of the constituent quarks of the neutron [95]. Gunion and Wyler showed that the dominant contribution comes from the color EDMs (CEDM) $\widetilde{d}_q$ ($q = \mathrm{u, d}$) of the light quarks [110] where the photon lines in the graphs considered by Barr and Zee are replaced by gluon lines. The corresponding operator reads
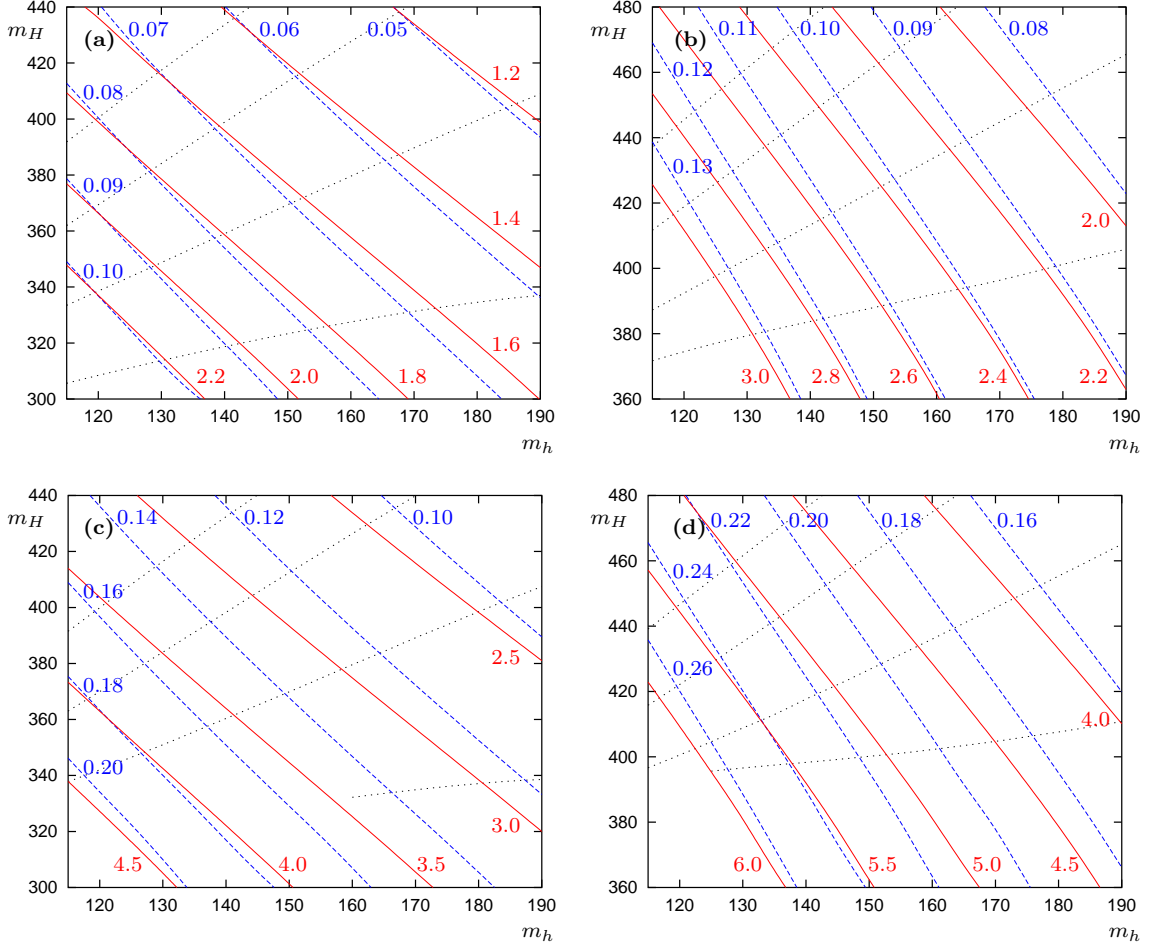
Figure 5.13: Contours of constant electron (dashed blue) and neutron (solid red) EDMs. d_{e} is given in units of $10^{-27}\,e\,\mathrm{cm}$, d_{n} in $10^{-26}\,e\,\mathrm{cm}$, masses in GeV. The parameter sets of plots (a)-(d) correspond to those of (c)-(f) in fig. 5.9. For orientation lines of constant ξ (top down: $\xi = 2.5$, 2.0, 1.5, 1.0) are dotted.

$$\mathcal{O}_{gq} = -\frac{i}{2}\widetilde{d}_q g_s \bar{\psi}_q \sigma_{\mu\nu} G^{\mu\nu} \gamma_5 \psi_q = \frac{1}{2}\widetilde{d}_q g_s \bar{\psi}_q \sigma_{\mu\nu} \widetilde{G}^{\mu\nu} \psi_q \tag{5.75}$$

with $q = \mathrm{u}, \mathrm{d}$. The computation of the CEDMs $\widetilde{d}_{\mathrm{u}}$ and $\widetilde{d}_{\mathrm{d}}$ as well as that of the three-gluon contribution w is presented in appendix B.3. The sum of these three values, according to eq. (B.25), yields the neutron EDM d_{n}.

In contrast to the electron electric dipole moment the one of the neutron does not lie below its experimental bound of $3.0 \cdot 10^{-26}\,e\,\mathrm{cm}$ [90] in all of our parameter region, as can be seen in fig. 5.13. In the case $\alpha = 0.4$ roughly half of the parameter region shown is excluded for $\mu_3^2 = 10000\,\mathrm{GeV}^2$ and the whole region for $\mu_3^2 = 20000\,\mathrm{GeV}^2$. However, note that d_{n} has quite a large error, about 50%, as pointed out in appendix B.3. Due to the large error band there arises actually no constraint as long as one

μ_3^2	α	m_h	m_H	d_{n}	$d_{\mathrm{n}}(\widetilde{d}_{\mathrm{u}})$	$d_{\mathrm{n}}(\widetilde{d}_{\mathrm{d}})$	$|d_{\mathrm{n}}(w)|$
10000	0.2	150	350	1.76	0.38	1.36	0.020
20000	0.2	150	410	2.53	0.56	1.95	0.031
10000	0.4	150	350	3.48	0.76	2.68	0.040
20000	0.4	150	410	5.03	1.10	3.88	0.062

Table 5.3: Examples for the neutron EDM and the single contributions from the CEDMs of up- and down quarks and from Weinberg's operator. Masses are given in units of GeV, the EDMs in units of $10^{-26}\, e\,\mathrm{cm}$.

restricts to $\mu_3^2 \lesssim 20000\,\mathrm{GeV}^2$ and $\alpha \lesssim 0.4$. For larger values of μ_3^2 or α the neutron EDM of course increases and exceeds the measured bound in a wide mass range.

The dependence of the neutron EDM on the input parameters is quite similar to that of the electron one. The lines of constant d_{n} run approximately parallel to those of d_{e} in the m_h-m_H-plane, the slope is just a little bit flatter. We also find roughly a doubling for a change in α from 0.2 to 0.4. In table 5.3 the results for d_{n} and its single contributions from the up and down quark CEDMs and from Weinberg's operator are listed for the same four examples as discussed in the electron case. The dominant contribution arises from the color EDM of the down quark, which is about a factor 3.5 larger than the one due to the up quark CEDM. The part $|d_{\mathrm{n}}(w)|$ arising from the three-gluon-operator is roughly an order 1% correction and could therefore be neglected. The examples of table 5.3 and the behavior discussed are typical for the analyzed parameter space. In summary it can be ascertained that both the electron and neutron electric dipole moments lie below the experimental limits in a wide parameter range of the model under consideration. The value of d_{e} is about one order of magnitude below the measured constraint and due to the large error in the theoretical determination of d_{n} it also does not definitely exceed the bound set by experiments.

Let us very briefly mention further experimental electroweak constraints, e.g. the ρ parameter. The statement $\rho \approx 1$ translates to the requirement of nearly degenerate heavy Higgs masses, which is fulfilled in our treatment. In addition $\tan\beta = 1$ prevents large deviation from Standard Model physics. Explicit formulae and detailed discussions can be found for instance in refs. [111–115].

5.9 The baryon asymmetry in the 2HDM

At the end of this chapter we will consider the baryon asymmetry which is predicted for given input parameters in the two-Higgs-doublet model. As in the case of the

φ^6 model we do not perform a detailed analysis, but discuss briefly the results of ref. [79]. The transport equations, which have to be solved are almost the same as in the φ^6 model because the same particles are taken into account. Eqs. (4.49)-(4.51) as well as eqs. (4.53)-(4.55), which refer to the particle types t, b and t^c, apply also to the 2HDM. A difference arises in the Higgs sector. Since this model contains two Higgs doublets we have to double the Higgs degrees of freedom. Thus, the corresponding transport equations read

$$4v_{\rm w}K_{1,h}\mu'_{h,2} + 4u'_{h,2} - 3\Gamma_y(\mu_{t,2} + \mu_{b,2} + 2\mu_{t^c,2} + 2\mu_{h,2}) - 4\Gamma_h\mu_{h,2} \;=\; 0 \qquad (5.76)$$

$$-4K_{4,h}\mu'_{h,2} + 4v_{\rm w}\tilde{K}_{5,h}u'_{h,2} + 4\Gamma_h^{\rm tot}u_{h,2} \;=\; 0. \qquad (5.77)$$

The latter one is only a multiple of eq. (4.56) because the source term on the r.h.s. vanishes. In the first equation the factor in front of the top Yukawa rate is not doubled since only one Higgs doublet couples to the top quark. The interaction rates and diffusion constants are also adopted from the φ^6 model as given by eqs. (4.48). For a given set of input parameters we first compute all relevant quantities, which enter the transport equations, such as ξ, $\tan\beta_T$, $L_{\rm w}$, $\theta_{\rm sym}$ and $\theta_{\rm brk}$, which have been extensively discussed in this chapter. The numerically derived solutions of the coupled set of Boltzmann equations enter eqs. (3.33) and (3.34), which gives us finally the baryon asymmetry in the model under consideration. Again, the wall velocity is treated as a free parameter. In general, η_B depends only mildly on $v_{\rm w}$ [79].

As an example we present in fig. 5.14 contours of constant baryon asymmetry in the m_h-m_H-plane for the parameter set $\mu_3^2 = 10000 \text{ GeV}^2$ and $\alpha = 0.2$. The wall velocity was fixed to $v_{\rm w} = 0.1$ in this plot. For orientation we also show the line $\xi = 1$. The mass region below that line is excluded since the phase transition is not strong enough. The baryon asymmetry increases for a stronger PT or accordingly for larger heavy Higgs masses. The dependence on the light mass is less pronounced. The observed value $\eta_B = (8.7 \pm 0.3)\cdot 10^{-11}$ can be reached in this example for heavy Higgs masses between 320 and 330 GeV. The light Higgs mass can be tuned up to about 160 GeV. Since η_B is nearly proportional to the CP-phase α [79] the measured asymmetry can easily be explained for larger masses m_H if one decreases α. Taking for instance $\alpha = 0.1$ the allowed heavy Higgs masses range is shifted to $330 - 340$ GeV and the light mass can be chosen up to about 190 GeV.

If we compare fig. 5.14 with fig. 5.13a, which shows the EDMs in the corresponding parameter set, we can use the baryon asymmetry to predict the EDMs. They are largest for small Higgs masses m_h and m_H. Taking $m_h = 115$ GeV and $\xi = 1$ the observed value of η_B is reached for $\alpha \approx 0.8$, assuming a linear dependence. In this case we find a neutron EDM of about $9\cdot 10^{-26}\,e$ cm, using again a proportional scaling of $d_{\rm n}$ in dependence of α, which we found in the previous section. Thus, the neutron EDM is a factor of three larger than the experimental bound. Concerning the theoretical uncertainties the experimental upper limit on $d_{\rm n}$ starts to cut into the parameter space. An improvement of an order of magnitude offers the possibility
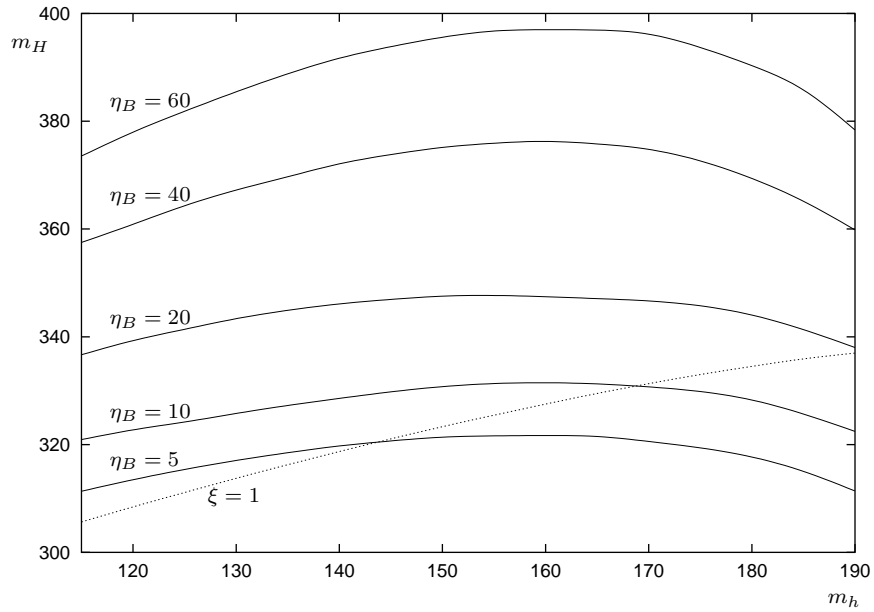
Figure 5.14: Contours of constant η_B in the m_h-m_H-plane for the parameter set $\mu_3^2 = 10000 \text{ GeV}^2$ and $\alpha = 0.2$. The Higgs masses are given in units of GeV, η_B in units of 10^{-11}. The (ξ=1)-line is also shown for orientation.

to probe a larger part of the parameter space. The electron EDM does not exceed the current limit in the region analyzed. As in the φ^6 model we also find in the two-Higgs-doublet model a wide parameter range which can explain the observed baryon asymmetry without being in conflict with experimental constraints.

Chapter 6

Summary

We analyzed the phase structure, especially with regard to the strength of a first order electroweak phase transition, in two different extensions of the Standard Model. We had to consider beyond the Standard Model (BSM) physics since we wanted to realize electroweak baryogenesis, which is not possible in the Standard Model. We focused on the extended Standard Model with a dimension-six Higgs operator and the two-Higgs-doublet model. Motivated by the opportunity to measure the mass of the Higgs boson or BSM Higgs particles in the near future at collider experiments we asked whether the measured baryon asymmetry of the universe can be explained within these models. We used the one-loop effective potential in order to estimate the strength of the phase transition in dependence of the respective model parameters. In addition the bubble wall profiles were approximated, which led in combination with the strength of the PT to a determination of the parameter range which fulfills the requirements for electroweak baryogenesis. The possible parameter space is further restricted by the experimental bounds on the electron and neutron EDMs, which must not be exceeded.

After reviewing the derivation of the effective potential as well as some general aspects concerning the EWPT and the electroweak baryogenesis in chapters 2 and 3 we paid attention to the Standard Model with a dimension-six Higgs operator in chapter 4.
This model was parameterized by the Higgs mass m_h and the cut-off scale Λ. For the effective potential we took at zero-temperature the top quark one-loop contribution into account. The thermal part we approximated with the high-temperature expansion including the weak gauge, the Higgs and the Goldstone bosons as well as the top quark. It turned out that the cubic, the logarithmic term and the one-loop term due to the dimension-six Higgs operator give a $\mathcal{O}(10\%)$ contribution to the strength of the phase transition, whereas the effects of the Higgs two-loop-contribution and a dimension-eight operator are negligible. We found a strong first order phase transition, i.e. $\xi \geq 1$, for Higgs masses up to $m_h = 200$ GeV. In this case the scale Λ has to be around 400 GeV. For an intermediate Higgs mass of 160 GeV a range of

400 GeV $\lesssim \Lambda \lesssim$ 550 GeV is compatible with a strong first order PT. If the Higgs mass is lowered down to the experimental bound of 115 GeV, Λ can be chosen in the range between 600 and 800 GeV. In general, the PT becomes stronger for decreasing m_h and Λ. The quartic coupling in the potential is negative and stabilized by the φ^6 interaction in almost all of the parameter space satifying $\xi \geq 1$.

Beside the strength of the PT we considered some properties of the nucleating bubbles using for this purpose the thin wall approximation. The nucleation temperature T_n was estimated, which differs only slightly from the critical temperature T_c for phase transitions with $\xi \approx 1$, but reaches a deviation of $\mathcal{O}(10\%)$ for $\xi \approx 2.5$. Since we computed the wall thickness at $T = T_c$ instead of $T = T_n$ the approximation starts to break down for large values of ξ. The wall profile was computed on one hand by solving numerically the equation of motion in the thin wall limit and on the other hand using a simple tanh-function. The different methods coincided well and we found wall thicknesses between three (roughly at $\xi \approx 2.5$) and $8 - 16$ times T_c^{-1} (at $\xi \approx 1$, depending on Λ). The wall velocity we treated as a free parameter. In conclusion a wide parameter range for Higgs masses well above 115 GeV meets the requirements of electroweak baryogenesis.

Assuming maximal CP-violation in the top quark phase we estimated also the electron and neutron EDMs in this model. They are both at least one order of magnitude below the experimental bounds. Stronger constraints on this model may arise from forthcoming experiments.

Finally we presented the results of ref. [79] for the baryon asymmetry as a function of the model parameters. The baryon asymmetry η_B was computed in the WKB approximation, expanding in derivatives of the background Higgs field. We found a range of approximately $5 \cdot 10^{-12} \lesssim \eta_B \lesssim 1 \cdot 10^{-9}$ which is compatible to $1 \lesssim \xi \lesssim 2.5$ and $L_\mathrm{w} \gtrsim 3\,T_c^{-1}$. The latter requirement is necessary for the validity of the WKB ansatz. We predicted a correlation between the Higgs mass and the cut-off scale Λ such that the measured baryon asymmetry is achieved. For $m_h = 115$ GeV one needs $\Lambda \approx 730$ GeV, down to $\Lambda \approx 410$ GeV for $m_h = 200$ GeV. The strength of the phase transition varies along this line between about 1.0 and 1.7, the wall thickness is around 6 or $7\,T_c^{-1}$, a range in which our approximations can be regared as valid. Future high energy experiment, e.g. at the LHC, will be able to detect a Higgs boson with a mass of the order of some hundred GeV and to test new physics at the cut-off scale. It would be interesting for further investigations to study the impact of other higher dimesional operators, which we neglected, on electroweak measurements in order to have additional testable constraints on this model.

In chapter 5 we performed a corresponding analysis for the two-Higgs-doublet model. We did not use the most general potential, but followed the common choice $\mu_1^2 = \mu_2^2$ and $\lambda_1 = \lambda_2$, i.e. $\tan\beta = 1$, and restricted the investigation to the case of degenerate heavy Higgs masses. We implemented explicit CP-violation due to a complex coupling $\mu_3^2 e^{i\alpha}$ in the potential. The model was described by the light and the heavy Higgs mass, m_h and m_H, respectively, as well as the parameters μ_3^2 and α. We had

to set up a renormalization procedure in order to express the couplings in terms of our input parameters also at one-loop level, which could not be realized analytically like in the φ^6 model.

We took into account the zero-temperature contribution to the effective potential from the heavy Higgs bosons and the top quark. At finite temperature we included additionally the weak gauge bosons. Since the mass over temperature range exceeds the area of validity of the high temperature expansion, we used the high and low temperature expansions with a smooth interpolation in-between. We parameterized the potential with the neutral fields h_1 and h_2 and with a phase θ.

The phase transition properties were analyzed for different discrete sets of μ_3^2 and α, each in dependence of the Higgs masses. Since the effective potential becomes complex for $m_h \gtrsim 190$ GeV we restricted the mass range to smaller values, for which we also found a strong first order phase transition. It gets stronger for increasing heavy or decreasing light Higgs mass. The dependence on the phase α is weak and μ_3^2 shifts the heavy Higgs mass range, in which the PT is strong and the wall thickness satisfies $L_{\mathrm{w}} T_c \gtrsim 3$. The latter was approximated with the same method as used in the φ^6 model. The width of the bubble wall decreases while m_H gets larger. We also computed the profile of the phase between the two Higgs expectation values, which changes between the broken and the symmetric phase. The varying phase leads to a CP-violating source term for the top quark, which contributes to the generation of the baryon asymmetry.

The CP-violation also gives rise to non-vanishing electric dipole moments, which we estimated in this model for the electron and neutron. The EDMs are approximately proportional to the phase α and they decrease for larger masses, both m_h and m_H, or smaller μ_3^2. Thus, the experimental bound on the neutron EDM limits the range of α and μ_3^2.

We finally computed the baryon asymmetry η_B in the 2HDM as a function of the model parameters. Again the WKB approximation was applied also to this model in order to derive the transport equations, which were solved numerically. The baryon asymmetry depends only weakly on the light Higgs mass and rises for increasing heavy mass. It turned out that η_B also scales proportionally to α. With the experimentally measured value of η_B we could predict the EDMs in terms of the Higgs masses. Since beside the masses also the coupling μ_3^2 and the phase α are unknown we computed for the case $\mu_3^2 = 10000\,\mathrm{GeV}^2$ an upper limit for the neutron EDM, which exceeds the experimental bound by roughly a factor three. However, for a wide parameter range this model is not in conflict with the EDM constrains.

For further studies it would be interesting to extend the analysis to a wider parameter range, e.g. including the case $\tan \beta > 1$, and to derive more definite relations between the baryon asymmetry and the model parameters. Forthcoming collider experiments, like the LHC, will probably detect at least the light Higgs boson. Maybe also heavy bosons will be observed, which will reduce the number of unknown degrees of freedom. Perhaps at a future $e^+ e^-$ collider the Higgs self-coupling will be measured.

In conclusion we were able to show that both models, the Standard Model with a dimension-six Higgs operator and the two-Higgs-doublet model, satisfy in natural parameter regions the requirements for electroweak baryogenesis. The dependences of the strength of the phase transition and the bubble wall thickness on the Higgs mass are comparable in both cases. Prospects for the experimental discovery of the Higgs boson or BSM physics and their impact on the theories considered motivate more detailed investigations in the future.

Appendix A

Higgs Masses in the 2HDM

Here we compute the Higgs masses in the 2HDM with CP-violation. At first we parameterize the Higgs doublets via eight real fields $\varphi_1, \ldots, \varphi_8$

$$\Phi_1 = \begin{pmatrix} \varphi_1 + i\,\varphi_2 \\ \varphi_5 + i\,\varphi_6 \end{pmatrix} \quad \text{and} \quad \Phi_2 = \begin{pmatrix} \varphi_3 + i\,\varphi_4 \\ \varphi_7 + i\,\varphi_8 \end{pmatrix}. \tag{A.1}$$

The VEV is expressed in polar coordinates

$$\left\langle \Phi_1^0 \right\rangle = h\,e^{-i\theta_0/2} \quad \text{and} \quad \left\langle \Phi_2^0 \right\rangle = h\,e^{i\theta_0/2}. \tag{A.2}$$

The charged part of the mass matrix

$$(M_c^2)_{ij} = \frac{1}{2}\,\left.\frac{\partial^2 V}{\partial \varphi_i \partial \varphi_j}\right|_{\text{VEV}}, \quad i,j = 1,\ldots,4 \tag{A.3}$$

gives a symmetric matrix with the components

$$\begin{aligned}
(M_c^2)_{11} = (M_c^2)_{22} = (M_c^2)_{33} = (M_c^2)_{44} &= -\mu_1^2 + (\lambda_1 + \lambda_3)h^2, \\
(M_c^2)_{12} = (M_c^2)_{34} &= 0, \\
(M_c^2)_{13} = (M_c^2)_{24} &= -\mu_3^2 \cos\alpha + (\lambda_4 + \lambda_5)\cos\theta_0\,h^2, \\
-(M_c^2)_{14} = (M_c^2)_{23} &= -\mu_3^2 \sin\alpha - (\lambda_4 - \lambda_5)\sin\theta_0\,h^2. \quad \text{(A.4)}
\end{aligned}$$

The eigenvalues can be easily computed. One obtains quite a short form by expressing λ_4 and μ_3^2 in terms of the other parameters. For this purpose we use the minimum equations (5.15) and (5.16), which give us

$$\begin{aligned}
\lambda_4 &= \frac{\mu_1^2}{h^2} - \lambda_1 - \lambda_3 - \lambda_5[\cos(2\theta_0) - \cot(\theta_0 + \alpha)\sin(2\theta_0)], \\
\mu_3^2 &= \lambda_5 \csc(\theta_0 + \alpha)\sin(2\theta_0)h^2. \tag{A.5}
\end{aligned}$$

Then we find for the squared masses of the charged Goldstone and Higgs bosons

$$\begin{aligned}
m_{G^\pm}^2 &= 0, \\
m_{H^\pm}^2 &= -2\mu_1^2 + 2(\lambda_1 + \lambda_3)h^2. \tag{A.6}
\end{aligned}$$

In the neutral sector it is useful to use Cartesian instead of polar coordinates for the VEV

$$\left\langle \Phi_1^0 \right\rangle = a + ib \quad \text{and} \quad \left\langle \Phi_2^0 \right\rangle = a - ib. \tag{A.7}$$

With these variables the minimum conditions read

$$\begin{aligned} -\mu_1^2 + b^2(\lambda_1 + \lambda_3 + \lambda_4 - 3\lambda_5) + a^2(\lambda_1 + \lambda_3 + \lambda_4 + \lambda_5) & \\ -\frac{\mu_3^2}{a}(a\cos\alpha - b\sin\alpha) &= 0, \\ -\mu_1^2 + a^2(\lambda_1 + \lambda_3 + \lambda_4 - 3\lambda_5) + b^2(\lambda_1 + \lambda_3 + \lambda_4 + \lambda_5) & \\ +\frac{\mu_3^2}{b}(b\cos\alpha - a\sin\alpha) &= 0. \end{aligned} \tag{A.8}$$

The mass matrix of the neutral fields

$$(M_n^2)_{ij} = \frac{1}{2}\left.\frac{\partial^2 V}{\partial\varphi_i\partial\varphi_j}\right|_{\text{VEV}}, \quad i,j = 5,\ldots,8 \tag{A.9}$$

has the following structure

$$M_n^2 = \begin{pmatrix} A & C & E & D \\ C & B & -D & F \\ E & -D & A & -C \\ D & F & -C & B \end{pmatrix} \tag{A.10}$$

with

$$\begin{aligned} A &= -\mu_1^2 + b^2(\lambda_1 + \lambda_3 + \lambda_4 - \lambda_5) + a^2(3\lambda_1 + \lambda_3 + \lambda_4 + \lambda_5), \\ B &= -\mu_1^2 + a^2(\lambda_1 + \lambda_3 + \lambda_4 - \lambda_5) + b^2(3\lambda_1 + \lambda_3 + \lambda_4 + \lambda_5), \\ C &= 2ab(\lambda_1 - \lambda_5), \\ D &= -2ab(\lambda_3 + \lambda_4 - 2\lambda_5) + \mu_3^2\sin\alpha, \\ E &= -\mu_3^2\cos\alpha + 2a^2(\lambda_3 + \lambda_4 + \lambda_5) - 2b^2\lambda_5, \\ F &= -\mu_3^2\cos\alpha - 2b^2(\lambda_3 + \lambda_4 + \lambda_5) + 2a^2\lambda_5. \end{aligned} \tag{A.11}$$

The eigenvalues can be expressed analytically

$$\begin{aligned} m_{1,2}^2 &= \frac{1}{2}\Big(A + B - E + F \\ &\quad \pm\sqrt{(A + B - E + F)^2 - 4[(C + D)^2 + (A - E)(B + F)]}\Big), \\ m_{3,4}^2 &= \frac{1}{2}\Big(A + B + E - F \\ &\quad \pm\sqrt{(A + B + E - F)^2 + 4[(C + D)^2 - (A + E)(B - F)]}\Big). \tag{A.12} \end{aligned}$$

One can show by using the minimum conditions (A.8) that the term in squared brackets in the equation for $m_{1,2}^2$ vanishes. Thus, we can extract the root and we find $m_2^2 = 0$, which corresponds to the Goldstone boson, and

$$m_{H_2}^2 = m_1^2 = -2\mu_1^2 + 4\lambda_1 h^2, \tag{A.13}$$

after rewriting the Cartesian back into polar coordinates. In the limit $\alpha \to 0$ m_1^2 matches $m_{H^0}^2$, but for arbitrary α the neutral mass eigenstates are mixtures of CP states. Hence, we cannot assign an odd or even state to a given Higgs mass, and we just label the lightest Higgs with H_1 and the heavier neutral ones with H_2 and H_3. For the other two eigenvalues $m_{3,4}^2$ we also go back to h and θ_0. Moreover it is again useful to eliminate μ_3^2 and λ_4 in the root term by the use of eqs. (A.5) to derive

$$
\begin{aligned}
m_{H_3}^2 &= m_3^2 \\
&= -\mu_1^2 + 2(\lambda_1 + \lambda_3 + \lambda_4)h^2 + \sqrt{\mu_1^4 + 4\lambda_5 \cos(2\theta_0)\mu_1^2 h^2 + 4\lambda_5^2 h^4}, \\
m_{H_1}^2 &= m_4^2 \\
&= -\mu_1^2 + 2(\lambda_1 + \lambda_3 + \lambda_4)h^2 - \sqrt{\mu_1^4 + 4\lambda_5 \cos(2\theta_0)\mu_1^2 h^2 + 4\lambda_5^2 h^4}. \tag{A.14}
\end{aligned}
$$

If we consider the limit $\alpha \to 0$, we can relate $m_{H_3}^2$ to $m_{A^0}^2$ and $m_{H_1}^2$ to $m_{h^0}^2$.

Appendix B

Contributions to the EDMs

B.1 CP-violating parameters Im(Z)

We start from eqs. (5.68), which connect the four relevant CP-violating parameters to the neutral Higgs propagators. For their computation we first diagonalize the neutral mass matrix M_n^2, eq. (A.10), by an orthogonal transformation U given by the eigenvectors of M_n^2, i.e.

$$U\, M_n^2\, U^T = \text{diagonal}, \tag{B.1}$$

and express the neutral Higgs fields $\Phi_1^0 = 1/\sqrt{2}\,(a_1 + ib_1)$ and $\Phi_2^0 = 1/\sqrt{2}\,(a_2 + ib_2)$ in terms of mass eigenstates $(\phi_1, \phi_2, \phi_3, \phi_4)$,

$$\begin{pmatrix} a_1 \\ a_2 \\ b_1 \\ b_2 \end{pmatrix} = U^T \begin{pmatrix} \phi_1 \\ \phi_2 \\ \phi_3 \\ \phi_4 \end{pmatrix}. \tag{B.2}$$

For the propagators, which are real because of the reality of the fields, Lorentz invariance and translational invariance, we use the estimate [104]

$$\langle a_k a_l \rangle_q \simeq \sum_i \frac{U_{ki}^T U_{li}^T}{q^2 + M_i^2} \tag{B.3}$$

where $a_{k,l}$ stands for one of the fields a_1, a_2, b_1, b_2. Considering for example $\text{Im}(Z_{0i})$ where i indicates the neutral mass eigenstates this gives us the relation

$$\text{Im}\left[\frac{\langle \bar{\Phi}_1^0 \Phi_2^0 \rangle_q}{\langle \bar{\Phi}_1^0 \rangle \langle \Phi_2^0 \rangle}\right] = \text{Im}\left[\frac{1}{h_1 h_2} e^{-i(\theta_1 + \theta_2)} \frac{1}{2} \langle (a_1 - ib_1)(a_2 + ib_2) \rangle_q\right]$$

$$
\begin{aligned}
=\ & \frac{1}{2h_1 h_2} \Big\{ \cos(\theta_1 + \theta_2) \left(\langle a_1 b_2 \rangle_q - \langle a_2 b_1 \rangle_q \right) \\
& - \sin(\theta_1 + \theta_2) \left(\langle a_1 a_2 \rangle_q - \langle b_1 b_2 \rangle_q \right) \Big\} \\
=\ & \frac{1}{2h_1 h_2} \sum_i \frac{1}{q^2 + M_i^2} \Big\{ \cos(\theta_1 + \theta_2) \left(U_{1i}^T U_{4i}^T - U_{2i}^T U_{3i}^T \right) \\
& - \sin(\theta_1 + \theta_2) \left(U_{1i}^T U_{2i}^T + U_{3i}^T U_{4i}^T \right) \Big\}
\end{aligned}
\tag{B.4}
$$

where we have used $\langle \Phi_i^0 \rangle = h_i e^{\mp i\theta_i}$ for $i = 1, 2$, respectively, which corresponds to the notation of eq. (5.13). After replacing also in the Fermi constant (5.69) the Higgs expectation values by h_1 and h_2,

$$
G_F = \frac{1}{2\sqrt{2}(h_1^2 + h_2^2)},
\tag{B.5}
$$

the imaginary part of the r.h.s. of eq. (5.68) for $\mathrm{Im}(Z_{0i})$ then reads

$$
\mathrm{Im} \left[\sum_i \frac{\sqrt{2} G_F}{q^2 + M_i^2} (Z_{0i}) \right] = \sum_i \frac{1}{q^2 + M_i^2} \frac{\mathrm{Im} Z_{0i}}{2(h_1^2 + h_2^2)}.
\tag{B.6}
$$

Now a comparison of the coefficients corresponding to the different mass eigenstates in the equations (B.4) and (B.6) yields

$$
\begin{aligned}
\mathrm{Im}(Z_{0i}) =\ & \frac{h_1^2 + h_2^2}{h_1 h_2} \Big\{ \cos(\theta_1 + \theta_2) \left(U_{1i}^T U_{4i}^T - U_{2i}^T U_{3i}^T \right) \\
& - \sin(\theta_1 + \theta_2) \left(U_{1i}^T U_{2i}^T + U_{3i}^T U_{4i}^T \right) \Big\} \\
=\ & \frac{2}{\sin(2\beta)} \Big\{ \cos(\theta_1 + \theta_2) \left(U_{1i}^T U_{4i}^T - U_{2i}^T U_{3i}^T \right) \\
& - \sin(\theta_1 + \theta_2) \left(U_{1i}^T U_{2i}^T + U_{3i}^T U_{4i}^T \right) \Big\}.
\end{aligned}
\tag{B.7}
$$

In an analogous way we derive for the three remaining CP-violating parameters the relations

$$
\begin{aligned}
\mathrm{Im}(\widetilde{Z}_{0i}) =\ & \frac{2}{\sin 2\beta} \Big\{ \cos(\theta_1 - \theta_2) \left(U_{1i}^T U_{4i}^T + U_{2i}^T U_{3i}^T \right) \\
& + \sin(\theta_1 - \theta_2) \left(U_{1i}^T U_{2i}^T - U_{3i}^T U_{4i}^T \right) \Big\}, \\
\mathrm{Im}(Z_{1i}) =\ & \frac{1}{\cos^2 \beta} \Big\{ 2\cos(2\theta_1) U_{1i}^T U_{3i}^T + \sin(2\theta_1) \left(U_{1i}^T U_{1i}^T - U_{3i}^T U_{3i}^T \right) \Big\}, \\
\mathrm{Im}(Z_{2i}) =\ & \frac{1}{\sin^2 \beta} \Big\{ 2\cos(2\theta_2) U_{2i}^T U_{4i}^T - \sin(2\theta_2) \left(U_{2i}^T U_{2i}^T - U_{4i}^T U_{4i}^T \right) \Big\}.
\end{aligned}
\tag{B.8}
$$

B.2 The electron EDM

Following the results of ref. [107] we calculate the different contributions to the electron EDM in terms of the parameters $\text{Im}(Z_i)$, which we derived in the previous section. We first define a common factor

$$K = \frac{m_e \alpha_{em} \sqrt{2} G_F}{(4\pi)^3} \approx 0.6553 \times 10^{-27} \text{cm} \tag{B.9}$$

and the mass ratios

$$
\begin{aligned}
z_i^t &= \frac{m_t^2}{M_i^2}, \\
z_Z^t &= \frac{m_t^2}{m_Z^2}, \\
z_i^W &= \frac{m_W^2}{M_i^2}, \\
z_Z^W &= \frac{m_W^2}{m_Z^2}.
\end{aligned}
\tag{B.10}
$$

Moreover we need the loop functions

$$
\begin{aligned}
F(z) &= \frac{z}{2} \int_0^1 \mathrm{d}x \frac{1 - 2x(1-x)}{x(1-x) - z} \ln \frac{x(1-x)}{z}, \\
G(z) &= \frac{z}{2} \int_0^1 \mathrm{d}x \frac{1}{x(1-x) - z} \ln \frac{x(1-x)}{z}, \\
H(z) &= \frac{z}{2} \int_0^1 \mathrm{d}x \frac{1}{z - x(1-x)} \left(1 + \frac{z}{z - x(1-x)} \ln \frac{x(1-x)}{z} \right), \\
\widetilde{F}(z_1, z_2) &= \frac{z_2 F(z_1)}{z_2 - z_1} + \frac{z_1 F(z_2)}{z_1 - z_2}, \\
\widetilde{G}(z_1, z_2) &= \frac{z_2 G(z_1)}{z_2 - z_1} + \frac{z_1 G(z_2)}{z_1 - z_2}.
\end{aligned}
\tag{B.11}
$$

The following loops contribute to the electron EDM:

- top-loop, $H\gamma\gamma$-vertex

$$(d_e/e)_{t-\text{loop}}^{H\gamma\gamma} = -\frac{16}{3} K \sum_i \left[(F(z_i^t) + G(z_i^t))\text{Im}(Z_{0i}) - (F(z_i^t) - G(z_i^t))\text{Im}(\widetilde{Z}_{0i}) \right] \tag{B.12}$$

- top-loop, $HZ\gamma$-vertex

$$
\begin{aligned}
(d_{\mathrm{e}}/e)_{t-\mathrm{loop}}^{HZ\gamma} &= -\frac{(1-4\sin^2\theta_w)(3-8\sin^2\theta_w)}{6\sin^2\theta_w\cos^2\theta_w}K \\
&\quad \times \sum_i \Big[(\widetilde{F}(z_i^t, z_Z^t) + \widetilde{G}(z_i^t, z_Z^t))\mathrm{Im}(Z_{0i}) \\
&\qquad\quad - (\widetilde{F}(z_i^t, z_Z^t) - \widetilde{G}(z_i^t, z_Z^t))\mathrm{Im}(\widetilde{Z}_{0i}) \Big]
\end{aligned} \tag{B.13}
$$

- W-loop, $H\gamma\gamma$-vertex

$$
(d_{\mathrm{e}}/e)_{W-\mathrm{loop}}^{H\gamma\gamma} = 4K\sin^2\beta \sum_i \mathrm{Im}(Z_{0i}) \left[3F(z_i^W) + \frac{23}{4}G(z_i^W) + \frac{3}{4}H(z_i^W) \right] \tag{B.14}
$$

- W-loop, $HZ\gamma$-vertex

$$
\begin{aligned}
(d_{\mathrm{e}}/e)_{W-\mathrm{loop}}^{HZ\gamma} &= \frac{1-4\sin^2\theta_w}{\sin^2\theta_w}K\sin^2\beta \sum_i \mathrm{Im}(Z_{0i}) \left[\frac{5-\tan^2\theta_w}{2}\widetilde{F}(z_i^W, z_Z^W) \right. \\
&\quad \left. +\frac{7-3\tan^2\theta_w}{2}\widetilde{G}(z_i^W, z_Z^W) + \frac{3}{4}G(z_i^W) + \frac{3}{4}H(z_i^W) \right]
\end{aligned} \tag{B.15}
$$

- Goldstone-loop, $H\gamma\gamma$-vertex

$$
(d_{\mathrm{e}}/e)_{G-\mathrm{loop}}^{H\gamma\gamma} = 2K\sin^2\beta \sum_i \frac{\mathrm{Im}(Z_{0i})}{z_i^W} \left[F(z_i^W) - G(z_i^W) \right] \tag{B.16}
$$

- Goldstone-loop, $HZ\gamma$-vertex

$$
\begin{aligned}
(d_{\mathrm{e}}/e)_{G-\mathrm{loop}}^{HZ\gamma} &= \frac{1-4\sin^2\theta_w}{4\sin^2\theta_w}K\sin^2\beta \\
&\quad \times \sum_i \frac{\mathrm{Im}(Z_{0i})}{z_i^W}(1-\tan^2\theta_w) \left[\widetilde{F}(z_i^W, z_Z^W) - \widetilde{G}(z_i^W, z_Z^W) \right]
\end{aligned} \tag{B.17}
$$

Here we use for the weak mixing angle the numerical value $\theta_w = 0.5030$. The resulting electron EDM is the sum over the single contributions (B.12)–(B.17).

B.3 The neutron EDM

The dominant contributions to the neutron EDM are caused by two-loop calculations of the QCD corrected coefficients $\widetilde{d}_{\mathrm{u}}, \widetilde{d}_{\mathrm{d}}$ from the color electric dipole moments

(CEDM) [110, 116, 117], see eq. (5.75),

$$\widetilde{d}_{\mathrm{u}} = \frac{\sqrt{2}G_F m_u(\mu)}{128\pi^4}g_s^2(\mu)\left(\frac{g_s(m_t)}{g_s(\mu)}\right)^{\frac{74}{23}}\sum_i \left[F(z_i^t) + G(z_i^t)\right]\mathrm{Im}(Z_{2i}), \quad \text{(B.18)}$$

$$\widetilde{d}_{\mathrm{d}} = \frac{\sqrt{2}G_F m_d(\mu)}{128\pi^4}g_s^2(\mu)\left(\frac{g_s(m_t)}{g_s(\mu)}\right)^{\frac{74}{23}}$$
$$\times \sum_i \left[F(z_i^t)\tan^2\beta\,\mathrm{Im}(Z_{2i}) - G(z_i^t)\cot^2\beta\,\mathrm{Im}(Z_{1i})\right]. \quad \text{(B.19)}$$

Moreover we discuss the contribution w due to the Weinberg operator (5.74) [109, 116–118],

$$w = -\frac{\sqrt{2}G_F}{256\pi^4}g_s^3(\mu)\left(\frac{g_s(m_t)}{g_s(\mu)}\right)^{\frac{108}{23}}\sum_i H(z_i^t)\mathrm{Im}(Z_{2i}). \quad \text{(B.20)}$$

The loop functions F and G are defined in eqs. (B.11) and H is given by the expression [118]

$$H(z) = \frac{z^2}{4}\int_0^1 \mathrm{d}x \int_0^1 \mathrm{d}y \frac{x^3y^3(1-x)}{[zx(1-xy) + (1-x)(1-y)]^2}. \quad \text{(B.21)}$$

The energy scale μ is set to the nucleon mass scale, i.e. $\mu = 1$ GeV. The numerical values for the quark masses [117], the strong coupling [96] and the Fermi constant are

$$\begin{aligned}
m_u(\mu) &= 5.6 \text{ MeV}, \\
m_d(\mu) &= 9.9 \text{ MeV}, \\
g_s(\mu) &= 2.1, \\
g_s(m_t) &= 1.196, \\
G_F &= 2.30156 \cdot 10^{-22} \text{ cm/MeV}. \quad \text{(B.22)}
\end{aligned}$$

For the computation of the neutron EDM we use the results of ref. [96], which are based on QCD sum rule techniques. The contribution caused by the CEDMs of the constituent quarks then reads

$$(d_{\mathrm{n}}/e)(\widetilde{d}_{\mathrm{u}}, \widetilde{d}_{\mathrm{d}}) = (1 \pm 0.5)(0.55\widetilde{d}_{\mathrm{u}} + 1.1\widetilde{d}_{\mathrm{d}}) \quad \text{(B.23)}$$

and that for the Weinberg operator

$$|(d_{\mathrm{n}}/e)(w)| = 22 \text{ MeV } |w|. \quad \text{(B.24)}$$

Unfortunately the error of $(d_{\mathrm{n}}/e)(\widetilde{d}_{\mathrm{u}}, \widetilde{d}_{\mathrm{d}})$ is quite large, about 50%, and for $(d_{\mathrm{n}}/e)(w)$ only the absolute value can be determined. But the latter turns out to be merely an about 1% correction to the first one. We finally use for the total neutron EDM the estimate

$$d_{\mathrm{n}}/e = (d_{\mathrm{n}}/e)(\widetilde{d}_{\mathrm{u}}, \widetilde{d}_{\mathrm{d}}) + |(d_{\mathrm{n}}/e)(w)|. \quad \text{(B.25)}$$

Bibliography

[1] D. N. Spergel et al., *Wilkinson Microwave Anisotropy Probe (WMAP) Three Year Results: Implications for Cosmology*, arXiv:astro-ph/0603449.

[2] A. D. Sakharov, *Violation of CP Invariance, C Asymmetry, and Baryon Asymmetry of the Universe*, Pisma Zh. Eksp. Teor. Fiz. **5** (1967) 32 [JETP Lett. **5** (1967 SOPUA,34,392-393.1991 UFNAA,161,61-64.1991) 24].

[3] M. Yoshimura, *Unified Gauge Theories and the Baryon Number of the Universe*, Phys. Rev. Lett. **41** (1978) 281 [Erratum-ibid. **42** (1979) 746].

[4] S. Dimopoulos and L. Susskind, *On the Baryon Number of the Universe*, Phys. Rev. **D18** (1978) 4500.

[5] D. Toussaint, S. B. Treiman, F. Wilczek and A. Zee, *Matter - Antimatter Accounting, Thermodynamics, and Black Hole Radiation*, Phys. Rev. **D19** (1979) 1036.

[6] S. Weinberg, *Cosmological Production of Baryons*, Phys. Rev. Lett. **42** (1979) 850.

[7] M. Fukugita and T. Yanagida, *Baryogenesis without Grand Unification*, Phys. Lett. **B174** (1986) 45.

[8] W. Buchmüller and M. Plümacher, *Neutrino Masses and the Baryon Asymmetry*, Int. J. Mod. Phys. A **15** (2000) 5047 [arXiv:hep-ph/0007176].

[9] W. Buchmüller, *Some Aspects of Baryogenesis and Lepton Number Violation*, arXiv:hep-ph/0101102.

[10] T. Yanagida, *Horizontal Gauge Symmetry and Masses of Neutrinos*, Prog. Theor. Phys. **64** (1980) 1103.

[11] M. Gell-Mann, P. Ramond and R. Slansky, *Complex Spinors and Unified Theories*, Print-80-0576 (CERN)

[12] V. A. Kuzmin, V. A. Rubakov and M. E. Shaposhnikov, *On the Anomalous Electroweak Baryon Number Nonconservation in the Early Universe*, Phys. Lett. **B155** (1985) 36.

[13] K. Kajantie, M. Laine, K. Rummukainen and M. E. Shaposhnikov, *Is there a Hot Electroweak Phase Transition at m(H) ¿ approx. m(W)?*, Phys. Rev. Lett. **77** (1996) 2887 [arXiv:hep-ph/9605288].

[14] K. Kajantie, M. Laine, K. Rummukainen and M. E. Shaposhnikov, *A Non-Perturbative Analysis of the Finite T Phase Transition in SU(2) x U(1) Electroweak Theory*, Nucl. Phys. **B493** (1997) 413 [arXiv:hep-lat/9612006].

[15] F. Csikor, Z. Fodor and J. Heitger, *Endpoint of the Hot Electroweak Phase Transition*, Phys. Rev. Lett. **82** (1999) 21 [arXiv:hep-ph/9809291].

[16] Z. Fodor, J. Hein, K. Jansen, A. Jaster and I. Montvay, *Simulating the Electroweak Phase Transition in the SU(2) Higgs Model*, Nucl. Phys. **B439** (1995) 147 [arXiv:hep-lat/9409017].

[17] K. Kajantie, M. Laine, K. Rummukainen and M. E. Shaposhnikov, *The Electroweak Phase Transition: a Non-Perturbative Analysis*, Nucl. Phys. **B466** (1996) 189 [arXiv:hep-lat/9510020].

[18] W. Buchmuller, Z. Fodor and A. Hebecker, *Thermodynamics of the Electroweak Phase Transition*, Nucl. Phys. **B447** (1995) 317 [arXiv:hep-ph/9502321].

[19] LEP Collaborations, LEP Electroweak Working Group, SLD Electroweak Group and SLD Heavy Flavor Group, hep-ex/0312023.

[20] M. Trodden, *Electroweak Baryogenesis*, Rev. Mod. Phys. **71** (1999) 1463 [arXiv:hep-ph/9803479].

[21] X. Zhang, *Operator Analysis for the Higgs Potential and Cosmological Bound on the Higgs-Boson Mass*, Phys. Rev. **D47** (1993) 3065 [arXiv:hep-ph/9301277].

[22] S. W. Ham and S. K. Oh, *Electroweak Phase Transition in the Standard Model with a Dimension-Six Higgs Operator at One-Loop Level*, Phys. Rev. **D70** (2004) 093007 [arXiv:hep-ph/0408324].

[23] C. Grojean, G. Servant and J. D. Wells, *First-Order Electroweak Phase Transition in the Standard Model with a Low Cutoff*, Phys. Rev. **D71** (2005) 036001 [arXiv:hep-ph/0407019].

[24] A. I. Bochkarev, S. V. Kuzmin and M. E. Shaposhnikov, *Electroweak Baryogenesis and the Higgs Boson Mass Problem*, Phys. Lett. **B244** (1990) 275.

[25] A. G. Cohen, D. B. Kaplan and A. E. Nelson, *Spontaneous Baryogenesis at the Weak Phase Transition*, Phys. Lett. **B263** (1991) 86.

[26] A. E. Nelson, D. B. Kaplan and A. G. Cohen, *Why there is Something rather than Nothing: Matter from Weak Interactions*, Nucl. Phys. **B373** (1992) 453.

[27] N. Turok and J. Zadrozny, *Phase Transitions in the Two Doublet Model*, Nucl. Phys. **B369** (1992) 729.

[28] K. Funakubo, A. Kakuto and K. Takenaga, *The Effective Potential of Electroweak Theory with Two Massless Higgs Doublets at Finite Temperature*, Prog. Theor. Phys. **91** (1994) 341 [arXiv:hep-ph/9310267].

[29] A. T. Davies, C. D. Froggatt, G. Jenkins and R. G. Moorhouse, *Baryogenesis Constraints on Two Higgs Doublet Models*, Phys. Lett. **B336** (1994) 464.

[30] J. M. Cline, K. Kainulainen and A. P. Vischer, *Dynamics of Two Higgs Doublet CP Violation and Baryogenesis at the Electroweak Phase Transition*, Phys. Rev. **D54** (1996) 2451 [arXiv:hep-ph/9506284].

[31] J. M. Cline and P. A. Lemieux, *Electroweak Phase Transition in Two Higgs Doublet Models*, Phys. Rev. **D55** (1997) 3873 [arXiv:hep-ph/9609240].

[32] S. W. Ham and S. K. Oh, *Electroweak Phase Transition and Higgs Self-Couplings in the Two-Higgs-Doublet Model*, arXiv:hep-ph/0502116.

[33] E. W. Kolb and M. S. Turner, *The Early Universe*, Westview Press, 1994.

[34] P. W. Higgs, *Broken Symmetries, Massless Particles and Gauge Fields*, Phys. Lett. **12** (1964) 132.

[35] P. W. Higgs, *Broken Symmetries and the Masses of Gauge Bosons*, Phys. Rev. Lett. **13** (1964) 508.

[36] S. Coleman, *Aspects of Symmetry*, Cambridge University Press, 1988.

[37] P. Ramond, *Field Theory: A Modern Primer*, Addison-Wesley Publishing Company, 1989.

[38] M. Kaku, *Quantum Field Theory*, Oxford University Press, 1993.

[39] M. E. Peskin and D. V.Schroeder, *An Introduction to Quantum Field Theory*, Westview Press, 1995.

[40] T. Kugo, *Eichtheorie*, Springer Verlag Berlin Heidelberg, 1997.

[41] M. Quiros, *Finite Temperature Field Theory and Phase Transitions*, arXiv:hep-ph/9901312.

[42] S. Coleman and E. Weinberg, *Radiative Corrections as the Origin of Spontaneous Symmetry Breaking*, Phys. Rev. **D7** (1973) 1888.

[43] L. Dolan and R. Jackiw, *Symmetry Behavior at Finite Temperature*, Phys. Rev. **D9** (1974) 3320.

[44] P. Arnold and O. Espinosa, *The Effective Potential and First Order Phase Transitions: Beyond Leading-Order*, Phys. Rev. **D47** (1993) 3546 [Erratum-ibid. **D50** (1994) 6662] [arXiv:hep-ph/9212235].

[45] G. W. Anderson and L. J. Hall, *Electroweak Phase Transition and Baryogenesis*, Phys. Rev. **D45** (1992) 2685.

[46] M. E. Shaposhnikov, *Possible Appearance of the Baryon Asymmetry of the Universe in an Electroweak Theory*, JETP Lett. **44** (1986) 465 [Pisma Zh. Eksp. Teor. Fiz. **44** (1986) 364].

[47] G. D. Moore, *Measuring the Broken Phase Sphaleron Rate Nonperturbatively*, Phys. Rev. **D59** (1999) 014503 [arXiv:hep-ph/9805264].

[48] W. Buchmuller and O. Philipsen, *Magnetic Screening in the High Temperature Phase of the Standard Model*, Phys. Lett. **B397** (1997) 112 [arXiv:hep-ph/9612286].

[49] K. Rummukainen, M. Tsypin, K. Kajantie, M. Laine and M. E. Shaposhnikov, *The Universality Class of the Electroweak Theory*, Nucl. Phys. **B532** (1998) 283 [arXiv:hep-lat/9805013].

[50] Z. Fodor, *Electroweak Phase Transitions*, Nucl. Phys. Proc. Suppl. **83** (2000) 121 [arXiv:hep-lat/9909162].

[51] S. Coleman, *The Fate of the False Vacuum. 1. Semiclassical Theory*, Phys. Rev. **D15** (1977) 2929.

[52] A. D. Linde, *Decay of the False Vacuum at Finite Temperature*, Nucl. Phys. **B216** (1983) 421.

[53] A. D. Linde, *On the Vacuum Instability and the Higgs Meson Mass*, Phys. Lett. **B70** (1977) 306.

[54] A. D. Linde, *Fate of the False Vacuum at Finite Temperature: Theory and Applications*, Phys. Lett. **B100** (1981) 37.

[55] G. D. Moore, *Electroweak Bubble Wall Friction: Analytic Results*, JHEP **0003** (2000) 006 [arXiv:hep-ph/0001274].

[56] V. A. Rubakov and M. E. Shaposhnikov, *Electroweak Baryon Number Non-Conservation in the Early Universe and in High-Energy Collisions*, Usp. Fiz. Nauk **166** (1996) 493 [Phys. Usp. **39** (1996) 461] [arXiv:hep-ph/9603208].

[57] W. Bernreuther, *CP Violation and Baryogenesis*, Lect. Notes Phys. **591** (2002) 237 [arXiv:hep-ph/0205279].

[58] M. Kobayashi and T. Maskawa, *CP Violation in the Renormalizable Theory of Weak Interaction*, Prog. Theor. Phys. **49** (1973) 652.

[59] M. B. Gavela, P. Hernandez, J. Orloff, O. Pene, C. Quimbay, *Standard Model CP Violation and Baryon Asymmetry. Part 2: Finite Temperature*, Nucl. Phys. **B430** (1994) 382 [hep-ph/9406289].

[60] P. Huet, E. Sather, *Electroweak Baryogenesis and Standard Model CP Violation*, Phys. Rev. **D51** (1995) 379 [hep-ph/9404302].

[61] T. Konstandin, T. Prokopec and M. G. Schmidt, *Axial Currents from CKM Matrix CP Violation and Electroweak Baryogenesis*, Nucl. Phys. **B679** (2004) 246 [hep-ph/0309291].

[62] S. L. Adler, *Axial Vector Vertex in Spinor Electrodynamics*, Phys. Rev. **177** (1969) 2426.

[63] J. S. Bell and R. Jackiw, *A Pcac Puzzle: Pi0 → Gamma Gamma in the Sigma Model*, Nuovo Cim. **A60** (1969) 47.

[64] G. 't Hooft, *Symmetry Breaking through Bell-Jackiw Anomalies*, Phys. Rev. Lett. **37** (1976) 8.

[65] G. 't Hooft, *Computation of the Quantum Effects due to a Four-Dimensional Pseudoparticle*, Phys. Rev. **D14** (1976) 3432 [Erratum-ibid. **D18** (1978) 2199].

[66] N. S. Manton, *Topology in the Weinberg-Salam Theory*, Phys. Rev. **D28** (1983) 2019.

[67] F. R. Klinkhamer and N. S. Manton, *A Saddle Point Solution in the Weinberg-Salam Theory*, Phys. Rev. **D30** (1984) 2212.

[68] D. Bodeker, G. D. Moore and K. Rummukainen, *Chern-Simons Number Diffusion and Hard Thermal Loops on the Lattice*, Phys. Rev. **D61** (2000) 056003 [arXiv:hep-ph/9907545].

[69] G. D. Moore, *Sphaleron Rate in the Symmetric Electroweak Phase*, Phys. Rev. **D62** (2000) 085011 [arXiv:hep-ph/0001216].

[70] J. M. Cline, M. Joyce and K. Kainulainen, *Supersymmetric Electroweak Baryogenesis in the WKB Approximation*, Phys. Lett. **B417** (1998) 79 [Erratum-ibid. B **448** (1999) 321] [arXiv:hep-ph/9708393].

[71] J. M. Cline and K. Kainulainen, *A New Source for Electroweak Baryogenesis in the MSSM*, Phys. Rev. Lett. **85** (2000) 5519 [arXiv:hep-ph/0002272].

[72] J. M. Cline, M. Joyce and K. Kainulainen, *Supersymmetric Electroweak Baryogenesis*, JHEP **0007** (2000) 018 [arXiv:hep-ph/0006119].

[73] S. J. Huber and M. G. Schmidt, *SUSY Variants of the Electroweak Phase Transition*, Eur. Phys. J. **C10** (1999) 473 [arXiv:hep-ph/9809506].

[74] S. J. Huber and M. G. Schmidt, *Electroweak Baryogenesis: Concrete in a SUSY Model with a Gauge Singlet*, Nucl. Phys. **B606** (2001) 183 [arXiv:hep-ph/0003122].

[75] S. J. Huber, P. John and M. G. Schmidt, *Bubble Walls, CP Violation and Electroweak Baryogenesis in the MSSM*, Eur. Phys. J. **C20** (2001) 695 [arXiv:hep-ph/0101249].

[76] D. Bodeker, L. Fromme, S. J. Huber and M. Seniuch, *The Baryon Asymmetry in the Standard Model with a Low Cut-Off*, JHEP **0502** (2005) 026 [arXiv:hep-ph/0412366].

[77] L. Fromme and S. J. Huber, *Top Transport in Electroweak Baryogenesis*, arXiv:hep-ph/0604159.

[78] L. Fromme, S. J. Huber and M. Seniuch, *Baryogenesis in the Two-Higgs Doublet Model*, arXiv:hep-ph/0605242.

[79] L. Fromme, *Electroweak Baryogenesis in Extensions of the Standard Model*, PhD thesis, University of Bielefeld, 2006.

[80] T. Prokopec, M. G. Schmidt and S. Weinstock, *Transport Equations for Chiral Fermions to Order h-bar and Electroweak Earyogenesis. Part I*, Annals Phys. **314** (2004) 208 [arXiv:hep-ph/0312110].

[81] T. Prokopec, M. G. Schmidt and S. Weinstock, *Transport Equations for Chiral Fermions to Order h-bar and Electroweak Baryogenesis. Part II*, Annals Phys. **314** (2004) 267 [arXiv:hep-ph/0406140].

[82] X. Zhang, S. K. Lee, K. Whisnant, B.-L. Young, *Phenomenology of a Non-Standard Top Quark Yukawa Coupling*, Phys. Rev. **D50** (1994) 7042 [arXiv:hep-ph/9407259].

[83] E. M. Prucell and N. F. Ramsey, *On the Possibility of Electric Dipole Moments for Elementary Particles and Nuclei*, Phys. Rev. **78** (1950) 807.

[84] L. Landau and Zh. Eksperim, Teor. Fiz. **32** (1957) 405 [English transls.: Sov. Phys. - JETP**5** (1957) 336].

[85] L. Landau and Zh. Eksperim, *On the Conservation Laws for Weak Interactions*, Nucl. Phys. **3** (1957) 127.

[86] N. F. Ramsey, *Dipole Moments and Spin Rotations of the Neutron*, Phys. Rep. **43** (1978) 409.

[87] N. F. Ramsey, *Electric Dipole Moments of Particles*, Ann. Rev. Nucl. Part. Sci. **32** (1982) 211.

[88] C. S. Wu et al., *Experimental Test of Parity Conservation in Beta Decay*, Phys. Rev. **105** (1957) 1413.

[89] J. H. Christenson, J. W. Cronin, V. L. Fitch and R. Turlay, *Evidence for the 2 Pi Decay of the K(2)0 Meson*, Phys. Rev. Lett. **13** (1964) 138.

[90] C. A. Baker *et al.*, *An Improved Experimental Limit on the Electric Dipole Moment of the Neutron* arXiv:hep-ex/0602020.

[91] B. C. Regan, E. D. Commins, C. J. Schmidt and D. DeMille, *New Limit on the Electron Electric Dipole Moment*, Phys. Rev. Lett. **88** (2002) 071805.

[92] J. Donoghue, *T Violation in SU(2) X U(1) Gauge Theories of Leptons*, Phys. Rev. **D18** (1978) 1632.

[93] E. P. Shabalin, *Electric Dipole Moment of Quark in a Gauge Theory with Left-Handed Currents*, Sov. J. Nucl. Phys. **28** (1978) 75.

[94] D. Chang, *Mechanisms of CP Violation in Gauge Theory and the recent Developments*, FERMILAB-CONF-90-265-T (1990).

[95] S. M. Barr and A. Zee, *Electric Dipole Moment of the Electron and of the Neutron*, Phys. Rev. Lett. **65** (1990) 21.

[96] M. Pospelov and A. Ritz, *Electric Dipole Moments as Probes of New Physics*, Annals Phys. **318** (2005) 119 [arXiv:hep-ph/0504231].

[97] G. D. Moore, *Sphaleron Rate in the Symmetric Electroweak Phase*, Phys. Rev. **D62** (2000) 085011 [arXiv:hep-ph/0001216].

[98] G. D. Moore, *Computing the Strong Sphaleron Rate*, Phys. Lett. **B412** (1997) 359 [arXiv:hep-ph/9705248].

[99] P. Huet and A. E. Nelson, *Electroweak Baryogenesis in Supersymmetric Models*, Phys. Rev. **D53** (1996) 4578 [arXiv:hep-ph/9506477].

[100] J. F. Gunion, H. E. Haber, H. L. Kane and S. Dawson, *Higgs Hunter's Guide*, Addison-Wesley Publishing Company, 1990.

[101] S. J. Huber, *Electroweak Baryogenesis in the Supersymmetric Standard Model with a Gauge Singlet*, PhD thesis, University of Heidelberg, 1999.

[102] B. Kastening, R. D. Peccei and X. Zhang, *Sphalerons in the Two-Doublet Higgs Model*, Phys. Lett. **B266** (1991) 413.

[103] D. Land and E. D. Carlson, *Two Stage Phase Transition in Two Higgs Models*, Phys. Lett. **B292** (1992) 107 [arXiv:hep-ph/9208227].

[104] S. Weinberg, *Unitarity Constraints on CP Nonconservation in Higgs Exchange*, Phys. Rev. **D42** (1990) 860.

[105] W. Bernreuther and M. Suzuki, *The Electric Dipole Moment of the Electron*, Rev. Mod. Phys. **63** (1991) 313 [Erratum-ibid. **64** (1992) 633].

[106] J. F. Gunion and R. Vega, *The Electron Electric Dipole Moment for a CP Violating Neutral Higgs Sector*, Phys. Lett. **B251** (1990) 157.

[107] D. Chang, W. Y. Keung and T. C. Yuan, *Two Loop Bosonic Contribution to the Electron Electric Dipole Moment*, Phys. Rev. **D43** (1991) 14.

[108] R. G. Leigh, S. Paban and R. M. Xu, *Electric Dipole Moment of Electron*, Nucl. Phys. **B352** (1991) 45.

[109] S. Weinberg, *Larger Higgs-Boson-Exchange Terms in the Neutron Electric Dipole Moment*, Phys. Rev. Lett. **63** (1989) 2333.

[110] J. F. Gunion and D. Wyler, *Inducing a Large Neutron Electric Dipole Moment via a Quark Chromoelectric Dipole Moment*, Phys. Lett. **B248** (1990) 170.

[111] A. Denner, R. J. Guth and J. H. Kuhn, *Relaxation of Top Mass Limits in the Two Higgs Doublet Model*, Phys. Lett. **B240** (1990) 438.

[112] A. K. Grant, *The Heavy Top Quark in the Two Higgs Doublet Model*, Phys. Rev. **D51** (1995) 207 [arXiv:hep-ph/9410267].

[113] F. M. Borzumati and C. Greub, *Two Higgs Doublet Model Predictions for Anti-B → X/s Gamma in NLO QCD. (Addendum)*, Phys. Rev. **D59** (1999) 057501 [arXiv:hep-ph/9809438].

[114] P. H. Chankowski, M. Krawczyk and J. Zochowski, *Implications of the Precision Data for Very Light Higgs Boson Scenario in 2HDM(II)*, Eur. Phys. J. **C11** (1999) 661 [arXiv:hep-ph/9905436].

[115] A. Arhrib, *Unitarity Constraints on Scalar Parameters of the Standard and Two Higgs Doublets Model*, arXiv:hep-ph/0012353.

[116] M. Chemtob, *Nucleon Electric Dipole Moment and Gluonic Content of Light Hadrons*, Phys. Rev. **D45** (1992) 1649.

[117] T. Hayashi, Y. Koide, M. Matsuda and M. Tanimoto, *Neutron Electric Dipole Moment in Two Higgs Doublet Model*, Nucl. Phys. Proc. Suppl. **39BC** (1995) 276 [arXiv:hep-ph/9409366].

[118] D. A. Dicus, *Neutron Electric Dipole Moment from Charged-Higgs-Boson Exchange*, Phys. Rev. **D41** (1990) 999.

Acknowledgements